UNIVERSIDADE FEDERAL DO CEARÁ
CENTRO DE TECNOLOGIA
DEPARTAMENTO DE ENGENHARIA METALÚRGICA E DE MATERIAIS
PROGRAMA DE PÓS-GRADUAÇÃO EM ENGENHARIA E CIÊNCIA DE MATERIAIS

JOSÉ RENÊ DE SOUSA ROCHA

THERMOMECHANICAL ANALYSIS OF IN-SERVICE WELDING PIPELINES USING THE ELEMENT-BASED FINITE VOLUME METHOD

FORTALEZA
2022

JOSÉ RENÊ DE SOUSA ROCHA

THERMOMECHANICAL ANALYSIS OF IN-SERVICE WELDING PIPELINES USING THE ELEMENT-BASED FINITE VOLUME METHOD

Tese submetida ao Programa de Pós-Graduação em Engenharia e Ciência de Materiais da Universidade Federal do Ceará como requisito parcial à obtenção do título de Doutor em Engenharia e Ciência de Materiais. Área de Concentração: Processos de transformação e degradação dos materiais.

Orientador: Prof. Dr. Francisco Marcondes

Coorientador: Prof. Dr. Hélio Cordeiro de Miranda

Aprovada em: .

BANCA EXAMINADORA

Prof. Dr. Francisco Marcondes (supervisor)
Federal University of Ceará (UFC)

Prof. Dr. Hélio Cordeiro de Miranda (co-supervisor)
Federal University of Ceará (UFC)

Prof. Dr. Marcelo Ferreira Motta
Federal University of Ceará (UFC)

Prof. Dr. Clovis Raimundo Maliska
Federal University of Santa Catarina (UFC)

Prof. Dr. José Adilson de Castro
Fluminense Federal University (UFF)

Dados Internacionais de Catalogação na Publicação
Universidade Federal do Ceará
Sistema de Bibliotecas
Gerada automaticamente pelo módulo Catalog, mediante os dados fornecidos pelo(a) autor(a)

S697t Sousa Rocha, José Renê de.
Thermomechanical analysis of in-service welding pipelines using the Element-based Finite Volume Method / José Renê de Sousa Rocha. – 2022.
158 f. : il. color.

Tese (doutorado) – Universidade Federal do Ceará, Centro de Tecnologia, Programa de Pós-Graduação em Engenharia e Ciência de Materiais, Fortaleza, 2022.
Orientação: Prof. Dr. Francisco Marcondes.
Coorientação: Prof. Dr. Hélio Cordeiro de Miranda.

1. Element-based Finite Volume Method. 2. 3D simulation. 3. Unstructured mesh. 4. In-service welding. 5. Axial stress. I. Título.

CDD 620.11

To God.
To my parents, Pedro and Celina.

ACKNOWLEDGEMENTS

First of all, I would like to thank my family, specially my parents, Pedro and Celina, for all support during these years that I have been at Federal University of Ceará, for their good advices and guidance to succeed in all steps of my life.

I am thankful to all professors who I had the opportunity to study during these two years at the Graduate Program in Engineering and Material Science, besides, I would also like to express my gratitude for their help and effort to transmit some fundamental knowledge to us. Amongst the professors, I would like to thank my supervisor, Francisco Marcondes, with whom I had the opportunity to develop this study. In addition, I thank him for his fundamental experience during the supervision of this research, his helpful tips and review of this text, and all his collaboration during the development of this thesis.

I am also grateful to the committee members, composed by prof. Dr. Francisco Marcondes, prof. Dr. Hélio Cordeiro de Miranda, prof. Dr. Marcelo Ferreira Motta, prof. Dr. Clovis Raimundo Maliska, and prof. Dr. José Adilson de Castro, for their availability in being part of this work.

I would like to thank my classmates and friends for the great moments of joy and studies throughout this long journey of hard work. Furthermore, I would like to recognize the great advices, comments, and the significant sharing of information that I have received from my friends from the Computational Fluid Dynamics Laboratory (LDFC) and especially thank to Paulo and Ivens, whose guidance at earlier stages of this thesis brought some fundamental contribution to this work to be finished.

Last but not least, I would like to acknowledge the financial support provided by FUNCAP (Cearense Foundation of Support for Scientific and Technological Development) to this research.

“The error therefore lyeth neither in the abstract nor in geometry, nor in physicks, but in the calculator, that knoweth not how to adjust his accompts.”

“Galileo Galilei”

ABSTRACT

Currently, the welding process is the most used technique for joining workpieces. In-service welding of oil and gas pipelines is a technique, which shows important economic aspects as well as low environmental impact. The aforementioned benefits are possible since there is no need for interrupting the flow operation during pipe repairs, branch on pipes or substitution of some defective pipe section. However, during this process, some detrimental phenomena such as hydrogen-induced cracking and burn-through may appear. The thermomechanical model for analyzing heat transfer from the arc welding as well as the fluid flow into the pipeline is very complex, therefore analytical solutions are not available. Physical studies might present many difficulties for analyzing the process. Therefore, numerical methods emerge as an attractive alternative to solve several classes of engineering problems. The main goal of the present study is to develop a numerical simulator using the EbFVM (Element-based Finite Volume Method) to analyze in-service welding processes of pipelines. The flexibility of treating complex geometries through EbFVM make possible the analysis of various actual engineering problems. Based on the performed simulations, some preliminary modifications in the process variables can be proposed in order to improve the weld quality. For solving the governing equations arising from the thermomechanical model, the EbFVM was used in conjunction with unstructured grids. The numerical simulations were performed for applications in real welding process. Simulations were performed using methane as working fluid for a turbulent flow; Turbulence modeling was performed by making use of empirical correlation. The results are presented in terms of thermal cycles, temperature fields, axial and hoop stresses, and radial shrinkage, which evaluated them qualitatively and quantitatively. Furthermore, the developed simulator was confronted against experimental works, analytical solutions from literature, and others numerical studies. Finally, in most scenarios, excellent agreements were achieved.

Keywords: EbFVM, 3D simulation, Unstructured mesh, In-service welding, Thermal cycle. Axial and hoop stresses, Radial shrinkage.

LIST OF FIGURES

LIST OF TABLES

CONTENTS

CHAPTER
1

INTRODUCTION

One of the manufacturing methods of joining materials, the welding process, is applied in a myriad of materials which are employed in engineering. Therefore, it has vital influence in the thermomechanical behavior during structural element lifetime. According to American Welding Society (AWS) (1976), the welding process can be thought of as materials joining process that makes coalescence amongst materials by heating them to a given temperature. It worth to mention that the metal heating is most provided by an electric arc. In addition, a given pressure may or may not be applied in such processes as well as it may be applied by itself (Friction Stir Welding (FSW), for example). Also, the process can be made with or without the use of filler metal, in case of electric arc welding process (AWS, 1976).

Amongst the welding applications one can cite the constructions of bridges, oil platform, pressure vessels, aircrafts, automobile and nuclear reactors; in all these areas, different types of materials such as stainless steel, aluminum, magnesium, and copper can be welded. In contrast to conventional form of welding, in-service welding pipeline has gained academic and industrial attention mainly by its continuous basis modus operandi during welding repairs, branch on pipes or substitution of some defective pipe section. It is important to note that all these uses of in-service welding are a subset of the hot-tapping technique (Jaske et al., 2006; Pereira, 2012).

Welding Processes involving fluid flow in pipelines present by itself some dangerous issues. This is mainly due to the high pressure of the fluid flow and the high heat input provided by the arc welding. Therefore, this process needs to be made by high-quality welders and also welding simulations can be used to make preliminary analysis in order to avoid excessive costs of experiments. The interruption of such operations every time some welding is needed is not economic viable, so that in such situations in-service welding is mandatory.

Nowadays oil, gas and similar companies make use of pipelines for conveying large amounts of fluid through long distances. These pipelines need constantly preventive or corrective maintenance, so that the process can be operated uninterruptedly and avoid the additional costs provided from the operational stops. Moreover, in many situations, it is required addition pipe ramifications in order to supply the increasingly industrial demands.

The knowledge of the main factors which control the fluid flow by forced convection inside a given pipeline as well as its mechanical state at walls is it of vital importance for analyzing the physical process which governs such phenomena. Therefore, the full understanding of the in-service welding technique is fundamental for safety welding procedures since these operations modify the structural components of oil and gas pipelines.

The heat generated during welding process is dissipated through thermal radiation, free and forced convection and conduction. Conduction is possible when there is a temperature difference in a given medium, where this medium may be either a solid or fluid (liquid or gas). Also, it is important to mention that the heat conduction is the main mechanism of heat transfer during a welding procedure. Convection occurs between a solid and a moving fluid, in the presence of some temperature gradient. Thermal radiation is provided by the emission of electromagnetic waves in all bodies with non-zero temperatures (Incropera and DeWitt, 1990).

In-service welding can guarantee the continuity of the process without interrupt it, and therefore resulting in economic benefits and also keeping environmental impacts lower by avoiding leaking of harmful gases to the environment. The main disadvantages of in-service welding process, which sometimes may be crucial, is the higher tendency of forming hydrogen-induced cold cracking at pipeline walls of carbon and low-alloy steels (especially at the heat affected zone, HAZ) due to the fast cooling rate provided by the flowing oil/gas and the burn-through effect, which is caused by the excessive heat provided by the arc welding (Sabapathy et al., 2001). Last but not least, the fluid pressure is also needed to be considered when in-service welding is employed.

Considering the industrial relevance of the foregoing process and with the aim to increase the quality of the weld, researchers have carried out investigations in analytical, experimental, and numerical areas concerning the main relevant aspects that govern the fluid flow into the molten pool, the heat transfer as well as the stress/strain field throughout the workpiece being welded (Pereira, 2012; Sabapathy et al., 2001; Wang et al., 2013). As we know, experimental analysis has many drawbacks, such as high cost of equipment and less possibility to both change and analyze different scenarios. On the other hand, performing numerical analysis of in-service welding processes can overcome these drawbacks. Fig. 1.1 shows the in-service welding technique being executed.

Figure 1.1 – In-service welding technique.

Source: Wang et al. (2013).

The long-stablished methods to solve the set of partial differential equations numerically can be divided into three main categories: Finite Volume Method (FVM), Finite Element Method (FEM), and Finite Difference Method (FDM). Moreover, Finite Volume Method is the most used method in the thermo-fluid commercial packages and has gained great attention in solid mechanic simulations, since it is the only numerical approach that can warranty local conservation of the physical quantities (mass, momentum, and energy) (Maliska, 2004).

Numerical approaches can be used to perform analysis of systems that involve fluid flow, heat transfer, induced stress/strain and related phenomena such as combustion processes. In addition, solution is obtained in a computer-based simulation, since this approach involves cumbersome calculations. Numerical methods are based on the approximate solution of governing equations, viz., mass, momentum, and energy equations along with proper initial and boundary conditions. Also, Numerical methods have gained great attention in the research community as a result of their flexibility and low effective costs.

To perform a numerical simulation, four main steps must be followed:

- Defining the physical model;
- Defining the geometry and creating the mesh;
- Solving the given problem numerically;
- Postprocessing and visualizing the obtained results.

Analyzing the various physical and geometric parameters involved in welding modeling might be a complex task, especially when experimental techniques are applied. There are many advantages when comparing numerical techniques over experimental approaches, for instance, reduction of time to analyze systems with no added expenses, possibility to perform studies under hazardous conditions, infinite level of parametric studies leading to unlimited possibilities, reliable results, and ability to simulate ideal and realistic relevant problems. Nevertheless, to take full advantage of numerical capabilities, experience and exhaustive trial-and-error analysis is required by the design engineer.

However, numerical simulation in the welding analysis should not replace experimental analysis, instead, numerical analysis must be complemented by experimental ones in order to make integrated studies in complex systems (the thermomechanical coupling as one example) of vital importance to engineering.

As long as the influence of fluid flow as well as the heat provided by the electric arc welding is known, the design engineer has the chance to select high-resistance pipes, with larger diameters and thinner walls with the aim to increase the quality and reduce the material required for the construction of pipelines.

1.1 Objectives

1.1.1 General objective

The main objective of this study is to develop a numerical-computer-based simulator by making use of the Element-based Finite Volume Method in conjunction with unstructured grids in order to evaluate qualitatively and quantitatively the thermomechanical effects provided by general in-service welding processes.

1.1.2 Specific objectives

The main objective may be split into the following specific objectives:

- Verify and validate the thermo-elastoplastic numerical approach using experimental, numerical, and analytical works from the literature;
- Evaluate the influence of the 3D thermal field provided by the electric arc welding on the structural behavior of the pipeline;
- Assess the thermal cycles along the pipe walls during the in-service welding of pipelines;
- Evaluate the thermal distribution along the longitudinal pipe walls during the in-service welding process;
- Analyze the influence of fluid flow over the pipeline through empirical correlations from literature;
- Perform a parametric approach to evaluate various contributing factors to the weld induced residual stresses and weld distortions;

1.2 Research motivation

The in-service welding technique has gained special attention from the researchers and the industrial community since the necessity of weld quality improvement when concerning high-risk welding processes. Such technique allows the continuity of the normal pipeline operations during inevitable interventions leading to benefits for both the customers and the suppliers. Clearly, the achievement of success and safety operations depend upon the knowledge of the variables and procedures concerning this technique.

The turbulent fluid flow inside the pipelines enhances the cooling process during the welding operation. The main mechanism of heat transfer during in-service welding is the forced convection (Sabapathy et al., 2001), therefore an important step in the numerical simulation is to determine the heat transfer coefficient between the flow and the pipe wall. Many numerical studies in the area of in-service welding (Wang et al., 2013; Asl and Vatani, 2013) have made use of empirical correlations to calculate the heat transfer coefficient such as the Dittus-Boelter correlation (Incropera and DeWitt, 1990), which is based on the assumption of fully developed turbulent flow in smooth circular pipes. Sabapathy et al. (2001) and Wahab et al. (2005) calculated the heat transfer coefficient through a dimensionless approximation based on the empirical correlation of Seider and Tate's (Incropera and DeWitt, 1990).

During the in-service welding process a combination of a highly localized heat source acting upon the workpiece, the high cooling rates caused by the internal fluid flow, and the mechanical loads which is imposed by restrictions and internal pressure of the fluid may induce thermal residual stresses and distortions at the welded pipeline. The induced welding residual stresses and distortions have been considered a great challenge for engineers due to their complex nature. The main problems that can be caused by such imperfections are: hydrogen-induced cracking, fatigue damage, stress corrosion cracking, brittle fracture, and expansions/contractions. Therefore, the proper prediction and correction of welding residual stress and distortions are mandatory in any manufactory welding process in order to eliminate or at least minimize the aforementioned problems.

FEM has been used in most of published works concerning the thermo-mechanical welding processes. In addition, FEM is the most used method in the commercial packages, since it is traditionally used in solid mechanics analysis, and in particular, in Computational Welding Mechanics (CWM) (Lindgren, 2007). Despite being well-stablished numerical approaches, a few works in the welding area have devoted to the use of both FDM and FVM. Therefore, additional methodology will always be welcome to enhance the body of knowledge in any area of the physics and engineering. Finally, to the best of o knowledge there is no study applying the Element-based finite Volume Method to analyze the thermomechanical behavior of in-service welding pipelines. In this work, the EbFVM (Maliska, 2014; Marcondes et al., 2013) has been used to discretize the energy and the momentum equations for analyzing a thermo-elastoplastic problem, and therefore, we can contribute to the Computational Welding Mechanics area with a robust and reliable method for solving such problems.

CHAPTER

2

LITERATURE REVIEW

2.1 In-service welding process

In-service welding pipelines have been largely used in oil and gas industry, petrochemical, power generation, and related areas in order to make possible the continuity of operation during maintenance process, for instance. During the projection of in-service welding procedures, it is mandatory to observe some criteria in order to avoid burn-through (wall penetration) and cold cracking (hydrogen-induced cracking) along the pipe walls of carbon and low-alloy steels. These procedures involve the heat provided from the electric arc welding, pipe chemical composition, and the internal pressure of the fluid flow through the pipe (Pereira, 2012).

There exists a myriad of welding process which can be used in in-service welding operations such as MIG/MAG (Metal Inert Gas/Metal Active Gas), TIG (Tungsten Inert Gas), PAW (Plasma Arc Welding), SAW (submerged Arc Welding), among others. The correct choice amongst the aforementioned processes depends on the final application and location of the structure to be welded (Cary and Helzer, 2004).

Since in-service welding is often performed in remote areas, one can cite the SMAW (Shielded Metal Arc Welding) as one viable process for using due to its versatility, low cost, flexibility, portability and adaptation to the high cooling rates without introduce defects such as the lack of fusion on the weld joints (Jeffus, 2012; Küchler, 2009). This process is illustrated in Fig. 2.1.

Figure 2.1 – Shielded Metal Arc Welding.

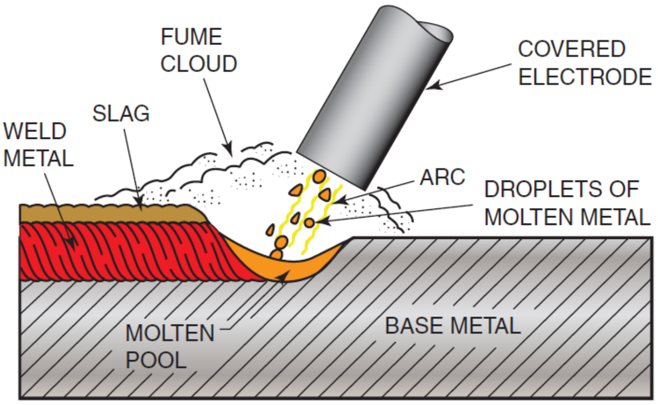

Source: Jeffus (2012).

In-service welding is part of a general operation for constructing pipelines, the so-called hot-tapping technique. Hot-tapping allows the addition of branch connections to a main pipeline and it is able to keep the process in a continuous basis. It is important to mention that the success of hot-tap operation is directly affected by the welding on both the valve assembly (a mid-way part of the operation) and the sleeve fitting onto the live pipeline (Sabapathy, 2002).

In-service welding technique can be divided into two main categories: the first one is mainly concerned to repair onto pipeline discontinuities and the second one concerned to the addition of new branch pipe connections (Pereira, 2012). The branch on pipes, where auxiliary pipes are used for deviating the working fluid to the principal pipes, while repairs are made, are of vital importance when there is necessity of increase or apply ramification of pipeline networks.

The main types of welding repairs applied to in-service operations are illustrated in Figs. 2.2 and 2.3. Fig. 2.2 illustrates the split repair sleeve method. It consists basically in the assembling two half-sleeves involving the pipe with one longitudinal and two circumferential fillet welds. In this method, while longitudinal weld does not offer any deleterious effect on the pipe, the circumferential fillet weld may induce thermal stress and high temperatures along pipe walls as result of the welding process (Alian et al, 2016).

Figure 2.2 – Sleeve repair of a defective pipe.

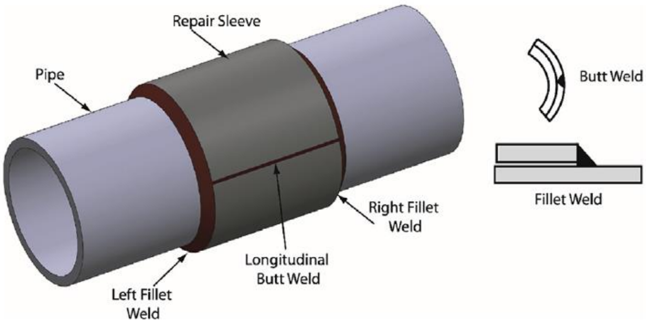

Source: Alian *et al*. (2016).

The repair by direct deposition of weld metal is illustrated in Fig. 2.3. In this method, welding is applied onto the pipe surface which suffered from internal wall losses due to material corrosion, reducing the pipe strength, and possibly causing the burn-through of the pipe wall. According to Jaske et al. (2006), this is specially applied in bend pipe sections and fittings, where the use of full-encirclement sleeves is prohibitive.

Figure 2.3 – Weld direct deposition.

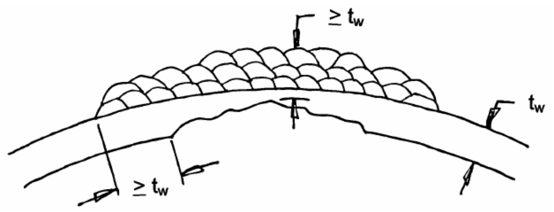

Source: Jaske et al. (2006).

In-service welding shows typical aspects such as the necessity of low energy process and the influence on the welding cooling rates by the forced convection provided by the fluid flow into the pipe. According to Pereira (2012), the main aspects required during in-service welding procedure in order to obtain crew safety as well as the integrity of the system are:

- Avoid excessive arc welding penetration at the pipe wall.
- Produce non-defective welds, with reasonable strength.

- Avoid cold cracking at HAZ by limiting its hardness.
- Avoid the reduction of internal pipe strength.

During in-service welding processes, the main concerns that need to be avoided are the burn-through and cold cracking formation at HAZ. Burn-through may occur due to localized heat provided by the electric arc welding, which can result the internal surface of the pipe with low strength. In addition, concerning the flow welding parameters, the pipe wall may also fail due to internal pressure of the working fluid, since the wall strength reaches sufficient low values (Asl and Vatani, 2013). Wade (1982) performed an experimental study on pipes subjected to pressurized gas by varying the wall thickness, the arc energy, and the internal gas pressure. In that study, he defined a burn-through failure as soon as a bulge of 1.0mm in height or higher is formed in the weld zone. Fig. 2.4 illustrates both bulging and burn-through effects.

Figure 2.4 – (a) Bulging and (b) Burn-through failures due to in-service welding.

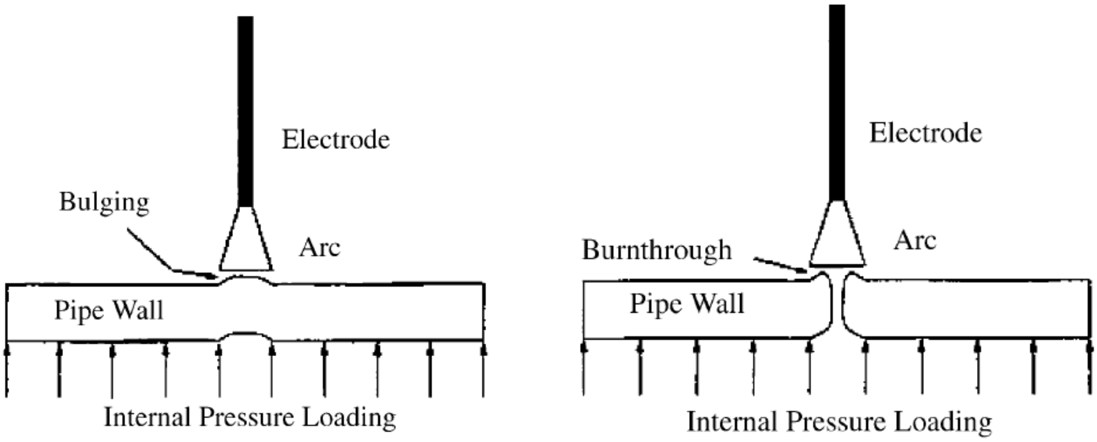

Source: Wahab et al. (2005).

The cold cracking formation may occur due to the high cooling rate during the welding; this is due to high heat rate transfer extracted from the pipe wall by the convection of the working fluid flow through the pipe. These combined factors impose the HAZ microstructure to high hardness, leaving the structure susceptible to formation of cracks (Küchler, 2009). It is important to mention that the most prone sites for cold cracking appear is the HAZ as well as the interface between HAZ and FZ (fusion zone) (Kou, 2003; Sharma and Maheshwari, 2017).

Fig. 2.5 shows the main regions originated during a welding process as well as the correspondent microstructures presented in a Fe-C phase diagram for a low-carbon 1018 steel.

Figure 2.5 – Specimen regions and correspondent Fe-C phase diagram.

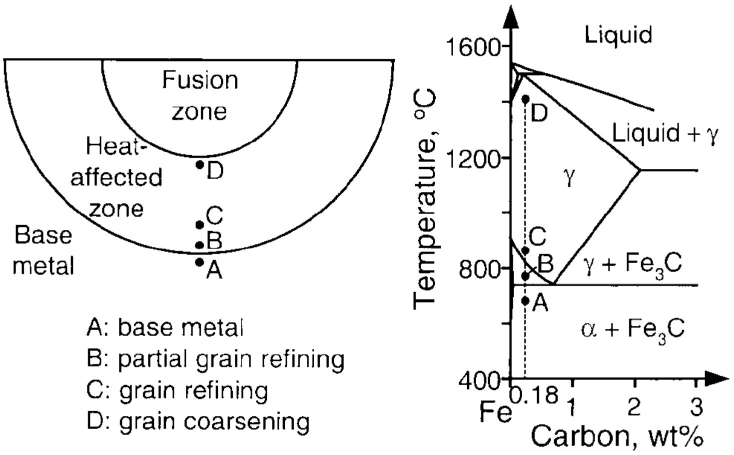

Source: Kou (2003).

The various HAZ regions which occur during a multi-pass in-service pipeline steel welding is depicted in Fig. 2.6.

Figure 2.6 – Schematic illustration of the different HAZ regions in a multi-pass welding.

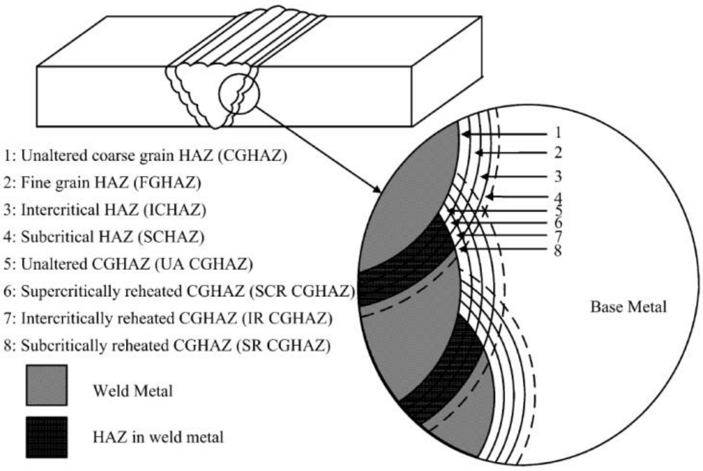

Source: Li et al. (2011a).

As Kou (2003) stressed out, cold cracking is formed when the following four factors are present simultaneously: presence of hydrogen in the weld metal, high stresses, susceptible microstructure (martensite), and relatively low temperatures (ranging from 100 to 200°C). As one could notice, the second and the third aforementioned factors are greatly augmented onto in-service welding operations.

High Strength Low Alloy (HSLA) steel grades have been commonly used in in-service pipelines since they present higher strength yield and thinner wall thickness giving the possibility of carrying a larger quantity of fluid material with a higher internal pressure. Therefore, HSLA steel grades are the best suited materials for the requirements of the pipelines of the oil and gas industries (Sharma and Maheshwari, 2017). As Sabapathy (2002) pointed out, the enhanced fluid transmission in conjunction with the reduction of pipe wall thickness will produce higher cooling rates as a consequence the harder microstructure may be formed at the HAZ leaving the material susceptible to cold cracking. Moreover, the pipe becomes prone to bulging or even explode by the influence of the arc welding (burn-through).

Therefore, as previously pointed out with the aim to adjust economic benefits, crew safety and system integrity some conservative actions must be implemented such as the use of proper heat input, reduction of pipeline internal pressure and/or fluid flow rate and make use of high strength pipes (Sabapathy, 2002; Asl and Vatani, 2013).

2.2 Analytical solutions

By solving the heat conduction equation analytically, the time-consuming process, usually encountered in numerical analysis, can be surpassed and also the solution can be considered free of spatial and temporal discretization errors provided from numerical studies.

Analytical solutions are obtained for welding analysis by starting from the linear heat conduction equation

$$\rho c \frac{\partial T}{\partial t} = k \nabla^2 T + q \tag{2.1}$$

where T is the temperature, k is the thermal conductivity, ρ denotes the material density, c is the specific heat coefficient, and q denotes the heat input which is originated from the arc welding.

Analytical solutions of the heat conduction equation with both a point and a line heat source were first derived by Rosenthal (1941) in the mid-1940s. His analytical solution was based on a number of simplifying assumptions, viz., constant material properties, semi-infinite orthogonal domain, quasi-steady-state regime (which leads to neglect the beginning and ending arc transient effects) and absence of weld grooves. Furthermore, phase change, convection and radiation thermal losses were neglected. In the case of three-dimensional heat transfer in a given domain, Rosenthal’s equation in a moving coordinate system can be given as

$$T = T_0 + \frac{P}{2\pi kR} exp\left[-\frac{v}{2\alpha}\left(x+R\right)\right] \tag{2.2}$$

where T_0 is the initial temperature, $P = \eta \times U \times I$ is the net power provided by the arc welding, U is voltage, I is the current, η denotes the process efficiency, k is the thermal conductivity, $R = \sqrt{x^2 + y^2 + z^2}$ is the distance between the heat source to a given point, v denotes the welding speed, and α denotes the thermal diffusivity. Fig. 2.7 shows temperature profiles using Eq. 2.2.

Figure 2.7 – Rosenthal’s solution in a given plate.

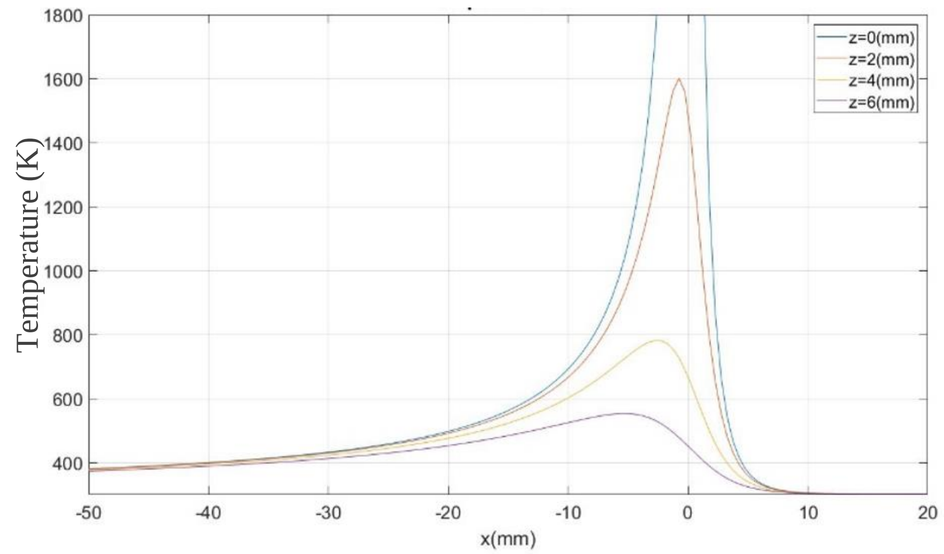

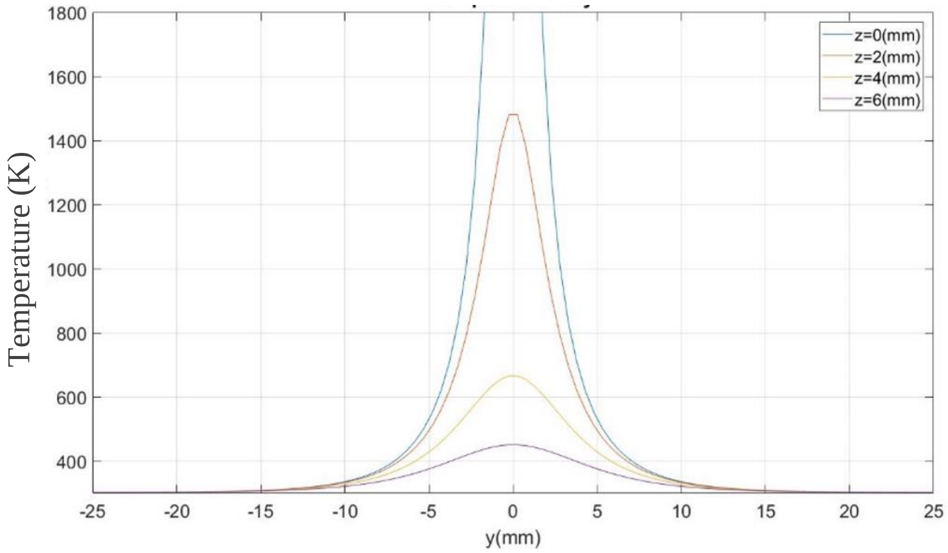

Despite the relevant contribution provided by the Rosenthal's analytical solution to the welding analysis, it is important to mention that the simplified assumptions cause serious divergences in the temperature profile near the arc welding including regions such as the Fusion Zone (FZ) and the Heat Affected Zone (HAZ), and therefore, the accuracy of the solution is drastically reduced, as we can see in Fig. 2.7. In fact, at heat source origin, the Rosenthal analytical solution provides infinite temperature, which is physically unrealistic. This is due to the assumption of point heat source model.

Despite those aforementioned drawbacks, Rosenthal (1941) lighted out relevant observations in welding analysis such as: the rise of temperature in front of the arc welding is steeper than the fall behind it, the welding speed affects the isotherm shape, the metal being welded is heated faster than cooled in a given temperature (KOMANDURI and HOU, 2000; Rosenthal, 1941). Based on the Rosenthal's results, Christensen et al. (1965) formulated a dimensionless analytical form in order to demonstrate the applicability in a variety of materials and welding process parameters. They found fair agreement in the weld pool shape, length and width of the pool. However, the weld depth is not accurated.

In order to enhance the pioneering analytical works, some authors have made some important contributions by adding more realistic assumptions to the previous studies. Eagar and Tsai (1983) performed an analytical analysis through the use of a 2D Gaussian distributed heat source on a semi-infinite plate. They compared their theoretical study with experimental results for different types of materials such as carbon steels, stainless steels, titanium, and aluminum with good agreement between the experimental and analytical solutions. In additions, they concluded that both welding process variables, viz., current, arc length and welding speed, and material parameters such as thermal diffusivity, have substantial effects on weld pool shape.

Boo and Cho (1990), proposed an analytical solution to predict transient temperature distribution over a three-dimensional finite thickness plate during an arc welding operation. Convection boundary conditions were applied to this model as well as a 2D Gaussian distributed heat source. To take into account the flow provided by the shielding gas, forced convection was applied at the top surface right beneath the welding torch and free convection was assumed at the bottom surface. Satisfactory accuracy was obtained when comparing this particular solution with experimental GTAW bead-on-plate series of experiments performed on a carbon steel medium.

Nguyen et al. (1999) developed transient analytical solutions for solving the heat conduction equation with the addition of 3D semi-ellipsoidal and double-ellipsoidal heat sources in a semi-infinite domain. Good agreement was obtained when compared transient experimental temperature distributions in specific points in a given specimen. Also, the predicted weld pool geometry was in accordance with the experimental measures.

Although numerical methods have been predominant in welding area, important analytical solutions have been also contributed to shade some light in complex phenomena of the welding process. Fachinotti et al. (2011) improved the Nguyen et al. (1999) model by making use of the double-ellipsoidal and double-ellipse heat source with different values for the size and heat input in the front and rear parts of the heat source subregions. In addition, the authors compared the analytical solution with both a fully 3D and a cross-sectional 2D numerical Finite Element Analysis (FEA) and they reached an excellent agreement among the three developed approaches.

Flint et al. (2018) derived a semi-analytical solution for the transient temperature field in a 3D orthogonal domain subjected to any linear combination of double-ellipsoidal or double-ellipsoidal-conical (DEC) heat sources. The solution was confronted with both numerical FEA and experimental studies and fair agreement was obtained. In addition, dramatic reduction of computing time, as commonly observed in analytical solution, was also noticed.

It is worth mentioning that the most recent developments concerning analytical solutions take advantage of numerical methods; this is due to the appearing of time integrals that do not have a closed analytical expression in the final form of the temperature field solution, therefore numerical integration is required to fully obtain the final analytical expression and the solution is in fact a semi-analytical one. Finally, in spite of gaining great insights with analytical solutions, as we could see in the foregoing studies, all of them were performed in an orthogonal domain, which leaves pipes welding analysis out of this approach and consequently in-service welding analysis as well. Therefore, in order to study the transient temperature distribution all over pipelines, one needs to rely on both experimental and numerical analysis.

2.3 Numerical methods applied to welding

With the aim to increase the quality of the weldment, researchers have carried out investigations in analytical (Rosenthal, 1941; Nguyen et al., 1999; Fachinotti et al., 2011; Flint et al., 2018), experimental (Li et al., 2011a; Li et al., 2011b;), and numerical (Anca et al., 2011; Gery et al., 2005) areas concerning the main relevant aspects that govern the fluid flow into the molten pool as well as the heat transfer throughout the workpiece being welded.

Analytical studies on thermal welding are based on a number of simplifying assumptions, which imposes to this type of analysis a certain degree of limitation. Experimental analysis, as one knows, has many drawbacks such as high cost of equipment and less possibility to both change and analyze different scenarios. On the other hand, since actual welding process requires all the aforementioned aspects to be correctly accounted for, numerical analysis may overcome these drawbacks concerning the welding area.

For solving numerically, the partial differential equations which arise from the physical welding model, several authors have been used the Finite Element Method (FEM) (Anca et al., 2011; Lindgren et al., 1999), the Finite Difference Method (FDM) (Pavelic et al., 1969; Magalhães et al., 2018) and the Finite-Volume Method (FVM) (Taylor et al., 2002; García-García et al., 2016). In addition, regarding time-saving considerations, alternative numerical proposals for treating welding process have been used (Barroso et al., 2010).

FEM has been used in most of published works concerning the thermo-mechanical welding fields. In addition, FEM is the most used method in the commercial packages, since it is traditionally used in solid mechanics analysis, and in particular, in Computational Welding Mechanics (CWM) (Lindgren, 2007). A few works have devoted to the use of both FDM and FVM. In this work, the Element-based Finite Volume Method (EbFVM) (Maliska, 2014; Marcondes et al., 2013) is used to discretize the energy and the momentum equations.

A massive number of researchers have been focused on predicting in their numerical analysis on either macroscopic aspects of welding in a miscellaneous of welded structures such as distortion (Hashemzadeh, 2013; Okano and Mochizuki, 2017), residual stresses (Anca et al., 2011; Xu et al., 2012), and microscopic ones such as microstructural changes (Aissani et al., 2015; Chen et al., 2019). In order to further predict these aforementioned aspects numerically, which are strongly related to the final weldment quality, thermal welding analysis is mandatory, since these aspects are a consequence of the heat discharged at the weld Fusion Zone (FZ) and the subsequent heat transferred to the Heat-Affected Zone (HAZ) and to the unaffected Base Metal (BM).

It is well-known the intrinsic three-dimensional character of the temperature field along a given welded structure. Therefore, in order to perform realistic welding analyses, 3D models are always necessary since the distribution of temperature along the whole medium needs to be taken into account. The downside of 3D models for welding process is the higher time-consuming and the requirement of powerful computers to perform full analyses. However, as pointed out by Traidia et al. (2012), when phenomena such as the filler metal addition and non-flat weld positions needed to be included in a given simulation, 2D models cannot be used and therefore 3D modeling needs to be performed. Fig. 2.8 shows a three-dimensional welding simulation in a given plate, where the welding heat source is localized in two different positions.

Figure 2.8 – 3D numerical analysis in a given plate.

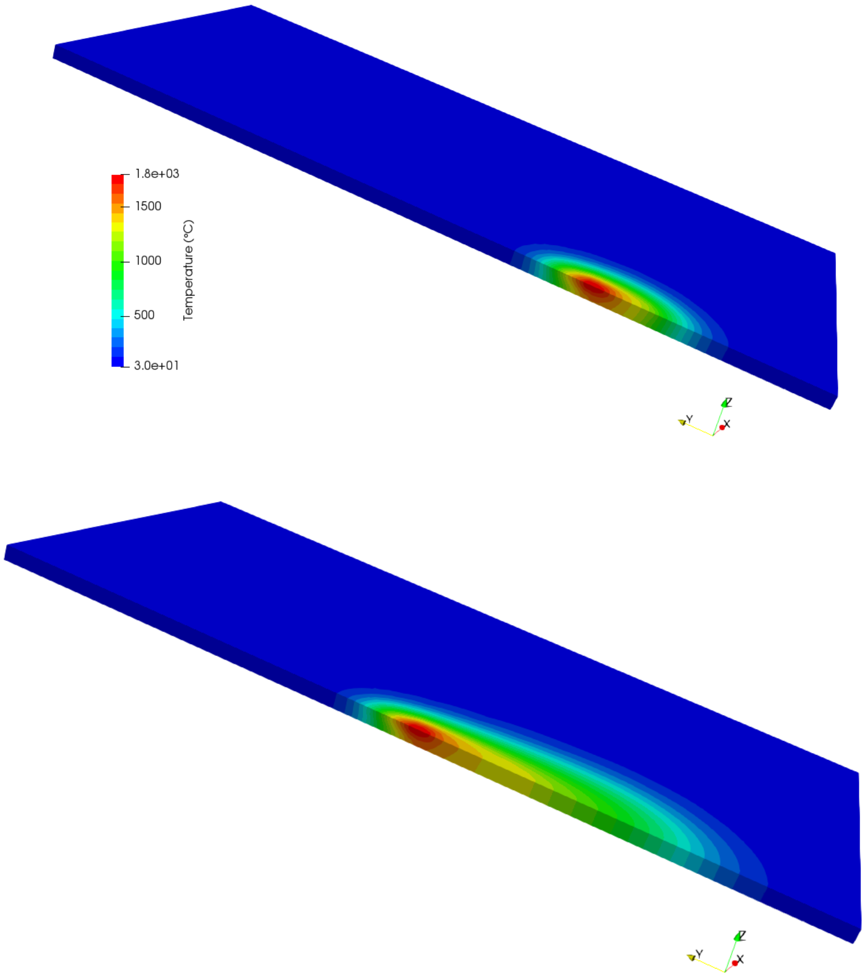

Earlier numerical studies in the welding area were developed using the two-dimensional assumption. Besides the easier numerical implementation of 2D models, the main advantage of performing a 2D numerical analysis is the reduction of CPU time requirements. Therefore, many authors have been reduced a full 3D model to different forms of 2D ones. In spite of some simplifying assumptions, two-dimensional models still can give accurate results. As one could see in Fig. 2.8, especially far away from the weld pool, the temperature can be assumed constant over the thickness, and the simulation can be performed in a 2D in-plane analysis. Fig. 2.9 presents a welding simulation in an *x*-*y* plane.

Figure 2.9 – 2D in-plane numerical analysis in a given plate.

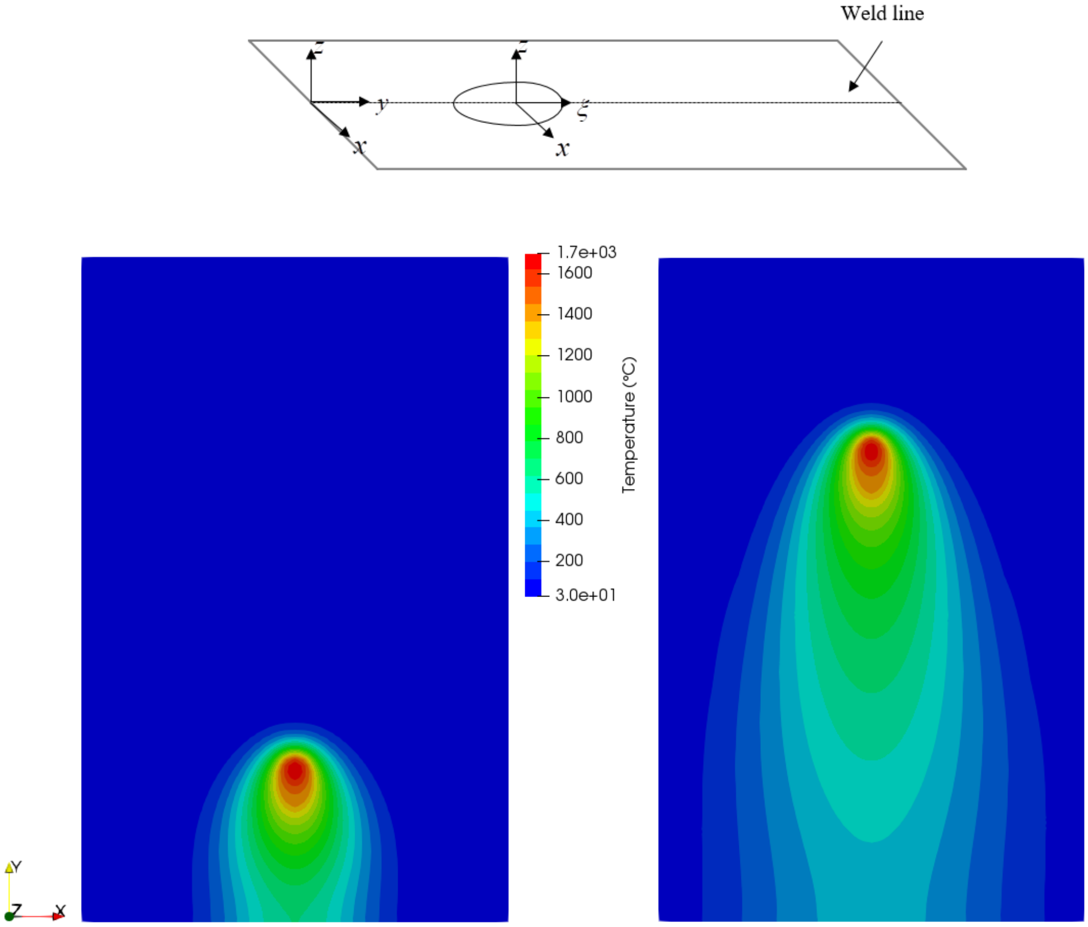

It is important to mention that in the 2D in-plane model, contrary to the 2D cross-sectional model, the whole plane (*y*-*x*) needs to be discretized in order to follow the surface heat source which passes along the given plane.

The 2D cross-sectional model, showed in Fig. 2.10, neglects the heat flow in the welding direction, i.e., $\left(\partial T/\partial y\right)=0$. By doing this, all the heat provided from the arc welding is deposited in a reference *x*-*z* plane.

Figure 2.10 – 2D cross-sectional numerical analysis in a given plate
with a surface heat source.

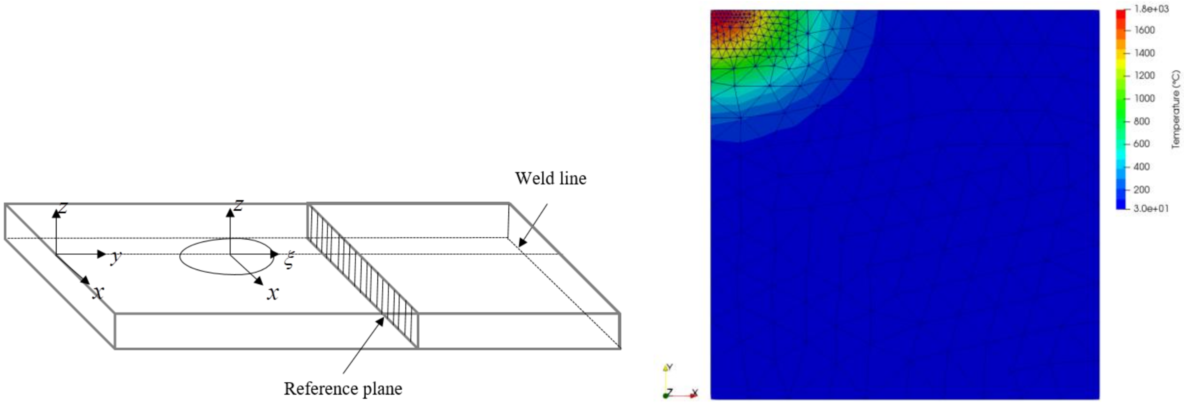

Fachinotti *et al*. (2011) pointed out that as long as the Peclet number (Pe) increases, the accuracy of the 2D cross-sectional model also increases. The Peclet number is directly proportional to the welding velocity v and to the characteristic dimension of the longitudinal direction L, and inversely proportional to the material thermal diffusivity α (Versteeg and Malalasekera, 2007; Mendez, 1995). Pe can be defined as

$$Pe = \frac{vL}{\alpha}, \tag{2.3}$$

It is important to mention that contrary to in-plane models, which may catch all transient temperature effects, cross-sectional models work well only for regions in the steady-state regime, i.e., the run-on and run-off welding effects are not well modeled.

To perform a welding process simulation, it is mandatory to know the material thermophysical properties as well as the process parameters under analysis. Therefore, the appropriate selection of these quantities is of great importance in order to guarantee the quality of a given numerical simulation. Through the use of FEM thermal simulations, Gery et al. (2005) investigated the effects of the heat source distribution, energy input and welding speed on temperature changes on a butt-joint welded plate. They found out that the above aforementioned factors greatly affect the shape and boundaries of both FZ and HAZ. Also, they concluded that these welding parameters influence the peak temperature in the FZ, so that they affect the transient distribution temperature onto the welded plate.

In order to reproduce real welding process by numerical models, the dependence of material thermophysical properties with temperature must be accounted for. Zhu and Chao

(2002) investigated three different scenarios for evaluating the specific heat, thermal conductivity, and density of 5052-H32 aluminum alloy in a FEM welding simulation, namely properties as a function of temperature, properties evaluated at room temperature, and properties as a mean value over the entire temperature history. From their study, it was concluded that the three approaches give rises to different results. However, as the authors pointed out, in the absence of data for the thermal properties (mainly at high temperature), constant room temperature values can be used in the welding simulations.

According to Goldak et al. (1984), a reasonable choice of the heat source is a mandatory factor for properly represent the thermal field in a welding numerical analysis. Therefore, since the earlier works by Rosenthal, where a point and line welding heat sources were proposed, many researchers have contributed to better approximate the shape and size of the molten pool as well as the way which the heat flux from the arc welding distributes onto a given medium. Contrary to the localized aspects of point and line heat application, Pavelic et al. (1969) first put forward the idea of a distributed flux onto an area by applying a Gaussian distribution of heat into a workpiece surface with the goal to model the welding heat source.

With this new way of modeling heat sources, a significant improvement in both analytical and numerical analysis could be achieved, since the effects in and near the molten pool could finally be correctly analyzed. It is important to stress out that this was not possible in Rosenthal’s heat source models due to the assumption that both the flux and temperature were assumed to be infinite at heat source. In the Pavelic’s circular disc model, the heat flux into a given workpiece has a Gaussian or normal distribution expressed by

$$q(r) = q(0)e^{-Cr^2} \tag{2.4}$$

where $q(0)$ denotes the maximum flux at the heat source center, C is a distribution width coefficient and r is the radial distance from the heat source center. Fig. 2.11 shows the parameters of model described above.

Figure 2.11 – Pavelic’s disc heat source model.

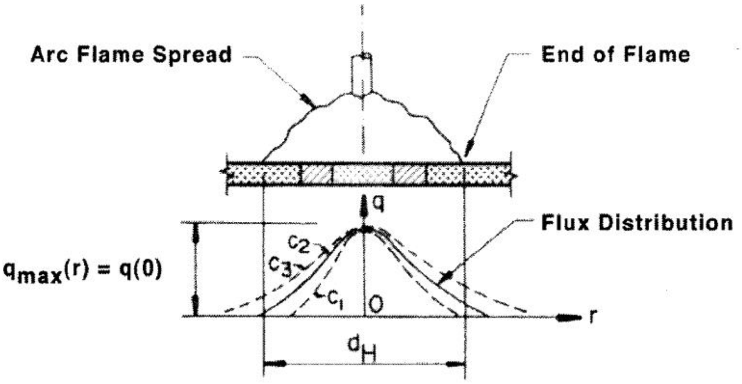

Source: Pavelic et al. (1969).

Alternative forms of the Pavelic’s disc heat source model were proposed subsequently by some authors, for example, the work by Friedman (1975). Aissani et al. (2015) determined the thermal properties for GTAW process using an experimental and a numerical approach. They implemented a 3D FEM model in which a bi-elliptical surface Gaussian heat source was used. In addition, metallographic analysis was performed to observe the microstructural evolutions. The approaches were confronted with one another and a good agreement between them was achieved.

Pavelic et al. (1969) and Friedman (1975) models work well in situations involving shallow weld penetration. Goldak et al. (1984) proposed a non-axisymmetric 3D heat source model for reaching a large range of welding penetrations, which would change according to the process, welding parameters, and material properties. Different from the traditional Pavelic’s and Friedman’s disc models, which distribute heat flux only at the workpiece surface, in Goldak’s double-ellipsoidal heat source (DEHS) model the heatsource acts throughout the molten zone, as a consequence the actual weld pool shape and size, the digging action, and stirring of the arc are taken into account.

Goldak’s DEHS is illustrated in Fig. 2.12, where a moving coordinate system (x, ξ, z) is following the heat source path.

Figure 2.12 – Goldak's DEHS model.

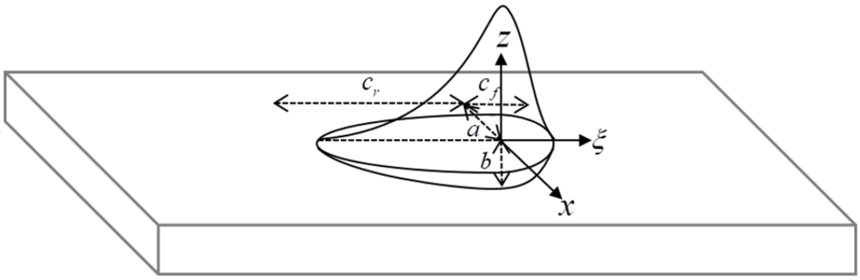

The parameters a, b, c_f, and c_r shown in Fig. 2.12 for the double-ellipsoid model are the semi-axes parameters to each heat distribution. It is important to mention that parameters a, b, c_f, and c_r, which denotes the width, depth and front and rear lengths of the molten pool, respectively are usually determined by metallographic analysis of the FZ (Xu et al., 2012) or even by neural-network programs (Moslemi et al., 2022). However, in the absence of experimental data, one can estimate the weld bead parameters from welding inputs by making use of some traditional mathematical methods such as the ones proposed by Christensen et al. (1965) and Eagar and Tsai (1983), and by the more recent work by Lima and Santos (2016). In the above aforementioned works a point heat source, surface heat source and volumetric heat source were used, respectively. In addition as suggested by Goldak et al. (1984), the distance in front of the heat source can be taken as one-half of the weld width and the distance behind the heat source may assume the value of twice the width.

If one needs to model a weld bead with a shape different from an ellipsoidal volume, Goldak's DEHS model turns out to be a non-optimal choice. Hence others models must be chosen as in the case of modeling Laser Beam Welding (LBW) as well as Electron Beam Welding (EBW) process where deeper penetration can be achieved.

García-García et al. (2016) established a mathematical model for an autogenous GTAW thermal field by making use of the commercial package ANSYS Fluent, which is based under the FVM approach. In their work, they developed a novel volumetric moving heat source model based upon an elliptic paraboloid geometry in order to represent shallow and deep penetration as well as wide and narrow FZ. Estimated thermal history as well as predicted shape of weld bead were in good agreement with experimental measures.

In light of the importance of the heat source modeling, as stressed out by Lindgren (2007), in many situations, it is reasonable acceptable that only the correct amount of heat as function of the time and space is inputted in the model. In addition, thermal field response of regions far enough of the molten weld pool has little or no dependence of the heat source geometry (Flint et al., 2018).

2.4 In-service and conventional welding computational analysis

The numerical analysis performed in pipes with or without fluid flow assumes basically the same procedure which has been applied to plates or any kind of structure. Hence, all considerations previously observed including the simplified results obtained by using a 2D model, for instance, can be applied to in-service welding computational analysis. However, one must pay attention to details that is intrinsically for each process being analyzed.

Amongst a great variety of welding processes, Gas Tungsten Arc Welding (GTAW) also referred as TIG (Gas Tungsten Welding) is one of the most important processes concerning both research and industrial applications. GTAW may or may not (Autogenous GTAW) make use of filler metal; it is important to mention that autogenous GTAW is especially important in applications that involves thin plates being welded in butt joint configuration. In addition, the lack of filler material makes the process easier for both implementing and analyzing from numerical point of view. Also, girth welding simulation using an autogenous process can be considered an intermediary step for validating in-service welding numerical codes due to the simple aspects of this process.

Kou and Le (1984) carried out theoretical and experimental studies concerning the heat flow during welding on pipes. Their work was made upon a 3D finite difference analysis for unsteady heat flow during an autogenous GTAW girth welding. The results achieved in the numerical analysis were in good agreement with the experimental ones. In addition, the study aimed to provide optimum conditions for girth welding such as uniform weld beads and absence of defects such as lack of fusion.

Modeling single or multi-pass welding include an additional challenge for correctly attach real welding conditions to a given numerical simulation, this is due to the necessity of addition of filler metal. The elements representing the filler material are included in the model by the process of activation or deactivation which depend on the moment of the simulation (filler metal being or not present). According to Lindgren (2007) two different approaches can handle this task, namely, the *quiet* and the *inactive* element approaches. Both approaches were compared in Lindgren et al. (1999) and the results showed that they work equally well.

The quiet element technique assumes that when a given element has not yet been filled, it assumes low thermal conductivity value so that even though that element is presented in the model a priori, it remains inactive. Therefore, the elements which are in front of the arc welding keep inactive until the front of the heat source enters the element. It is important to mention that only when the heat source encounters the inactivated elements the thermal conductivity is changed. After that, at each time step, the heat source reaches the inactivated filler material deposition is properly deposited, and the thermophysical properties of these activated element assumes values similar to those material at melting point. Contrary to the quiet element approach, the inactive one just assembles the elements when the corresponding filler material is added. Therefore, the system of equations which forms the whole model must be recomputed every time step a new element is activated, (Lindgren et al. 1999).

Karlsson and Josefson (1990) through a three-dimensional FE analysis investigated temperature, stresses, and deformations in a single-pass butt-welded pipe. According to the authors this kind of simulation can be applied not only to welding pipes but also to power stations, offshore structures, and in others industry applications. In that study, they made use of a coarse mesh and relatively large time-steps. However, in spite of that, they found satisfactory results for both thermal and mechanical models.

Taylor et al. (2002), used the cell-center Finite-Volume Method to model the welding phenomena such as the weld pool fluid flow, heat transfer, and phase change. In addition, a vertex-based approach was employed for analyzing the thermo-elasto-plastic distortion of a girth welding. PHYSICA integrated modeling framework was used in their FVM study in conjunction with unstructured meshes. The approach was validated against analytical, numerical, and experimental results and good agreements between all the investigated approaches were verified.

In order to simplify numerical simulations in circumferential pipe welding, authors have been making use of both axisymmetric and 3D shell models. Axisymmetric models are useful as explained before for cross-sectional model, whereas the applicability of 3D shell models is used in most of the cases to thin-walled structures being welded. These two types of models are illustrated in Fig. 2.13.

Figure 2.13 – axisymmetric and 3D shell models.

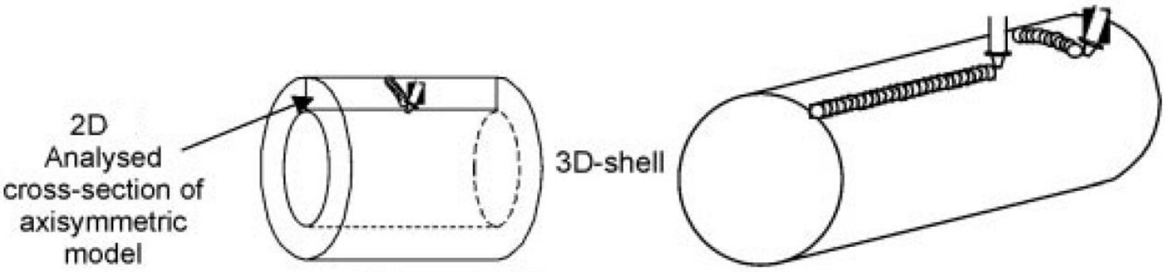

Source: Lindgren, 2007.

Deng and Murakawa (2006) developed both 2D and 3D thermomechanical FE models using the commercial software ABAQUS in order to simulate temperature fields and residual stress in multipass welds in a SUS304 stainless steel pipe. The results were validated with experimental data. Based on the 3D simulations, they observed a steady-state regime during the welding (except for run-on and run-off effects), and consequently, the results appear to be independent of the circumferential direction. Therefore, the axisymmetric 2D model also showed good agreement with the experimental results and could drastically reduce the computational time of simulation.

For having initial insights into the risk of burn-through during in-service welding and consequently make welding operations under safe limits, researchers have been used the Battelle computer-based software (Jaske et al., 2006). Battelle software can predict both cooling rates and inner surface temperature as function of welding parameters, geometric parameters, and operating conditions. Usually the limits for prevent burn-through and satisfy the safe operating conditions are avoid with inner surface temperature equal or bellow 982 °C, for low-hydrogen electrodes, and 760 °C, except for cellulosic electrodes, and keep maximum tolerable hardness at HAZ below 350 HV (Hardness Vickers). Some shortcomings makes the Battelle a limited software: use of a two-dimensional model, able to perform single pass simulation only, use of coarse meshes (limited number of elements), neglecting of existing thermal stress and mechanical stresses due to internal pipe pressure, point heat source, and the non-user-friendly interface (Jaske et al., 2006; Lima and Santos, 2016). On the other hand, currently FEM and FVM simulations in in-service welding processes can overcome all these drawbacks. Majnoun et al. (2021) have developed a new thermo-mechanical FEM approach in order to predict temperature and stress distribution in the welding of a T-shape pipe joint. They presented some results that even though the Battele simulator criteria were satisfied there was a high risk of burnthrough occur.

The myriad of processes as well as welding parameters make each simulation in welding area unique. One of the most important required abilities in a given welding analysis (in-service or not) is a proper representation of welding heat source. According to Sabapathy et al. (2001), a number of modifications must be performed in (Double-Ellipsoid Heat Source) DEHS model in order to correct approximate the out-of-position low-hydrogen SMAW process. For this reason, they proposed a new mathematical model of the heat source aiming to model the common in-service welding. In this new approach, a modification of DEHS model was made by changing the exponential terms in the previous model (Sabapathy et al., 2001). This was performed in order to mimic the weave technique often applied with MMAW in in-service welding operations. Finally, they analyzed welding cooling rates (Δt_{8-5}) and reasonable agreement was found when confronted against experimental data.

In order to represent hot-tapping on pipelines, Lima and Silva (2016) came up with a novel mathematical approach by adapting the DEHS model and also, they proposed an analytical methodology for estimates the size and shape of the molten pool. Despite good agreement with experimental results, the authors stressed out that the model needs to be validated by the variation of all extreme welding parameters.

Recently, Tahami et al. (2019) also developed a FEM model based on a new approach of a heat source model in order to model an in-service welding of a T-shape joint (direct branch on pipe) steel pipe connection. The parameters investigated were heat input, welding speed, pipe wall thickness, turbulent fluid flow parameters, material properties. In conjunction with experimental studies, the numerical results formed a computer-code based on neural network algorithms for predicting temperature levels for different welding conditions. The new model was based upon the Goldak's DEHS model in order to simulate a MMAW in-service welding process made in a saddle geometry (direct branch on pipe). The T-shape joint is illustrated in Fig. 2.14.

Figure 2.14 – 3D FE model for T-branch weld. Goldak's DEHS model.

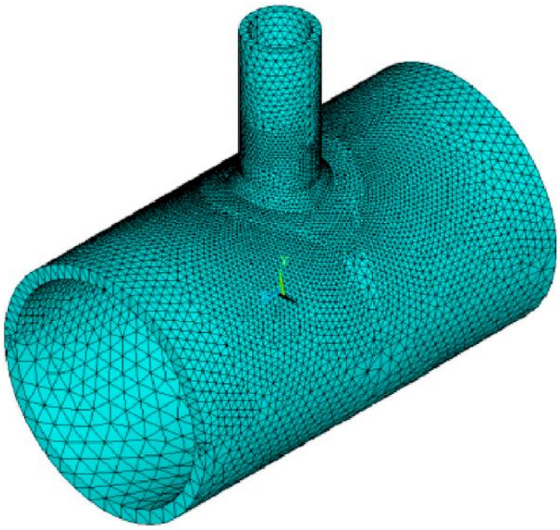

Source: Tahami et al. (2019).

The less time is consumed during in-service welding, the safer will be the operation for the crew; this is due to the severe and unsafe conditions that is encountered during this process. By performing both a 3D and a 2D axisymmetric FE thermomechanical analysis in a circumferential sleeve repair, Alian et al. (2016) observed the influence of the number of welders, their positions, and welding directions under induced residual stresses and corresponding distortions. Four different schemes were used, as shown in Fig. 2.15. Readers may also be referred to Fig. 2.2.

Figure 2.15 – Welding schemes considered in the work by Alian et al.

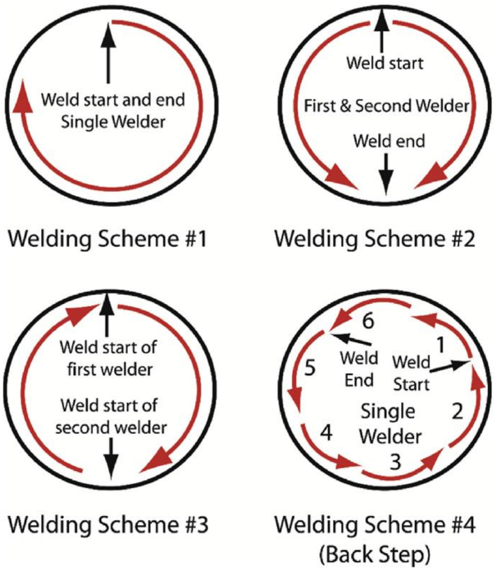

Source: Alian et al. (2016).

They validated their numerical code using experimental girth welding test data from literature. Despite the validation for both models were in satisfactory agreements, the axisymmetric model of the sleeve repair welds did not showed good agreements compared to 3D models when used to predictthe residual stresses and distortions. In addition, according to the obtained results, the authors could conclude that the back-step scheme gave the lowest average residual stress along the pipe circumference so that they recommended this scheme for in-service welding sleeve repair.

2.5 Internal pipe fluid flow

Due to the importance of assess information about the internal pipe pressure as well as cooling rates during the fluid flow into pipelines under welding operations, the inclusion of flow modeling is of vital importance in such welding process. The internal fluid flow inside pipelines may present nonlinearities, inherently instabilities, anisotropy, three-dimensional character, and statistic aspects (Wilcox, 2006), which makes it essentially turbulent.

When fluid flows are controlled by viscous diffusion, they are called laminar flows, and the Reynolds number (Re) (more details about Re will be discussed in section 3.3) is in general small. As Reynolds number increases, (for internal pipe flows this transition occurs between $Re = 2300$ and $Re = 10^4$) the inertia terms overcome the viscous stresses, and consequently rapid velocity and pressure fluctuation appear in the fluid flow and the motion becomes inherently three-dimensional and unstable, which can be described as a turbulent flow (Wilcox, 2006).

The calculation of the Re number during in-service welding repairs in pipelines as well as hot-tapping operations shows that Re may present values greater than 10^5. Therefore, the internal fluid flow in the in-service welding due to the combination of high Re values and remote area location can be classified as a turbulent fully-developed flow (Sabapathy et al., 2001).

The unsteady Navier-Stokes equations are capable of computing the smallest length and time scales of turbulence. However, these calculations are not feasible in terms of computing resources, since temporal and spatial grids need to be sufficiently fine in order to resolve all turbulent scales. Besides, for practical engineering applications the assessment of smaller eddies when compared to the larger eddies are not important.

One way to predict numerically the turbulent flow is by making use of Reynolds Averaged Navier-Stokes (RANS) methods. RANS is based on averaging the equations of motion, which results in a set of partial differential equations. In spite of having some limitations, due to the averaging process, up to date the RANS models are still the first choice when numerical modeling of turbulent fluid flow is required. However, for using this method, Computational fluid Dynamics (CFD) is required. Therefore a cumbersome and complex analysis is required to be implemented.

An alternative to the use of CFD is the use of non-dimensional empirical correlations. For in-service welding analysis, the most common used correlations are the dimensionless Dittus-Boelter equation and the Sieder and Tate equation (Incropera and DeWitt, 1990). These correlations will be better discussed in section 3.2.1. It is worth to mention that in-service welding, researchers have been following this tendency since these aforementioned empirical correlations have been massively employed by them in order to account for internal turbulent flow phenomenon (Alian et al., 2016; Sabapathy et al., 2001).

Finally, it worth to stress that Sabapathy et al. (2002) performed a sensitivity analysis of the Sieder and Tate dimensionless thermal model in order to accurate determine the heat transfer coefficient for turbulent flow in a circular pipe. From this investigation, some conclusions were able to be drawn. For instance, the variation of weld cooling rate was $\pm 4\%$, the variation of maximum HAZ depth was $\pm 3\%$, and the variation of penetration depth was considered to be negligible. Therefore, through the aforementioned observations, the author could prove the accuracy of the use of such dimensionless correlations in in-service welding numerical analysis.

2.6 Mechanics of the welding

During the welding process a high localized heat source act upon the workpiece, which also depend on the process conditions, as for instance, the cooling rates during the welding process. In addition, we may observe that a small region is subjected to high temperatures and a large surrounding area is kept at low temperature. The aforementioned conditions cause expansions and contractions due to the thermal loads (heating and cooling) as well as mechanical loads which is imposed by restrictions and internal pressure in the case of in-service welding process. After the cooling process, the workpiece may experience undesirable conditions such as welding residual stress and shape changes in the structure (plastic deformations). Brickstad and Josefson (1998) stressed out that the amount of residual stresses in piping system can be more deleterious than stresses caused by the design loads such as internal pressure and reaction forces at the supports.

According to Radaj (1992), residual stresses are self-equilibrating internal forces without the influence of external forces which are originated from plastic deformations and may act temporarily or permanently. In the context of welding processes, residual stresses may also be called thermal stresses due to the non-uniform temperature changes (Kou, 2003). The distribution of welding residual stresses may be affected by several factors such as structural dimensions and their restraints, material properties, heat source, number of welding passes, and welding sequence (Brickstad and Josefson, 1998; Deng and Murakawa, 2006). The authors also cited the main problems that welding residual stress may cause: hydrogen-induced cracking, fatigue damage, stress corrosion cracking, and brittle fracture. Therefore, the proper prediction and correction of welding residual stress is mandatory in any manufactory welding process in order to eliminate or at least minimize them.

Prasad et al. (2016) used a 3D FEM parametric analysis to study the effects of welding parameters on residual stress during circumferential TIG welding of pipes. They concluded that the higher the current from the arc welding the wider range of axial residual stresses. Furthermore, they also noted that the residual stresses near the welding line change from compressive to tensile from outer to inner surface. Similar results concerning the profile of axial residual stresses through the pipe wall thickness were also observed by Deng and Murakawa (2006) and Silva and Farias (2008). Typical results by Deng and Murakawa (2006) are shown in Fig. 2.16.

Figure 2.16 – Residual axial stresses at outer (a) and inner surfaces (b).

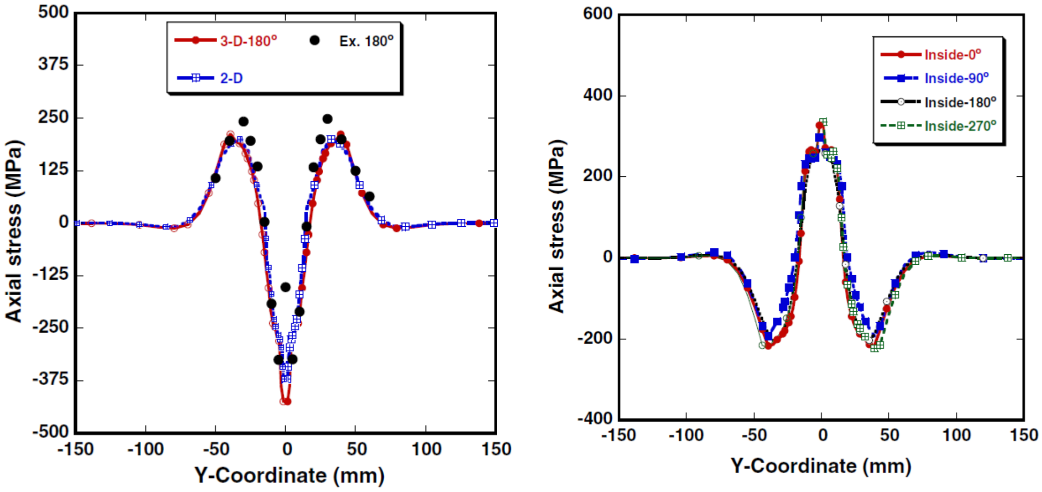

(a) (b)

Source: Deng and Murakawa, 2006.

The results presented in Fig. 2.16 is typically found in the welded pipes. The residual axial stresses in the pipes change to compressive on the outer surface to tensile on the inner surface. This phenomenon (shown in Fig. 2.17) is due to the shrinkage around the pipe during the weld bead cooling and is the so-called tourniquet effect (Law et al., 2006).

Figure 2.17 – Tourniquet effect around the welded pipe.

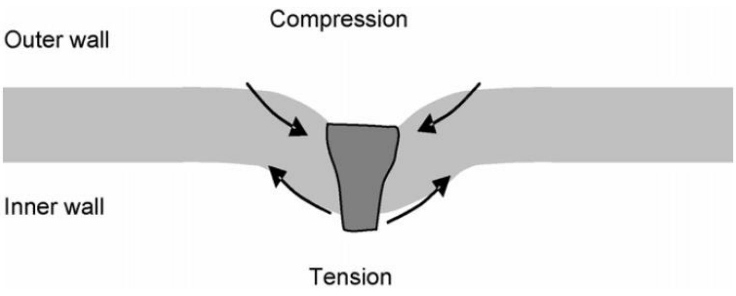

Source: Law et al., 2006.

The deformation/distortion which arises from the welding process is another important aspect that needs to be take into account during a numerical simulation. Since this undesirable defect changes the shape and dimension of the original workpiece, this alteration may compromise the performance and consequently, the main purpose of the given welded structure. Typical analysis of welding distortions by Qureshi (2008) are shown in Fig. 2.18.

Figure 2.18 – Radial displacements.

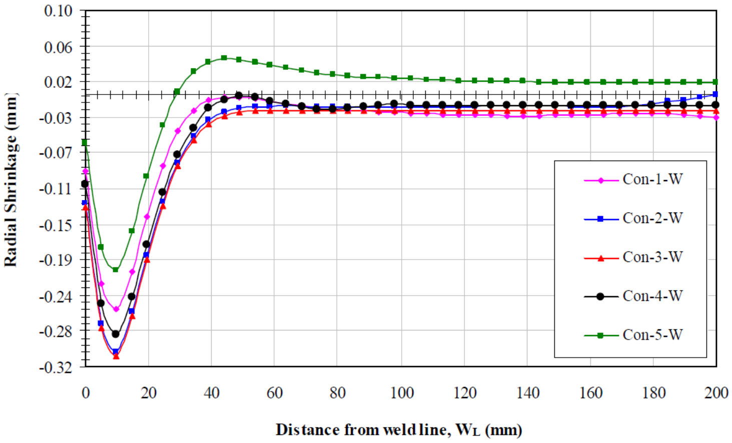

Source: Qureshi, 2008.

As the distribution of residual stresses in a given pipe is affected by many different factors, a variety of parametric studies concerning welding residual stress have been performed by many authors. Ferro et al. (2006) developed a 3D and 2D numerical model of laser beam welding of steel plates by considering the effects of phase transformation under the residual stresses. The material used was the ASTM SA 516 steel. They found out that both volume change and transformation plasticity tend to relieve high tensile stresses in the fusion zone. Sattari-Far and Farahani (2009) studied the effect of different grooves and pass numbers on residual stresses in butt-welded pipes. They showed that these two parameters may have great influence on magnitude and distribution of residual stresses in welded pipes. Molesmi et al. (2022) developed a 3D finite element model in the Sysweld commercial software. They investigated the influence of welding sequences on weld induced residual stresses and distortions in 316L stainless steel pipes. The full circumferential welding concept presented more uniform distributions of residual stresses and distortions along the circumferential direction.

CHAPTER

3

GEOMETRICAL, PHYSICAL MODEL, AND NUMERICAL INGREDIENTS

Solving the thermal energy equation as well as the momentum equations analytically is only possible for a few simplified problems such as the 2D steady-state solution of the temperature field over a thin plate, the Rosenthal's solution of the temperature field in an orthogonal domain subjected to a moving point or heat line source (Rosenthal, 1941), simple tension and simple shear applied to bodies under linear elasticity conditions, and bodies subjected to uniformly thermal loads under elasticity conditions. When we need to represent the real world processes by adding complex phenomena such as transient regime, temperature-dependent material properties, and thermo-elastoplasticity, one needs to deal with numerical methods.

Basically, by using a numerical approach, the set of partial differential equations, which mimics the real phenomena are transformed into a set of algebraic approximated equations. The set of algebraic equation needs a discrete domain for store the variables to be solved, therefore one defines a computational mesh for doing this task. A similar discretization in time is also required.

In order to guarantee the conservation of a given property, the approximated equations used by the FVM are obtained through a balance of the property being evaluated or by integration of the conservative equations over space and time. One knows that any numerical procedure that obtain their approximate equations through a material balance is a Finite Volume Method (FVM). Thus, there are different types of the aforementioned method. One of them is the Element-based FiniteVolume Method (EbFVM), denomination suggested by Maliska (2004). The latter, is a FVM that borrows from FEM the concepts of elements and shape functions that renders to the final approximate conservation equations at the discrete level.

3.1 Domain discretization

In general, a continuous physical model is described by a set of coupled differential partial equations with no analytical solution. In that case, the only remedy left behind is the numerical solution. In order to obtain a numerical solution, the domain needs to be broken into small pieces, and then forms a set of points, lines, faces, and elements, and therefore, this collection of geometrical quantities results in what we known as a mesh or grid. The mesh is a crucial step for implement any mesh-based numerical method so that care should always be taken when design the required mesh so as to obtain success in a modeling analysis. We can classify the types of meshes into two main groups: structured and unstructured meshes. One example of a 2D structured mesh (Cartesian mesh, in this example) composed of regular quadrilaterals is illustrated in Fig. 3.1.

Figure 3.1 – Structured Cartesian mesh.

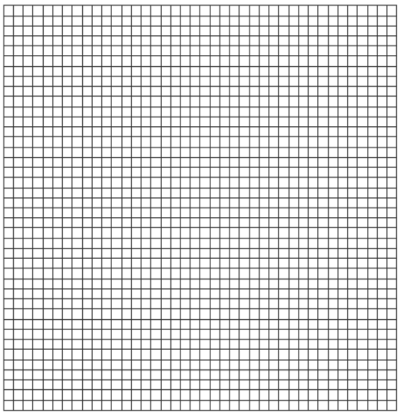

Fig. 3.2 shows a 2D unstructured mesh composed of non-uniform triangles for a welding analysis in a thin plate, where a localized refinement mesh has been performed near the patch of the arc welding (weld pool and HAZ) in order to capture the high temperature

gradients in these regions and a coarser mesh towards the base metal so as computational resources are saved.

Figure 3.2 – Unstructured mesh for a welding analysis.

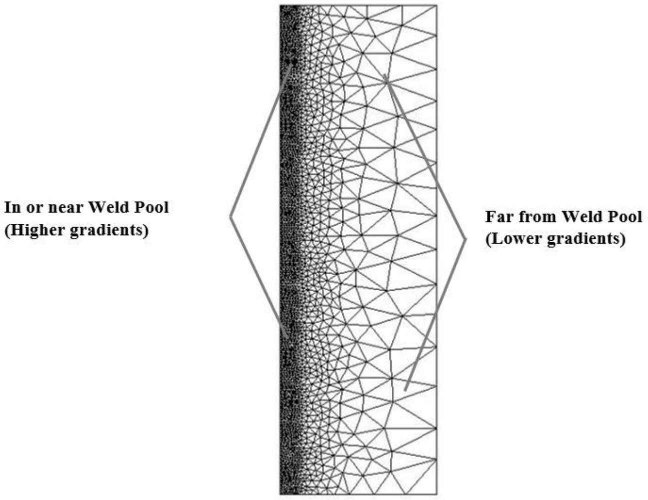

The unstructured mesh, which is identified by their irregular connectivities amongst its nodes and the absence of a specific rule for correlate mesh elements with its neighbors (Versteeg and Malalasekera, 2007; Maliska, 2004), has the ability to fit the boundaries of complex geometries, capture all the intricate details in a simulation, make the process of local refinement easier, and drastically reduce the required computational resources. Welding simulation of T-joint weld designs, branch on pipes, addition of filler metal in grooves, sleeve repair welding are some applications that can take advantage of unstructured meshes.

In the EbFVM approach the mesh can be composed of different types of elements; for 2D domain, a mesh composed of triangles, quadrilaterals or a mixed mesh composed of triangles and quadrilaterals, and for 3D domains the mesh can be composed of either hexahedral, tetrahedral, prism, and pyramid elements, or a combination of them. Nonetheless, for the sake of simplicity, a two-dimensional mesh, which is constructed with triangle and quadrilateral elements is described in Fig. 3.3. In this Figure, the blue numbers represent the elements, the sub-control volumes (sub-elements) are represented by the SCV_i, and the control volume related to the node 1 is described by the gray area.

Figure 3.3 – Unstructured mesh and vertex-based control-volume.

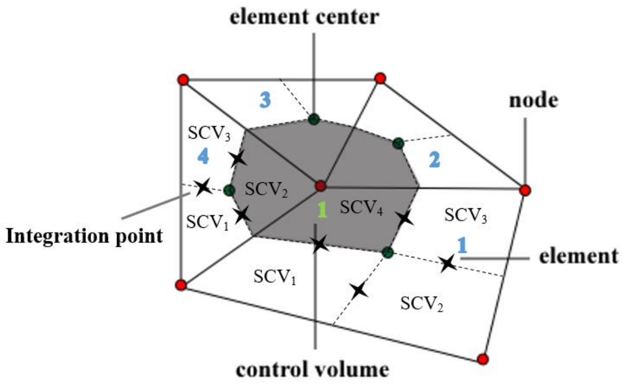

From Fig. 3.3, we can see that by joining the edge midpoints and the element centroids we can create the sub-control volumes for each element. A control volume is constructed around each node by adding the surrounding sub-control volumes that shares a node. This is called median dual method (Versteeg and Malalasekera, 2007; Ansys CFX, 2011), and gives rise to a cell-vertex approach. Finally, in general, hybrid meshes (combination of different elements) are used to better capture the physical phenomena of the problem to be solved. This approach has been successfully applied in several fields, see for instance, Marcondes et al. (2013), Pimenta (2019), and Taylor et al. (2012).

The steps of the construction of the approximated equations for each control volume is summarized as follows: the physical domain is divided into elements, and then each element is subdivided into sub-elements according to the number of nodes of each element. In general, each sub-element is called sub-control volume because the conservation equations are integrated in time and space for every sub-element. After the integration process, the equation of each control-volume is assembled visiting all sub-control volumes that share the same node. Due to its conservative aspect, conservation of properties is warranted at each finite control volume.

3.2 Global coordinate to local coordinate system

The EbFVM procedures applied to both thermal energy and linear momentum equations. Let us started by considering a general variable ϕ, and then writing the well-known transport equation as follows:

$$\frac{\partial\left(\rho\phi\right)}{\partial t}+\nabla\cdot\left(\rho\phi\mathbf{v}\right)=\nabla\cdot\left(\Gamma\nabla\phi\right)+S_{\phi} \tag{3.1}$$

Eq. (3.1) represents the conservation of the property ϕ at every point in a specified domain. The first term in the left-hand side is the time rate of change of ϕ, the second one is the net rate of ϕ transferred by advection through the domain surface; in the right-hand side, the first term is the net rate of ϕ transferred by diffusion through the domain surface and the second one is the rate of increase of ϕ due to source terms. The latter is related to the conversion of some types of internal energy such as chemical and electrical to thermal energy (Incropera and DeWitt, 1990).

The set of equations which will arise from the process of discretization results in a closed system of variables stored in the mesh nodes; therefore, in order to obtain the values all over the elements (the entities where most calculations are performed), interpolation functions need to be defined so that values at the integration points, for example, can be calculated. As we verify in Eq. (3.1), one can associate physical meaning for all the terms that compose this equation. The troublesome terms for treating numerically are the diffusion and advective terms, both associated with the flow crossing the element interfaces.

Diffusion terms do not pose numerical instabilities when interpolation schemes are applied to interpolate physical properties from the nodes to any part of the element (owing to their elliptic behavior); on the other hand, care should be taken when advective terms are involved. The use of non-exact interpolation functions gives rise to truncation errors. When these errors are associated with advective terms, numerical oscillation and numerical diffusion errors are yielded (Maliska, 2004). The advective terms are represented by the second term in the left-hand side of Eq. 3.1. However, as long as this term is not accounted in the problem (like the present study for both thermal energy and linear momentum equations), we do not need to address the aforementioned errors.

For treating diffusion terms, EbFVM borrows the idea usually implemented in Finite Element Method (FEM) by adopting polynomial function for interpolating variables into the elements; these functions are the so-called shape functions. For connecting the physical mesh (physical domain, frequently with distorted elements) with a local mesh (transformed domain), one may use mapping. Through the use of mapping, it is possible to do a parallelism between global equations and local ones. The equations responsible for evaluating each geometric position and each physical property ϕ within each element are defined by

$$x(s,t,p)=\sum_{i=1}^{n_v} N_i x_i \tag{3.2}$$

$$y(s,t,p)=\sum_{i=1}^{n_v} N_i y_i \tag{3.3}$$

$$z(s,t,p)=\sum_{i=1}^{n_v} N_i z_i \tag{3.4}$$

$$\phi(s,t,p)=\sum_{i=1}^{n_v} N_i \phi_i \tag{3.5}$$

where (x_i, y_i, z_i) are the Cartesian coordinates, (s,t,p) is the computational coordinates, n_v is the number of vertices of each element, N_i denotes the shape functions, and ϕ_i represents the physical properties stored at the nodes of the elements.

As previously mentioned, one may deal with different types of elements. In the present study hexahedral elements is used for representing three-dimensional geometries except in a few test cases where tetrahedrons and prisms are used. Since the majority of simulated test cases as well as the in-service welding analysis made use of hexahedron-based meshes, we will focus our analysis in this specific type of element. Therefore, Fig. 3.4 shows an irregular hexahedron being mapped to a regular hexahedron into a transformed space (*s,t,p*), where each axis in the transformed plane varies from -1 to 1.

Figure 3.4 – Distorted element, transformed element, and sub-element (sub-control volume).

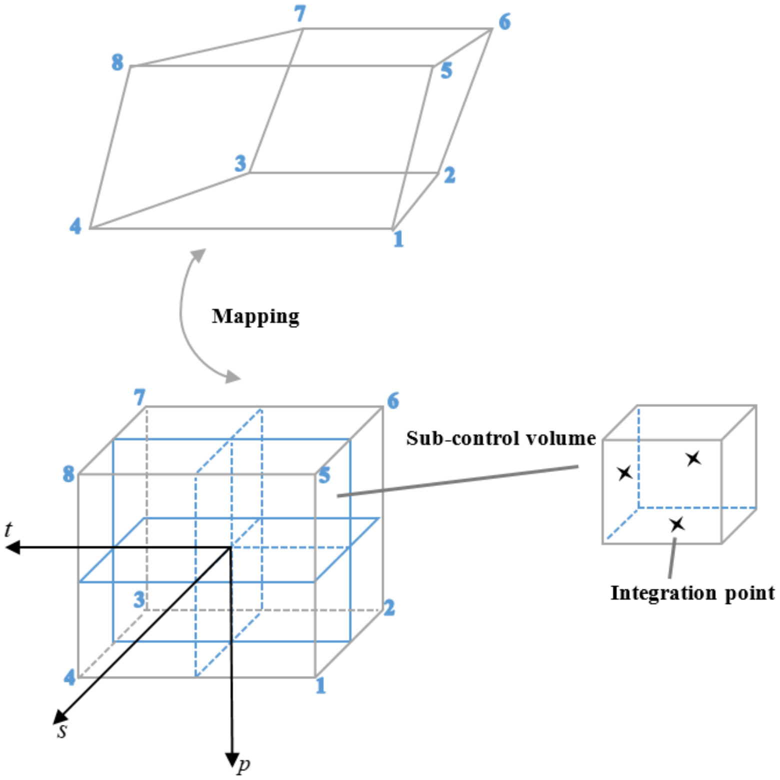

In order to perform the coordinate transformation, the eight tri-linear shape functions for each node of the hexahedral element are given by

$$N_1(s,t,p)=\frac{(1+s)(1-t)(1+p)}{8} \tag{3.6}$$

$$N_2(s,t,p)=\frac{(1-s)(1-t)(1+p)}{8}, \tag{3.7}$$

$$N_3(s,t,p)=\frac{(1-s)(1+t)(1+p)}{8} \tag{3.8}$$

$$N_4(s,t,p)=\frac{(1+s)(1+t)(1+p)}{8} \tag{3.9}$$

$$N_5(s,t,p)=\frac{(1+s)(1-t)(1-p)}{8} \tag{3.10}$$

$$N_6(s,t,p)=\frac{(1-s)(1-t)(1-p)}{8} \tag{3.11}$$

$$N_7(s,t,p)=\frac{(1-s)(1+t)(1-p)}{8} \tag{3.12}$$

$$N_8(s,t,p)=\frac{(1+s)(1+t)(1-p)}{8} \tag{3.13}$$

The diffusion terms are related to gradients of ϕ, therefore, we can evaluate these gradients taking the derivative of Eq. (3.5) with respect to global coordinates as follows:

$$\frac{\partial \phi}{\partial x}=\sum_{i=1}^{n_v}\frac{\partial N_i}{\partial x}\phi_i \tag{3.14}$$

$$\frac{\partial \phi}{\partial y}=\sum_{i=1}^{n_v}\frac{\partial N_i}{\partial y}\phi_i \tag{3.15}$$

$$\frac{\partial \phi}{\partial z}=\sum_{i=1}^{n_v}\frac{\partial N_i}{\partial z}\phi_i \tag{3.16}$$

In Eqs. (3.14) – (3.16), one has shape functions derivatives with respect to global coordinates (x,y,z). However, the shape functions are described in terms of local coordinates (s,t,p), please refer to Eqs. (3.6) through (3.13). In order to evaluate the derivatives in Eqs. (3.14) – (3.16) with respect to *x*, *y*, and *z*, it is necessary to apply the chain rule, which result in the following expressions for derivatives of shape function with respect to the global coordinates (x,y,z) in terms of local coordinates (s,t,p):

$$\frac{\partial N_i}{\partial x}=\frac{1}{det(J)}\left[\left(\frac{\partial y}{\partial t}\frac{\partial z}{\partial p}-\frac{\partial y}{\partial p}\frac{\partial z}{\partial t}\right)\frac{\partial N_i}{\partial s}-\left(\frac{\partial y}{\partial s}\frac{\partial z}{\partial p}-\frac{\partial y}{\partial p}\frac{\partial z}{\partial s}\right)\frac{\partial N_i}{\partial t}+\left(\frac{\partial y}{\partial s}\frac{\partial z}{\partial t}-\frac{\partial y}{\partial t}\frac{\partial z}{\partial s}\right)\frac{\partial N_i}{\partial p}\right] \tag{3.17}$$

$$\frac{\partial N_i}{\partial y}=\frac{1}{det(J)}\left[-\left(\frac{\partial x}{\partial t}\frac{\partial z}{\partial p}-\frac{\partial x}{\partial p}\frac{\partial z}{\partial t}\right)\frac{\partial N_i}{\partial s}+\left(\frac{\partial x}{\partial s}\frac{\partial z}{\partial p}-\frac{\partial x}{\partial p}\frac{\partial z}{\partial s}\right)\frac{\partial N_i}{\partial t}-\left(\frac{\partial x}{\partial s}\frac{\partial z}{\partial t}-\frac{\partial x}{\partial t}\frac{\partial z}{\partial s}\right)\frac{\partial N_i}{\partial p}\right] \tag{3.18}$$

$$\frac{\partial N_i}{\partial z}=\frac{1}{det(J)}\left[\left(\frac{\partial x}{\partial t}\frac{\partial y}{\partial p}-\frac{\partial x}{\partial p}\frac{\partial y}{\partial t}\right)\frac{\partial N_i}{\partial s}-\left(\frac{\partial x}{\partial s}\frac{\partial y}{\partial p}-\frac{\partial x}{\partial p}\frac{\partial y}{\partial s}\right)\frac{\partial N_i}{\partial t}+\left(\frac{\partial x}{\partial s}\frac{\partial y}{\partial t}-\frac{\partial x}{\partial t}\frac{\partial y}{\partial s}\right)\frac{\partial N_i}{\partial p}\right] \tag{3.19}$$

where $det(J)$ is the Jacobian of the transformation, which is given by

$$det(J)=\left(\frac{\partial y}{\partial t}\frac{\partial z}{\partial p}-\frac{\partial y}{\partial p}\frac{\partial z}{\partial t}\right)\frac{\partial x}{\partial s}-\left(\frac{\partial y}{\partial s}\frac{\partial z}{\partial p}-\frac{\partial y}{\partial p}\frac{\partial z}{\partial s}\right)\frac{\partial x}{\partial t}+\left(\frac{\partial y}{\partial s}\frac{\partial z}{\partial t}-\frac{\partial y}{\partial t}\frac{\partial z}{\partial s}\right)\frac{\partial x}{\partial p} \tag{3.20}$$

The Jacobian matrix can be defined using a matrix notation as

$$J\left(s,t,p\right)=\begin{bmatrix} \dfrac{\partial x}{\partial s} & \dfrac{\partial y}{\partial s} & \dfrac{\partial z}{\partial s} \\ \dfrac{\partial x}{\partial t} & \dfrac{\partial y}{\partial t} & \dfrac{\partial z}{\partial t} \\ \dfrac{\partial x}{\partial p} & \dfrac{\partial y}{\partial p} & \dfrac{\partial z}{\partial p} \end{bmatrix} \tag{3.21}$$

For more information about the numerical procedure described in this section see for instance (Maliska, 2014; Marcondes et al., 2013).

3.3 Thermal model

3.3.1 Thermal energy equation

Thermal energy equation is derived from the first law of thermodynamics, where one describes energy being conserved by an energy balance. By assuming that the conductive heat fluxes are expressed by the Fourier’s law, the partial differential equation, Eq. (3.1), which can model most of the problems concerning the welding processes can be rewritten as

$$\frac{\partial\left(\rho cT\right)}{\partial t}+\nabla\cdot\left(\rho cT\mathbf{v}\right)=\nabla\cdot\left(k\nabla T\right)+Q_S \tag{3.22}$$

Despite being an important source of heat transferred in the molten pool (Rykalin and Beketov, 1967), the advective term in the left-hand side which is responsible for modeling the fluid motion in the welding pool may be neglected in order to reduce the complexity of the model. Many authors (Sabapathy et al., 2001; Anca et al. 2011) have approximated this term by increasing the thermal conductivity in regions, where liquid phase is expected to appear. Therefore, the thermal distribution with phase change during the melting/solidification arc welding process can be outlined by the following nonlinear unsteady heat conduction equation:

$$\frac{\partial\left(\rho c T\right)}{\partial t}=\nabla\cdot\left(k\nabla T\right)+Q_S \tag{3.23}$$

where T is the temperature, $k=k\left(T\right)$ is the isotropic (non-dependent of the coordinate direction) thermal conductivity, $\rho=\rho\left(T\right)$ denotes the material density, $c=c\left(T\right)$ is the specific heat coefficient, and $Q_S=q\left(\boldsymbol{r},t\right)-q_L\left(T,t\right)$**,** where $q=q\left(\boldsymbol{r},t\right)$ denotes the surface or volumetric heat input which is originated from the arc welding and $q_L=q_L\left(T,t\right)$ is the term that takes into account the absorption or release of latent heat as a result of the heating or cooling of the workpiece being welded. The term concerning the latent heat can be expressed by the following expression:

$$q_L=\rho L\frac{\partial f_L}{\partial t} \tag{3.24}$$

where L is the latent heat and f_L denotes the liquid fraction that is defined as

$$f_L=\begin{cases}0 & for\ \ T<T_{sol}\\ \dfrac{T-T_{sol}}{T_{liq}-T_{sol}} & for\ \ T_{sol}\le T\le T_{liq}\\ 1 & for\ \ T>T_{liq}\end{cases} \tag{3.25}$$

where T_{sol} and T_{liq} denote the *solidus* and *liquidus* temperature, respectively used to take into account an extended (non-isothermal) range for phase change (mushy zone). The fact that f_L is a linear temperature function inside the phase change interval is equivalent to assume that latent heat is uniformly released/absorbed into the mushy zone (Fachinotti et al., 1999).

By applying the chain rule to Eq. (3.24) and substituting the result into Eq. (3.23), one obtains

$$\frac{\partial\left(\rho c_{eff} T\right)}{\partial t} = \nabla \cdot \left(k \nabla T\right) + q \tag{3.26}$$

where c_{eff} denotes the effective specific heat coefficient, which is defined as

$$c_{eff} = c + L\frac{\partial f_L}{\partial T} \tag{3.27}$$

By invoking Eq. (3.25), the effective specific heat coefficient can be recast as

$$c_{eff} = \begin{cases} c & for \;\; T < T_{sol} \\ c + \dfrac{L}{T_{liq} - T_{sol}} & for \;\; T_{sol} \le T \le T_{liq} \\ c & for \;\; T > T_{liq} \end{cases} \tag{3.28}$$

Finally, it is worth remembering that in Eq. (3.28) we have $c = c(T)$. In addition, from Eq. (3.28) one may infer that in the mushy zone the specific heat coefficient is artificially increased so as the latent heat is take into account (Thomas et. al., 1984).

3.3.2 Initial and boundary conditions

The thermal problem requires the solution of Eq. (3.23) along with proper initial and boundary conditions. As one knows the quality of a simulation is strongly affected by initial and boundary conditions, therefore, we must carefully choose them according to previous experimental observations.

In the present study three conventional types of boundary conditions were used and they can be extracted from the Fig. 3.5. For the sake of simplicity, one made use of a 2D Cartesian coordinate system.

Figure 3.5 – Thermal boundary conditions.

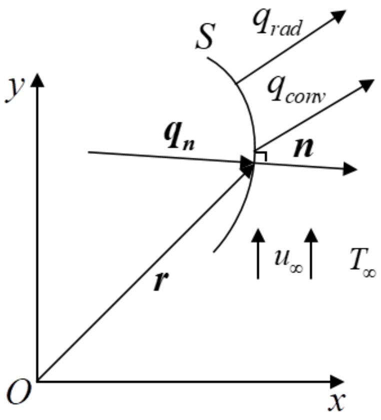

The first condition adopted was the Dirichlet boundary condition or boundary condition of the first kind. In this situation, one keeps the surface S at a fixed temperature T_s, and therefore we can mathematically express this condition by

$$T(\boldsymbol{r},t)=T_s \tag{3.29}$$

The above-mentioned boundary condition was applied just for a few test cases. The second and third boundary conditions were applied to all welding simulations and they are obtained by applying an energy balance at the surface of the medium. The external surfaces of the material being welded is either adiabatic surface or heat losses by natural or forced convection can be evaluated through Newton's law of cooling. The two aforementioned conditions are represented by Eqs. (3.30) and Eq. (3.31), respectively.

$$\left.\frac{\partial T}{\partial \mathbf{n}}\right|_s=0 \tag{3.30}$$

$$-k\left.\frac{\partial T}{\partial \mathbf{n}}\right|_s = h\left[T_\infty - T\left(\mathbf{r},t\right)\right] \tag{3.31}$$

where ***n*** is the unit outward normal vector to the surface *S* at a point located by the vector ***r***, and T_∞ is the environment temperature. Eq. (3.30) represents a Neumann boundary condition or boundary condition of second kind, and Eq. (3.31) is known as a third boundary condition type. When we have a quiescent environment, *h* is the sum of the heat transfer coefficient by natural convection h_{nc} and the heat transfer coefficient by thermal radiation h_r, which can be stated by

$$h = h_{nc} + h_r \tag{3.32}$$

where h_r is the result from the linearization of the Stefan-Boltzmann equation and is represented as follows:

$$h_r = \sigma\varepsilon\left[T\left(\mathbf{r},t\right) + T_\infty\right]\left[T\left(\mathbf{r},t\right)^2 + T_\infty^2\right] \tag{3.33}$$

where σ is the Stefan-Boltzmann constant and ε is the thermal emissivity. Heat loss provided by thermal radiation is mainly important at higher temperature regions such as welding zone and HAZ, where temperatures is near or higher than the melting temperature, whereas the heat loss provided by natural convection is dominating at region far from the welding line (Obeid et al., 2017).

When the designed system has some kind of external means providing the fluid flow, such as the fluid flow in a given pipeline, one has forced convection. The exchange of heat between the workpiece being welded and the medium under flowing is given via the forced convection heat transfer coefficient h_{fc} which can be calculated through the following relation

$$Nu = \frac{h_{fc}D}{k_f} = f\left(Re_D, Pr\right) \tag{3.34}$$

where Nu is the Nusselt number, D denotes a characteristic length (internal diameter), k_f is the thermal conductivity of the fluid, and Re_L (Reynolds number) and Pr (Prandtl number) are defined, respectively, as

$$Re_D = \frac{\rho u_\infty D}{\mu} \tag{3.35}$$

$$Pr = \frac{\nu}{\alpha} \tag{3.36}$$

where ρ is the fluid density, u_∞ is the fluid velocity, μ is the dynamic viscosity, ν is the kinematic viscosity and, α is the thermal diffusivity. By obtaining the forced convection heat transfer coefficient we can add it to Eq. (3.32) and model a boundary condition of fluid flow into a given pipeline. The two types of convection boundary conditions are illustrated in Fig. 3.6 for in-service welding application.

Figure 3.6 – Convection boundary conditions at pipe surfaces during in-service welding.

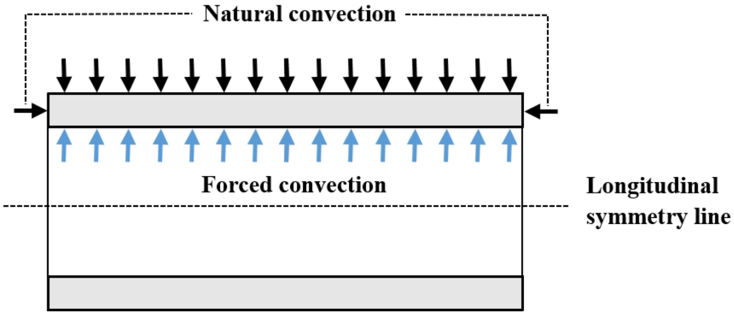

Calculation of the forced convection heat transfer coefficient can be obtained via empirical correlations. For in-service welding analysis, the most common used correlations are the dimensionless Dittus-Boelter equation (Eq. 3.37) and the Sieder and Tate equation (Eq. 3.38) (Incropera and DeWitt, 1990).

$$Nu_D = 0.023 Re_D^{4/5} Pr^{0.4} \qquad if \quad \begin{bmatrix} 0.7 \le Pr \le 160 \\ Re_D \ge 10000 \\ \dfrac{L}{D} \ge 10 \end{bmatrix} \tag{3.37}$$

$$Nu_D = 0.027 Re_D^{4/5} Pr^{1/3} \left(\frac{\mu}{\mu_s} \right)^{0.14} \qquad if \quad \begin{bmatrix} 0.7 \le Pr \le 16700 \\ Re_D \ge 10000 \\ \dfrac{L}{D} \ge 10 \end{bmatrix} \tag{3.38}$$

where *L* denotes the hydrodynamic entry length and μ_s is the viscosity of the fluid near the pipe wall.

Finally, concerning the initial temperature distribution along the medium, it is assumed that the welding model is initially at a specified value (T_0). The latter value is usually assumed to be T_∞.

$$T\left(\boldsymbol{r}, 0\right) = T_0 \tag{3.38}$$

3.3.3 Welding heat source models

Before showing the mathematical formulation for the welding heat sources, we introduce the coordinate system $\left(x, \xi, z\right)$, which follows the welding heat source, refer to Fig. 3.7.

Figure 3.7 – Coordinate system following the heat source path.

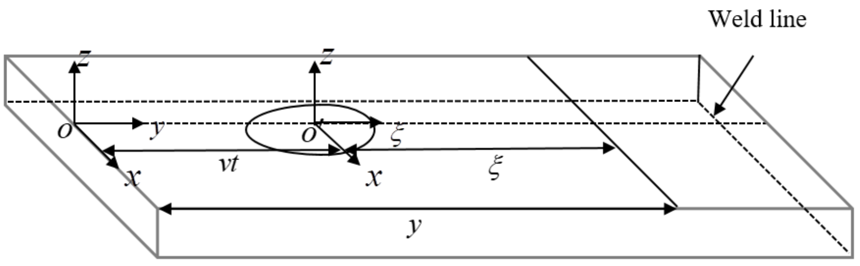

The relationship between the fixed coordinate system (x, y, z) and the local moving coordinate system (x, ξ, z) can be expressed as

$$\xi = (y - y_0) - vt \tag{3.39}$$

where the coordinates *x* and *z* are equals in both systems, (x_0, y_0, z_0) defines the position of the heat source at the initial time, and *v* is the welding speed.

Fig. 3.8 shows the considerations for the case of circumferential welding modeling. The electric arc path is described by considering that the electric arc is moving along a given *x*-*y* plane.

Figure 3.8 – Path described by the electric arc in a circumferential welding.

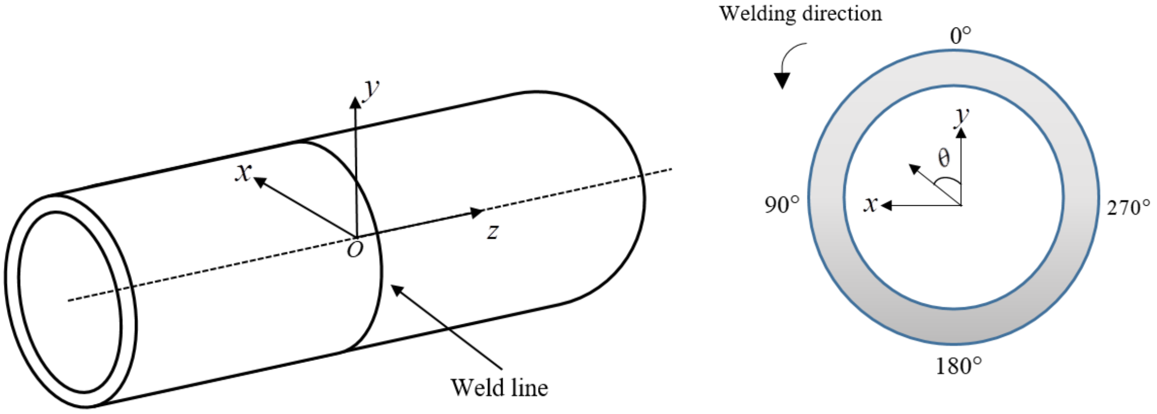

The mathematical description for modeling circumferential welding is assumed by introducing the local moving coordinates (ξ_1, ξ_2, z).

$$\xi_1 = \left(x - x_0\right) - R\sin\left(\theta\right) \tag{3.40}$$

$$\xi_2 = \left(y - y_0\right) - R\cos\left(\theta\right) \tag{3.41}$$

where R is the radial distance from the arc welding to the pipe longitudinal axis z and θ denotes the final angular position described by the torch which started from the initial angular position θ_0 and can be defined as

$$\theta = \frac{vt}{R} \tag{3.42}$$

Finally, a well-modeled welding heat source is of great importance when welding thermal analysis is performed. Thereby, in order to model the heat provided by the electric arc to the given workpiece, four types of moving heat sources have been tested. Contrary to high-density Laser Beam Welding (LBW) or Electron Beam Welding (EBW), where the depth to width ratio may achieve high values, the heat input arisen from the arc welding can be either a constant heat generation per unit area (in the case of shallow weld) or per unit volume. The following heat sources are tested in the present work: circular and double-ellipse surface flux Gaussian distributions (W/m^2), and semi-ellipsoid and double-ellipsoid volumetric flux Gaussian distributions (W/m^3). Eqs. (3.43) - (3.48) describes the aforementioned welding heat sources models applied to a given plate.

- Disc-shaped model

$$\begin{aligned} q\left(x,\xi,t\right) &= \frac{3Q}{\pi a^2} exp\left[-3\frac{\left(x-x_0\right)^2}{a^2} - 3\frac{\xi^2}{a^2}\right] && if \;\; x^2 + \xi^2 \le a^2 \\ q\left(x,\xi,t\right) &= 0 && if \;\; x^2 + \xi^2 > a^2 \end{aligned} \tag{3.43}$$

- Double-elipse model

$$q_f\left(x,\xi,t\right)=\frac{6Q}{a\pi\left(c_f+c_r\right)}exp\left[-3\frac{\left(x-x_0\right)^2}{a^2}-3\frac{\xi^2}{c_f{}^2}\right]\quad\left\{\begin{array}{l}\xi\geq 0\\ \frac{x^2}{a^2}+\frac{\xi^2}{c_f{}^2}\leq 1\end{array}\right.\tag{3.44}$$

$$q_f\left(x,\xi,t\right)=0\qquad\left\{\begin{array}{l}\xi\geq 0\\ \frac{x^2}{a^2}+\frac{\xi^2}{c_f{}^2}>1\end{array}\right.$$

$$q_r\left(x,\xi,t\right)=\frac{6Q}{a\pi\left(c_f+c_r\right)}exp\left[-3\frac{\left(x-x_0\right)^2}{a^2}-3\frac{\xi^2}{c_r{}^2}\right]\quad\left\{\begin{array}{l}\xi< 0\\ \frac{x^2}{a^2}+\frac{\xi^2}{c_r{}^2}\leq 1\end{array}\right.\tag{3.45}$$

$$q_r\left(x,\xi,t\right)=0\qquad\left\{\begin{array}{l}\xi< 0\\ \frac{x^2}{a^2}+\frac{\xi^2}{c_r{}^2}>1\end{array}\right.$$

- Semi-ellipsoid model

$$q\left(x,\xi,z,t\right)=\frac{6\sqrt{3}Q}{abc\pi\sqrt{\pi}}exp\left[-3\frac{\left(x-x_0\right)^2}{a^2}-3\frac{\xi^2}{c^2}-3\frac{\left(z-z_0\right)^2}{b^2}\right]\quad if\quad\frac{x^2}{a^2}+\frac{\xi^2}{c^2}+\frac{z^2}{b^2}\leq 1\tag{3.46}$$

$$q\left(x,\xi,z,t\right)=0\qquad if\quad\frac{x^2}{a^2}+\frac{\xi^2}{c^2}+\frac{z^2}{b^2}>1$$

- Double-ellipsoid model

$$q_f\left(x,\xi,z,t\right)=\frac{6\sqrt{3}Qf_f}{abc_f\pi\sqrt{\pi}}exp\left[-3\frac{\left(x-x_0\right)^2}{a^2}-3\frac{\xi^2}{c_f{}^2}-3\frac{\left(z-z_0\right)^2}{b^2}\right]\quad\left\{\begin{array}{l}\xi\geq 0\\ \frac{x^2}{a^2}+\frac{\xi^2}{c_f{}^2}+\frac{z^2}{b^2}\leq 1\end{array}\right.\tag{3.47}$$

$$q_f\left(x,\xi,z,t\right)=0\qquad\left\{\begin{array}{l}\xi\geq 0\\ \frac{x^2}{a^2}+\frac{\xi^2}{c_f{}^2}+\frac{z^2}{b^2}>1\end{array}\right.$$

$$q_r\left(x,\xi,z,t\right)=\frac{6\sqrt{3}Qf_r}{abc_r\pi\sqrt{\pi}}exp\left[-3\frac{\left(x-x_0\right)^2}{a^2}-3\frac{\xi^2}{c_r{}^2}-3\frac{\left(z-z_0\right)^2}{b^2}\right]\quad\begin{cases}\xi<0\\ \dfrac{x^2}{a^2}+\dfrac{\xi^2}{c_r{}^2}+\dfrac{z^2}{b^2}\leq 1\end{cases} \tag{3.48}$$

$$q_r\left(x,\xi,z,t\right)=0\quad\begin{cases}\xi<0\\ \dfrac{x^2}{a^2}+\dfrac{\xi^2}{c_r{}^2}+\dfrac{z^2}{b^2}>1\end{cases}$$

Fig. 3.9 represents the double-ellipsoid heat source model as well as its geometrical parameters in a half-geometry.

Fig. 3.9. Geometrical parameters for double-ellipsoid heat source model in a half-geometry.

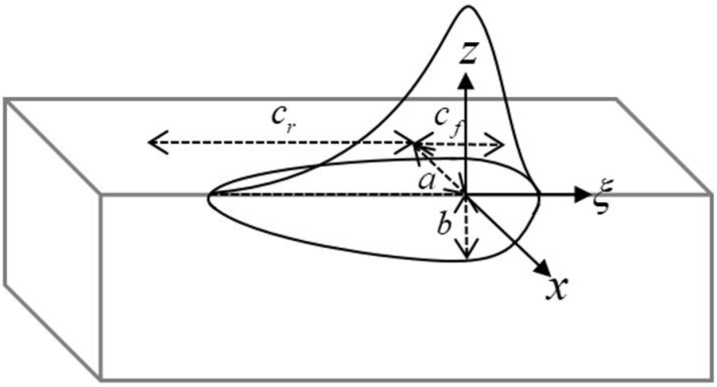

The parameters a, b, c_f, and c_r shown in Fig. 3.9 for the double-ellipsoid model are the semi-axes according to each heat distribution, f_f and f_r are the fraction of heat deposited in the front and rear quadrant of the source, respectively. In addition, it is worth mentioning that the fractions are related by $f_f + f_r = 2$ (Goldak and Akhlaghi, 2005). In the above equations, Q is the net power of the electric arc, which is defined as

$$Q=\eta UI \tag{3.49}$$

where η is the weld thermal efficiency, U *is* the arc voltage, and I is the welding current.

3.4 Mechanical model

The engineering applications concerning the solid mechanics field involves high complex nonlinearities. These nonlinearities are the result of the relation among displacement, strain, stress, and boundary conditions, being in the form of prescribed displacement or applied loads. According to Kim (2015) the sources of nonlinearities in solid mechanics can be split into four main categories: geometric nonlinearity, material nonlinearity, kinematic nonlinearity, and force nonlinearity.

Kinematic and force nonlinearities are related to the dependence of displacement and force boundary conditions on the deformations of the structure. They will not be taken into account in the present study. Therefore, only geometric nonlinearities, due to large rotations, and material nonlinearities, in the form of inelastic material behavior, will be considered in the present study.

It is important to stress out that the large deformation theory was not applied to welding analysis; the subsequent sections will be focused on the large deformation theory, since this approach had been tested and validated with some elastoplastic mechanical loadings.

3.4.1 Deformation of a solid

When a given body Ω undergoes small (infinitesimal) deformation under some applied loads, the undeformed (initial) and deformed (current) configurations present no significant difference in their shapes. A solid body under infinitesimal deformation must have both small displacement, small strain, and small rotation. Such assumptions made the numerical analysis easier to implement due to some aspects that do not need to be accounted for, e.g., whether one uses the undeformed or deformed area in defining stress. When a solid body presents either large displacement, large strain, large rotation, or a mixture of them, the deformation is said to be large (finite) deformation. In addition, for large deformation analysis we need to take into account the difference between undeformed and deformed configurations, since this difference can be sometimes even visible to the naked eye.

Fig. 3.10 shows a given body under some forces and displacements resulting in two different domains. The first one is denoted by undeformed (material) or initial domain (Ω_0) and the second one is the deformed (spatial) or current domain (Ω_x).

Figure 3.10 – Undeformed and deformed body configurations.

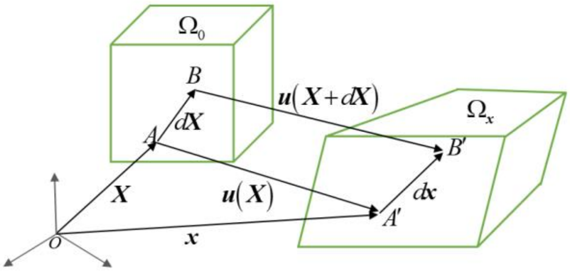

In Fig. 3.10 each point located by a vector $\boldsymbol{X}$ in the undeformed domain is unique related to a specific point located by a vector $\boldsymbol{x}$ in the deformed domain. Hence, with the aim to map the undeformed infinitesimal distance $d\boldsymbol{X}$ to the deformed infinitesimal distance $d\boldsymbol{x}$, one may define the following one-to-one relation

$$d\boldsymbol{x} = \boldsymbol{F} d\boldsymbol{X} \tag{3.50}$$

where, $\boldsymbol{F}$ is the second-order deformation gradient which provides a complete description about stretch and rigid body rotation. By relating the displacement vector $\boldsymbol{u}$ to the vector $\boldsymbol{X}$ and $\boldsymbol{x}$ we can obtain

$$\boldsymbol{F} = \frac{\partial \boldsymbol{x}}{\partial \boldsymbol{X}} = \boldsymbol{I} + \nabla_0 \boldsymbol{u} \tag{3.51}$$

where, $\boldsymbol{I}$ is the identity tensor, and $\nabla_0 \boldsymbol{u}$ is the displacement gradient at the undeformed configuration.

3.4.2 Description of meshes in solid mechanics

For solving the linear momentum equations is possible to either choose a Lagrangian or an Eulerian mesh description. According to Belitschko et al. (2014) if the mesh is Eulerian, the spatial coordinates $\boldsymbol{x}$ of the mesh nodes are fixed, which means that the nodes coincide with the spatial points, whereas if the mesh is Lagrangian, the material coordinates $\boldsymbol{X}$

of the mesh nodes are time invariant, that is, the nodes coincide with the material points. On one hand, the Eulerian approach is normally used in fluid mechanics problems since in these cases we are interested in the fluid flow over a fixed region of space; on the other hand, the Lagrangian approach is massively used in solid mechanics problems with the aim to follow the particle paths in order to determine the deformation along the domain as well as along the boundary domain (Maneeratana, 2000), and to accurately describe history-dependent materials (Belitschko et al., 2014). In light of that, the Lagrangian approach will be used in the present study.

As soon as the Lagrangian mesh description is selected, a frame of reference must be chosen where the linear momentum equations will be integrated. There are two principal choices: the first one is the undeformed geometry, which results in the so-called total Lagrangian (TL) formulation and the second one is the deformed geometry, which gives rise to the updated Lagrangian (UL) formulation (Kim, 2015). The present study will make use of the latter approach.

The UL formulation is expressed in terms of Eulerian measures of stress and strain in which derivatives and integrals are taken with respect to the deformed domain Ω_x (Belitschko et al., 2014). Furthermore, in the UL formulation the frame of reference is updated continuously as the time passes by, and all the quantities is referred to the last converged solution when new increments are required. Also, the computational mesh may move at the beginning of each load step by using the displacement increment vector $\Delta\boldsymbol{u}$ from the previous load step. Finally, after defining the frame of reference in which the integration will be performed, one needs to define a proper work conjugate stress-strain pair. In the present study the second-order Cauchy stress rate $\dot{\boldsymbol{\sigma}}$ in conjunction with the second-order rate of deformation tensor $\boldsymbol{D}$ is adopted.

3.4.3 Linear momentum equations for UL formulation

Knowing that $\boldsymbol{\sigma} = \boldsymbol{\sigma}(\boldsymbol{u})$, and $\boldsymbol{v} = \boldsymbol{v}(\boldsymbol{u})$, that is, both the Cauchy stress tensor and the velocity vector is displacement-dependent, one may write the linear momentum equations for UL formulation according to the general equation (Eq. 3.1) as follows:

$$\frac{\partial(\rho \boldsymbol{v})}{\partial t} + \nabla_{x} \cdot (\rho \boldsymbol{v}\boldsymbol{v}) = \nabla_{x} \cdot (\boldsymbol{\sigma}) + \rho \boldsymbol{b} \tag{3.52}$$

For starting the mechanical analysis and for the purposes of the present study, we first neglect body force effects, the motions by advective nature, and consider a quasi-static condition. Therefore, the partial differential equation which describes the conservation of linear momentum for UL formulation at every point in a given domain Ω_x can be described as

$$\nabla_{x} \cdot (\boldsymbol{\sigma}) = \mathbf{0} \tag{3.53}$$

where $\nabla_x \cdot (\cdot)$ is the spatial divergence of a given property defined in the current configuration. Also, the above equation can be expressed in its Cartesian system as

$$\begin{bmatrix} \dfrac{\partial \sigma_{xx}}{\partial x} + \dfrac{\partial \sigma_{xy}}{\partial y} + \dfrac{\partial \sigma_{xz}}{\partial z} \\ \dfrac{\partial \sigma_{yx}}{\partial x} + \dfrac{\partial \sigma_{yy}}{\partial y} + \dfrac{\partial \sigma_{yz}}{\partial z} \\ \dfrac{\partial \sigma_{zx}}{\partial x} + \dfrac{\partial \sigma_{zy}}{\partial y} + \dfrac{\partial \sigma_{zz}}{\partial z} \end{bmatrix} = \mathbf{0} \tag{3.54}$$

The numerical implementation of the present study is a displacement-based one, i.e., the primitive variable is the displacement vector $\boldsymbol{u}$ which means that we need to obtain a relation between the Cauchy stress and the aforementioned vector. This relation is obtained via the well-known constitute models which will be presented in section *3.4.5*.

3.4.4 Mechanical boundary conditions

For solving Eq. (3.54), we need to stablish a set of boundary conditions (BC). For mechanical displacement-based equations one has two possibilities to express the boundary conditions: essential boundary conditions (prescribed displacement) and natural boundary conditions (prescribed traction). Fig. 3.11 illustrates these BC types along a boundary domain $\partial\boldsymbol{\Omega}$ located at a given point by the vector $\boldsymbol{x}$.

Figure 3.11 – Mechanical boundary conditions.

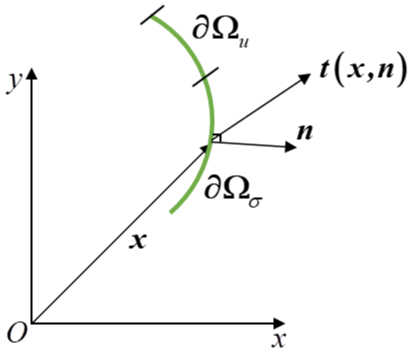

The prescribed displacement and the prescribed traction can be mathematically expressed, respectively, as follows:

$$\boldsymbol{u}=\bar{\boldsymbol{u}} \quad on \ \ \partial\Omega_u \tag{3.55}$$

$$\boldsymbol{\sigma}\cdot\boldsymbol{n}=\boldsymbol{t}=\bar{\boldsymbol{t}} \quad on \ \ \partial\Omega_\sigma \tag{3.56}$$

where $\boldsymbol{n}$ is the outward unit normal vector to the surface $\partial\Omega$ at a given point located by $\boldsymbol{x}$, and $\boldsymbol{t}$ is the surface traction vector.

3.4.5 Material behavior - constitutive models

By inspecting the behavior of materials through experimentation (one-dimensional uniaxial tensile test, for example), one may find relationships between stresses and strains, and these relations are the so-called constitutive equations. Belitschko et al., (2014) listed some important features which are of key importance when a given constitutive model is to be used:

- The main assumptions in the model development;
- The capacity of the model for modeling the material behavior;
- The model response according to load and deformation regime;
- Numerical issues of the model implementation.

One of these constitutive models is the generalized Hooke’s law, which relates each stress component through a linear combination of strains for elastic (reversible and time independent) materials (Kim, 2015). The Hooke’s law is defined as

$$\boldsymbol{\sigma} = \boldsymbol{C}{:}\boldsymbol{\varepsilon}^{\mathrm{e}} \tag{3.57}$$

where $\boldsymbol{\varepsilon}^{\mathrm{e}}$ is the second-order tensor which represents the reversible elastic strains, and $\boldsymbol{C}$ is the isotropic (after considering material symmetries) fourth-order tensor which represents the linear elastic modulus and is represented by the linear combination of Kronecker deltas as follows:

$$C_{ijkl} = \lambda\delta_{ij}\delta_{kl} + \mu\left(\delta_{ik}\delta_{jl} + \delta_{il}\delta_{jk}\right) \tag{3.58}$$

where λ and μ are the Lamé constants, which are related to the Young’s modulus E and the Poisson’s ratio ν by the following relations:

$$\lambda = \frac{E\nu}{\left(1+\nu\right)\left(1-2\nu\right)} \tag{3.59}$$

$$\mu = \frac{E}{2\left(1+\nu\right)} \tag{3.60}$$

In order to make the computer implementation more practical and by considering isotropic material and symmetry of stress and strain tensors, the Hooke’s law can be further put into Voigt’s notation. In this notation, one considers fourth-order tensor as 2D pseudo matrices and second-order tensor as pseudo vectors. Therefore, we have the following representation:

$$\begin{bmatrix} \sigma_{xx} \\ \sigma_{yy} \\ \sigma_{zz} \\ \sigma_{xy} \\ \sigma_{yz} \\ \sigma_{zx} \end{bmatrix} = \begin{bmatrix} \lambda+2\mu & \lambda & \lambda & 0 & 0 & 0 \\ \lambda & \lambda+2\mu & \lambda & 0 & 0 & 0 \\ \lambda & \lambda & \lambda+2\mu & 0 & 0 & 0 \\ 0 & 0 & 0 & \mu & 0 & 0 \\ 0 & 0 & 0 & 0 & \mu & 0 \\ 0 & 0 & 0 & 0 & 0 & \mu \end{bmatrix} \begin{bmatrix} \varepsilon_{xx} \\ \varepsilon_{yy} \\ \varepsilon_{zz} \\ 2\varepsilon_{xy} \\ 2\varepsilon_{yz} \\ 2\varepsilon_{zx} \end{bmatrix} \tag{3.61}$$

It is important to point out that in Voigt's notation the shear strain components are stored as engineering shears, i.e., twice the tensorial shears.

3.4.6 Hypoelastic-based models

The class of constitutive laws, which relates the rate of stress to the rate of deformation gives rise to the hypoelastic models. They can be described by the relation

$$\boldsymbol{\sigma}^{\nabla} = \boldsymbol{f}\left(\boldsymbol{\sigma}, \boldsymbol{D}\right) \tag{3.62}$$

where $\boldsymbol{\sigma}^{\nabla}$ represents any objective (material frame indifferent) rate of the Cauchy stress, and $\boldsymbol{D}$ is the second-order rate of deformation tensor, which is given by the symmetric part of the velocity gradient $\boldsymbol{L}$ as follows:

$$\boldsymbol{D} = sym\left(\boldsymbol{L}\right) = \frac{1}{2}\left(\boldsymbol{L} + \boldsymbol{L}^{T}\right) \tag{3.63}$$

where

$$\boldsymbol{L} = \frac{\partial \boldsymbol{v}}{\partial \boldsymbol{x}} = \frac{\partial \Delta \boldsymbol{u}}{\partial^{n+1} \boldsymbol{x}} \tag{3.64}$$

Eq. (3.62) satisfies the principle of material objectivity, which states that a constitutive relation must be independent of any rigid body motions (translation and rotation) (Belitschko et al., 2014; Dunne and Petrinic 2005). In other words, the material response cannot change under the relative motion of a given observer. Finally, as demonstrated by Dunne and Petrinic (2005), all the quantities in Eq. (3.62) are objective. In the present study we employed a zero-graded (constant isotropic elasticity fourth-order tensor) linear constitutive relation between the Jaumann rate of the Cauchy/Kirchhoff stress tensor, which are also objective, and the rate of deformation tensor as follows:

$$\boldsymbol{\sigma}^{\nabla J} = \boldsymbol{C} : \boldsymbol{D} \tag{3.65}$$

$$\boldsymbol{\tau}^{\nabla J} = J\boldsymbol{C} : \boldsymbol{D} \tag{3.66}$$

where the Jaumann rate of the Cauchy stress $\boldsymbol{\sigma}^{\nabla J}$ and the Jaumann rate of the Kirchhoff stress $\boldsymbol{\tau}^{\nabla J}$ are related to the Cauchy stress rate $\boldsymbol{\sigma}$ and to the Kirchhoff stress rate $\boldsymbol{\tau}$ by the following expressions, respectively:

$$\boldsymbol{\sigma}^{\nabla J} = \dot{\boldsymbol{\sigma}} + \boldsymbol{\sigma}\boldsymbol{W} - \boldsymbol{W}\boldsymbol{\sigma} \tag{3.67}$$

$$\boldsymbol{\tau}^{\nabla J} = \dot{\boldsymbol{\tau}} + \boldsymbol{\tau}\boldsymbol{W} - \boldsymbol{W}\boldsymbol{\tau} \tag{3.68}$$

where $\boldsymbol{W}$ is the second-order continuum spin tensor which is given by the skew-symmetric part of the velocity gradient $\boldsymbol{L}$ as follows

$$\boldsymbol{W} = skew(\boldsymbol{L}) = \frac{1}{2}\left(\boldsymbol{L} - \boldsymbol{L}^T\right) \tag{3.69}$$

and the Cauchy stress and the Kirchhoff stress are related as follows

$$\boldsymbol{\tau} = J\boldsymbol{\sigma} \tag{3.70}$$

where J is the Jacobian between the current and reference configurations obtained from de deformation gradient by

$$J = det\,\boldsymbol{F} \tag{3.71}$$

The Eq. (3.67) is crucial to the present implementation since even though the Cauchy stress tensor presents objectivity, its counterpart rate do not possess the required material objectivity (Belitschko et al., 2014; Dunne and Petrinic 2005).

3.4.7 Hypoelastoplastic formulation

Materials which sustain permanent deformations after suffer loading and unloading conditions such as metals, soils and concrete are called plastics. They may be further classified as elastoplastic materials since they usually exhibit elastic behavior until the yield strength is reached, and after this stress limit, plastic strains are evolved. The present section will be focused on the rate-independent plasticity, i.e., the permanent deformation is indifferent to the rate of application of loads. For small elastic strains compared to plastic strains, the modeling of material plasticity can be made in terms of the rate of deformation tensor which can be additively split as (Kim, 2015),

$$\boldsymbol{D} = \boldsymbol{D}^{e} + \boldsymbol{D}^{p} + \boldsymbol{D}^{th} + \boldsymbol{D}^{vp} + \boldsymbol{D}^{c} + \boldsymbol{D}^{tp} \tag{3.72}$$

where $\boldsymbol{D}^{e}$ denotes the elastic part of the rate deformation tensor, $\boldsymbol{D}^{p}$ is the rate-independent part of the rate deformation tensor, $\boldsymbol{D}^{vp}$ is the rate-dependent viscoplastic part of the rate deformation tensor, $\boldsymbol{D}^{th}$ denotes the part of the rate deformation tensor due to thermal expansion, $\boldsymbol{D}^{c}$ is the creep part of the rate deformation tensor, and $\boldsymbol{D}^{tp}$ denotes the transformation plasticity part of the rate deformation tensor. It is worth mentioning that the present work will deal only with the first three components on the right-hand side of Eq. 3.72.

Concerning the Computational Welding Mechanics (CWM) applications, Eq. 3.72 has been used with great success including the in-house codes (Lindgren et al., 1999; Zhu and Chao, 2002; Anca et al., 2011) to the ANSYS a well-established multi-physics commercial software (Sattari-Far and Farahani, 2009; Prasad et al., 2016; Qureshi, 2008), ABAQUS (Deng and Murakawa, 2006), and the SYSWELD a commercial software specifically designated for welding analysis (Ferro et al., 2006; Xu et al., 2012; Velaga et al., 2017).

As the rate of deformation tensor due to the thermal expansion is purely volumetric (Lindgren, 2007), we will treat this term separately at the end of this section, therefore, the following discussion is related to the elastoplastic strains only.

Eq. (3.72) in conjunction with Eqs. (3.65)/(3.66) are the first two components of a general hypoelastoplastic constituve model. To fully describe a hypoelastoplastic constitutive model we need a yield criterion, a plastic flow rule, and a hardening law. It is well-known that plastic flow occurs when the yield stress is reached, and this can be represented by a yield function. Therefore, plastic flow may be represented by

$$f\left(\boldsymbol{\sigma}, \boldsymbol{A}\right) = 0 \tag{3.73}$$

where f is the scalar yield function and $\boldsymbol{A}$ is a set of internal variables. When $f < 0$ one has elastic deformation whereas $f > 0$ is an inadmissible region of the yield surface. The yield function can be expresses in terms of the Von Mises equivalent stress as follows:

$$f\left(\boldsymbol{\sigma},\boldsymbol{A}\right)=\sqrt{\frac{3}{2}}\left\|\boldsymbol{S}\left(\boldsymbol{\sigma}\right)\right\|-\sigma_y\left(\boldsymbol{A}\right) \tag{3.74}$$

where σ_y is the yield stress, $\sigma_{eq}=\sqrt{\frac{3}{2}}\left\|\boldsymbol{S}\left(\boldsymbol{\sigma}\right)\right\|$ is the equivalent stress or von Mises stress, and $\boldsymbol{S}$ is the deviatoric part of the stress tensor, which is given by

$$\boldsymbol{S}=\boldsymbol{\sigma}-p\boldsymbol{I} \tag{3.75}$$

In Eq. (3.75), the invariant Cauchy hydrostatic pressure p is defined as

$$p=\frac{1}{3}tr\ \boldsymbol{\sigma} \tag{3.76}$$

By considering the associative flow rule (Neto et al., 2008), the rate of plastic flow is given by

$$\boldsymbol{D}^p=\dot{\lambda}\frac{\partial f}{\partial\boldsymbol{\sigma}} \tag{3.77}$$

where $\dot{\lambda}$ is a scalar plastic flow. By considering the hardening law from the same function f, we can postulate this rule by a function of a set of internal variables $\dot{\boldsymbol{\alpha}}$

$$\dot{\boldsymbol{\alpha}}=-\dot{\lambda}\frac{\partial f}{\partial\boldsymbol{A}} \tag{3.78}$$

After obtaining the solution of the thermal boundary-valued problem, the transient temperature field is inputted into the mechanical boundary-valued problem via the rate deformation tensor due to thermal expansion, which is given as

$$\boldsymbol{D}^{th} = \beta\left(T\right)\left(T\text{-}T_{ref}\right)\boldsymbol{I} \tag{3.79}$$

where T is the temperature, T_{ref} is the reference temperature, and $\beta\left(T\right)$ is defined as

$$\beta\left(T\right)=\frac{\alpha E}{1\text{-}2v} \tag{3.64}$$

where α is the temperature-dependent linear thermal expansion coefficient.

CHAPTER

4

EbFVM DISCRETIZATION AND NUMERICAL SOLUTION OF THE APPROXIMATED EQUATIONS

4.1 EbFVM discretization of nonlinear heat conduction equation

To obtain the discretization of heat conduction equation, it is necessary to integrate Eq. (3.26) in space and time. The spatial integration is made in a control volume V defined in local coordinates like the one shown in Fig. 3.4. In addition, one may include the term involving boundary conditions in order to include both internal and external fluxes of energy; the result is as follows

$$\int_t \int_V \frac{\partial\left(\rho c_{eff} T\right)}{\partial t} dVdt = \int_t \int_V \nabla \cdot \left(k \nabla T\right) dVdt + \int_t \int_V q dVdt + \int_t \int_S h\left(T_\infty - T\right) dSdt \tag{4.1}$$

where dS is an infinitesimal area. By applying the Gauss's divergence theorem to the first term on the right-hand side of Eq. (4.1), one obtains

$$\int_t\int_V \frac{\partial\left(\rho c_{eff}T\right)}{\partial t}dVdt = \int_t\int_S \left(k\nabla T\right)\vec{n}dSdt + \int_t\int_V qdVdt + \int_t\int_S h\left(T_\infty - T\right)dSdt \tag{4.2}$$

The first term in the left-hand side can be evaluated at node *p* by considering the product of the average value of the integrand by the volume of the control volume. Therefore, the first term in the left-hand side of equation 4.2 becomes

$$\int_t\int_V \frac{\partial\left(\rho c_{eff}T\right)}{\partial t}dVdt = \left[\left(\rho c_{eff}T\right)_p^{n+1} - \left(\rho c_{eff}T\right)_p^{n}\right]\Delta V_p \tag{4.3}$$

where ΔV_p is the volume of the control volume, which can be calculated for hexahedral elements by

$$\Delta V_p = \sum_{i=1}^{n_{scv}} \Delta V_i = \sum_{i=1}^{n_{scv}} det(J)_i \tag{4.4}$$

where n_{scv} denotes the number of sub-control volumes that forms the control volume, and ΔV_i is the volume of each sub-control volume.

The first term in the right-hand side can be evaluated by considering the product of the average value of the integrand by the surface area of the control volume. In order to use a method as unconditionally stable as possible (Lindgren, 2007; Versteeg and Malalasekera, 2007; Maliska, 2004) for any time-step size, we will adopt a fully implicit approach.

$$\int_t\int_S \left(k\nabla T\right)\vec{n}dSdt = \sum_{i=1}^{n_{scv}}\left(\sum_{j=1}^{n_{cs}}\left(k\nabla T\right)_j \cdot \Delta\vec{S}_j\right)_i^{n+1}\Delta t \tag{4.5}$$

where n_{cs} is the number of surfaces of each sub-control volume, Δt is the time step and $\Delta\vec{S}$ denotes the vector area related to each control surface which can be defined as

$$\Delta\vec{S} = \vec{n} \cdot \Delta S \tag{4.6}$$

Finally, inserting Eq. (4.6) into Eq. (4.5), one obtains

$$\int_t \int_S (k\nabla T)\vec{n}dSdt = \left(\sum_{i=1}^{n_{scv}} \sum_{j=1}^{n_{cs}} \sum_{k=1}^{n_v} k_{ij} \nabla N_{ijk} T_{ijk} \cdot \Delta\vec{S}_{ij} \right)^{n+1} \Delta t \tag{4.7}$$

Following the same procedure adopted with transient terms, the source term and the term related to the boundary conditions can be evaluated, respectively, as follows

$$\int_t \int_V qdVdt = q_p^{n+1} \Delta V_p \Delta t \tag{4.8}$$

$$\int_t \int_S h(T_\infty - T)dSdt = h\left(T_\infty - T_p\right)^{n+1} \Delta S_p \Delta t \tag{4.9}$$

Substituting Eqs. 4.3, 4.7, 4.8 and 4.9 into Eq. 4.2, one obtains the discretized form of the thermal energy equation as

$$\left[\left(\rho c_{eff} T\right)_p^{n+1} - \left(\rho c_{eff} T\right)_p^{n} \right] \Delta V_p = \left(\sum_{i=1}^{n_{scv}} \sum_{j=1}^{n_{cs}} \sum_{k=1}^{n_v} k_{ij} \nabla N_{ijk} T_{ijk} \cdot \Delta\vec{S}_{ij} + q_p \Delta V_p + h\left(T_\infty - T_p\right) \Delta S_p \right)^{n+1} \Delta t \tag{4.10}$$

By considering all control volume equations in a given mesh, we have the following system of algebraic nonlinear equations:

$$\boldsymbol{A}^{\boldsymbol{n}+1} \boldsymbol{T}^{\boldsymbol{n}+1} = \boldsymbol{B}^{\boldsymbol{n}} \tag{4.11}$$

where ***A*** is the coefficient matrix, ***T*** is the vector of nodal temperature, and ***B*** is the vector of independent terms. It is important to highlight that the nonlinearities introduced in the system of equations aforementioned is due to temperature-dependent properties, heat source, boundary conditions and so on.

For solving the thermal problem, which is given by Eq. (4.11), one will make use of an incremental procedure. The incremental approach (time marching) starts with a given temperature initial field $\boldsymbol{T_0}$. Then, the system of nonlinear algebraic equation is solved. Finally, the temperature $\boldsymbol{T}$ is assigned to $\boldsymbol{T_0}$ so that temperature field is actualized and the solution continues by further adding new time steps. However, due to the nonlinearities, an iterative procedure needs to be performed during this process.

4.1.1 Iterative solution method for thermal analysis

Eq. 4.11 is a nonlinear system of equations so that an iterative approach is required for linearizing and subsequently solving them at each time step. In order to perform this task, the Newton-Raphson iterative method is used. Equation (4.11) will be rewritten as follows

$$\boldsymbol{A}_{i+1}^{n+1}\boldsymbol{T}_{i+1}^{n+1} - \boldsymbol{B}_{i+1}^{n} = \boldsymbol{R}_{i+1}^{n+1} \tag{4.12}$$

where $\boldsymbol{R}$ is a residue vector and the subscript $\boldsymbol{i}$ is the iteration counter. Iterative corrections to the increment in temperature is made through a predictor $\boldsymbol{T_i}$ for the first iteration and subsequently by an iterative corrector $\delta\boldsymbol{T_i}$. This can be mathematically calculated as

$$\boldsymbol{T}_{i+1}^{n+1} = \boldsymbol{T}_{i}^{n+1} + \delta\boldsymbol{T}_i \tag{4.13}$$

Next, one must find the iterative correction which may obtains $\boldsymbol{R}_{i+1}^{n+1} = \boldsymbol{0}$ in the following iteration. This can be achieved by

$$\boldsymbol{R}_{i+1}^{n+1} \approx \boldsymbol{R}_{i}^{n+1} + \frac{\partial \boldsymbol{R}_{i}^{n+1}}{\partial \boldsymbol{T}}\delta\boldsymbol{T}_i = \boldsymbol{0} \tag{4.14}$$

Eq. 4.14 can be written as

$$-\frac{\partial \boldsymbol{R}_{i}^{n+1}}{\partial \boldsymbol{T}}\delta\boldsymbol{T}_i = \boldsymbol{R}_{i}^{n+1} \tag{4.15}$$

In Eq. 4.15 the derivatives can be calculated as follows

$$-\frac{\partial \boldsymbol{R}_i^{n+1}}{\partial \boldsymbol{T}} = -\left(\frac{\partial \boldsymbol{A}_i^{n+1} \boldsymbol{T}_i^{n+1}}{\partial \boldsymbol{T}} - \frac{\partial \boldsymbol{B}_i^{n}}{\partial \boldsymbol{T}} \right) \approx -\boldsymbol{A}_i^{n+1} \tag{4.16}$$

Therefore, the increment $\delta \boldsymbol{T}_i$ can be finally calculated as

$$\delta \boldsymbol{T}_i = -\left[\boldsymbol{A}_i^{n+1} \right]^{-1} \boldsymbol{R}_i^{n+1} \tag{4.17}$$

The incremental and iterative procedures for solving the heat conduction equation is summarized in Fig. 4.1.

Figure 4.1 – Incremental and iterative procedures for heat conduction analysis.

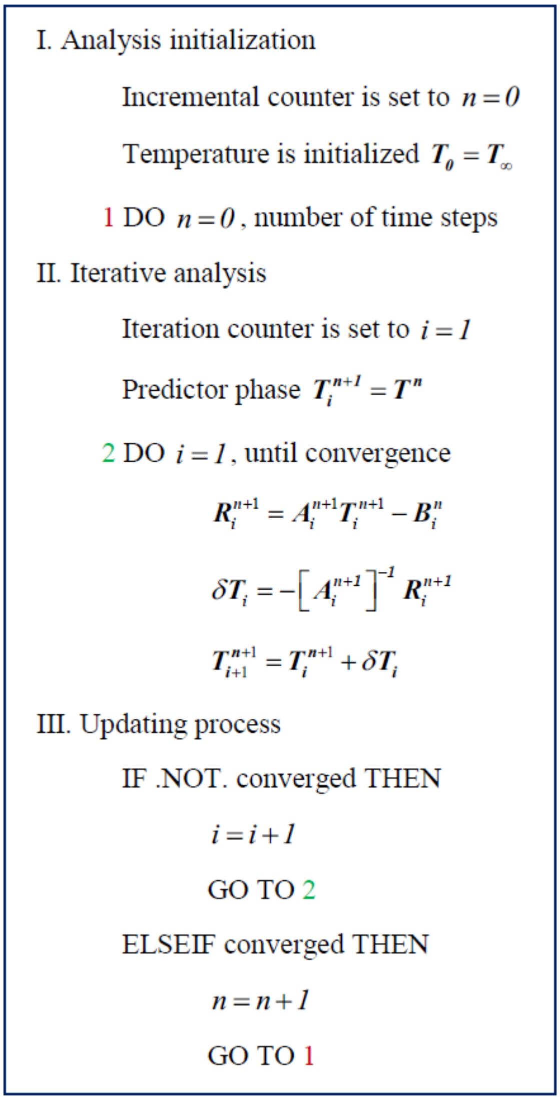

```
I. Analysis initialization
        Incremental counter is set to $n = 0$
        Temperature is initialized $T_0 = T_\infty$
      1 DO $n = 0$, number of time steps
II. Iterative analysis
        Iteration counter is set to $i = 1$
        Predictor phase $T_i^{n+1} = T^n$
      2 DO $i = 1$, until convergence
                $R_i^{n+1} = A_i^{n+1} T_i^{n+1} - B_i^n$
                $\delta T_i = -\left[ A_i^{n+1} \right]^{-1} R_i^{n+1}$
                $T_{i+1}^{n+1} = T_i^{n+1} + \delta T_i$
III. Updating process
        IF .NOT. converged THEN
                $i = i + 1$
                GO TO 2
        ELSEIF converged THEN
                $n = n + 1$
                GO TO 1
```

4.2 EbFVM discretization of nonlinear momentum equations

As a starting point for the purpose of EbFVM numerical implementation the nonlinear momentum equations is written as

$$\boldsymbol{F}_{ext}^{n+1} - \boldsymbol{F}_{int}^{n+1} = \mathbf{0} \tag{4.18}$$

where $\boldsymbol{F}_{ext}^{n+1}$ is a force vector due to external applied loads and $\boldsymbol{F}_{int}^{n+1}$ is a force vector associated with the internal stresses both at time $n+1$. The internal stresses can be written for an arbitrary solid, with a volume V and boundary ∂V in its integral form as

$$\boldsymbol{F}_{int}^{n+1} = \oint_{\partial V} \boldsymbol{\sigma}^{n+1} \cdot \boldsymbol{n} dS = \mathbf{0} \tag{4.19}$$

By substituting Eq. 4.19 into Eq. 4.18 one has

$$\boldsymbol{F}_{ext} - \oint_{\partial V} \boldsymbol{\sigma}^{n+1} \cdot \boldsymbol{n} dS = \mathbf{0} \tag{4.20}$$

By implicitly decomposing the vector of unknown stress components at time $n+1$, which is denoted as $\boldsymbol{\sigma}^{n+1}$ as

$$\boldsymbol{\sigma}^{n+1} = \boldsymbol{\sigma}^{n} + \Delta\boldsymbol{\sigma}^{n+1} \tag{4.21}$$

and substituting Eq. (4.21) into Eq. (4.20), we obtain

$$\oint_{\partial V} \Delta\boldsymbol{\sigma}^{n+1} \cdot \boldsymbol{n} dS = \boldsymbol{F}_{ext}^{n+1} - \oint_{\partial V} \boldsymbol{\sigma}^{n} \cdot \boldsymbol{n} dS \tag{4.22}$$

By rewritten the generalized Hooke’s law (Eq. 3.57) in its counterpart in the rate form and neglecting the contribution due to temperature variation one has

$$\dot{\boldsymbol{\sigma}}^{n+1} = \boldsymbol{C}^{ep,n+1} : \boldsymbol{D}^{e,n+1} \tag{4.23}$$

where $\boldsymbol{C}^{ep}$ is the elastoplastic material tensor. Therefore, by considering the additive decomposition of the rate of deformation tensor expressed in Eq. 3.72, we rearrange Eq. (4.23) as

$$\dot{\boldsymbol{\sigma}}^{n+1} = \boldsymbol{C}^{ep,n+1} : \left(\boldsymbol{D}^{n+1} - \boldsymbol{D}^{p,n+1} - \boldsymbol{D}^{th,n+1} \right) \tag{4.24}$$

By combining Eqs. (4.24), (3.65) and (3.67), one obtains

$$\dot{\boldsymbol{\sigma}}^{n+1} = \boldsymbol{C}^{ep,n+1} : \left(\boldsymbol{D}^{n+1} - \boldsymbol{D}^{p,n+1} - \boldsymbol{D}^{th,n+1} \right) + \boldsymbol{W}^{n+1} \boldsymbol{\sigma}^{n} - \boldsymbol{\sigma}^{n} \boldsymbol{W}^{n+1} \tag{4.25}$$

The left-hand side of Eq. (4.22) can be rewritten considering the incremental form of Eq. (4.25), for each sub-control volume of each individual element (*ne*) of the domain.

$$\sum_{e=1}^{ne} \oint_{\partial V^e} \Delta \boldsymbol{\sigma}^{n+1} \cdot \boldsymbol{n} dS = \sum_{e=1}^{ne} \oint_{\partial V^e} \left[\boldsymbol{C}^{ep,n+1} : \left(\Delta \boldsymbol{D}^{n+1} - \Delta \boldsymbol{D}^{p,n+1} - \Delta \boldsymbol{D}^{th,n+1} \right) + \Delta \boldsymbol{W}^{n+1} \boldsymbol{\sigma}^{n} - \boldsymbol{\sigma}^{n} \Delta \boldsymbol{W}^{n+1} \right] \cdot \boldsymbol{n} dS \tag{4.26}$$

Therefore, substituting Eq. (4.26) into Eq. (4.22), and assuming that a priori we do not have any force associated with inelastic strains, then we have

$$\sum_{e=1}^{ne} \oint_{\partial V^e} \left[\boldsymbol{C}^{ep,n+1} : \Delta \boldsymbol{D}^{n+1} + \Delta \boldsymbol{W}^{n+1} \boldsymbol{\sigma}^{n} - \boldsymbol{\sigma}^{n} \Delta \boldsymbol{W}^{n+1} \right] \cdot \boldsymbol{n} dS = \boldsymbol{F}_{ext}^{n+1} + \boldsymbol{F}_{th}^{n+1} - \boldsymbol{F}_{int}^{n} \tag{4.27}$$

The vector force that takes into account the thermal variation at each vertex is expressed as follows:

$$\boldsymbol{F}_{th}^{n+1} = \sum_{e=1}^{ne} \oint_{\partial V^e} \left[\boldsymbol{C}^{ep,n+1} : \Delta \boldsymbol{D}^{th,n+1} \right] \cdot \boldsymbol{n} dS \tag{4.28}$$

and the internal force vector is

$$\boldsymbol{F}_{int}^{n} = \sum_{e=1}^{ne} \oint_{\partial V^e} \boldsymbol{\sigma}^{n} \cdot \boldsymbol{n} dS \tag{4.29}$$

Eq. 4.27 can be further rearranged as follows

$$\sum_{e=1}^{ne} \oint_{\partial V^e} \left[\boldsymbol{C}^{ep,n+1} \boldsymbol{:} \Delta \boldsymbol{D}^{n+1} \right] \cdot \boldsymbol{n} dS \; + \; \sum_{e=1}^{ne} \oint_{\partial V^e} \left[\Delta \boldsymbol{W}^{n+1} \boldsymbol{\sigma}^{n} - \boldsymbol{\sigma}^{n} \Delta \boldsymbol{W}^{n+1} \right] \cdot \boldsymbol{n} dS \; = \boldsymbol{F}_{ext}^{n+1} + \boldsymbol{F}_{th}^{n+1} - \boldsymbol{F}_{int}^{n} \tag{4.30}$$

In order to get the final form of the matrices which will contribute to the structural stiffness, the terms in the left-hand side are put in index notation. Therefore, using Eqs. 3.14 – 3.16 the following equations are obtained:

$$\begin{aligned} \sum_{e=1}^{ne} \oint_{\partial V^e} \left[\boldsymbol{C}^{ep,n+1} \boldsymbol{:} \Delta \boldsymbol{D}^{n+1} \right] \cdot \boldsymbol{n} dS \; &= \sum_{e=1}^{ne} \oint_{\partial V^e} \left[C_{ijmp}^{ep,n+1} \Delta D_{mp}^{n+1} \right] n_j dS \\ &= \sum_{e=1}^{ne} \oint_{\partial V^e} \left[C_{ijkl}^{ep,n+1} \frac{\partial \Delta u_k^{n+1}}{\partial^{n+1} x_l} \right] n_j dS \\ &= \sum_{e=1}^{ne} \oint_{\partial V^e} \left[C_{ijkl}^{ep,n+1} \sum_{I=1}^{n_v} \frac{\partial N_I}{\partial^{n+1} x_l} \Delta u_{I,k}^{n+1} \right] n_j dS \\ &= \sum_{e=1}^{ne} \oint_{\partial V^e} \left[C_{ijkl}^{ep,n+1} \sum_{I=1}^{n_v} \frac{\partial N_I}{\partial^{n+1} x_l} \right] n_j dS \Delta u_{I,k}^{n+1} \end{aligned} \tag{4.31}$$

$$\begin{aligned} \sum_{e=1}^{ne} \oint_{\partial V^e} \left[\Delta \boldsymbol{W}^{n+1} \boldsymbol{\sigma}^{n} - \boldsymbol{\sigma}^{n} \Delta \boldsymbol{W}^{n+1} \right] \cdot \boldsymbol{n} dS \; &= \sum_{e=1}^{ne} \oint_{\partial V^e} \left[\Delta W_{im}^{n+1} \sigma_{mj}^{n} - \sigma_{im}^{n} \Delta W_{mj}^{n+1} \right] n_j dS \\ &= \sum_{e=1}^{ne} \oint_{\partial V^e} \left[\frac{1}{2} \left(\sigma_{lj}^{n} \delta_{ik} - \sigma_{kj}^{n} \delta_{il} + \sigma_{ik}^{n} \delta_{jl} - \sigma_{il}^{n} \delta_{jk} \right) \frac{\partial \Delta u_k^{n+1}}{\partial^{n+1} x_l} \right] n_j dS \\ &= \sum_{e=1}^{ne} \oint_{\partial V^e} \left[\frac{1}{2} \left(\sigma_{lj}^{n} \delta_{ik} - \sigma_{kj}^{n} \delta_{il} + \sigma_{ik}^{n} \delta_{jl} - \sigma_{il}^{n} \delta_{jk} \right) \sum_{I=1}^{n_v} \frac{\partial N_I}{\partial^{n+1} x_l} \Delta u_{I,k}^{n+1} \right] n_j dS \\ &= \sum_{e=1}^{ne} \oint_{\partial V^e} \left[\frac{1}{2} \left(\sigma_{lj}^{n} \delta_{ik} - \sigma_{kj}^{n} \delta_{il} + \sigma_{ik}^{n} \delta_{jl} - \sigma_{il}^{n} \delta_{jk} \right) \sum_{I=1}^{n_v} \frac{\partial N_I}{\partial^{n+1} x_l} \right] n_j dS \Delta u_{I,k}^{n+1} \end{aligned} \tag{4.32}$$

By retrieving the matrix notation, we can define

$$\boldsymbol{K}_{mat}^{ep,n+1} = K_{ijkl}^{ep,n+1} = \sum_{e=1}^{ne} \oint_{\partial V^e} \left[C_{ijkl}^{ep,n+1} \sum_{I=1}^{n_v} \frac{\partial N_I}{\partial^{n+1} x_l} \right] n_j dS \tag{4.33}$$

$$\boldsymbol{K}_{geo}^{ep,n+1} = K_{ijkl}^{ep,n+1} = \sum_{e=1}^{ne} \oint_{\partial V^e} \left[\frac{1}{2} \left(\sigma_{lj}^{n} \delta_{ik} - \sigma_{kj}^{n} \delta_{il} + \sigma_{ik}^{n} \delta_{jl} - \sigma_{il}^{n} \delta_{jk} \right) \sum_{I=1}^{n_v} \frac{\partial N_I}{\partial^{n+1} x_l} \right] n_j dS \tag{4.34}$$

where $\boldsymbol{K}_{mat}^{ep,n+1}$ is the material stiffness matrix and $\boldsymbol{K}_{geo}^{ep,n+1}$ is the geometrical stiffness matrix, and we can define the total stiffness matrix as

$$\boldsymbol{K}_{tot}^{ep,n+1} = \boldsymbol{K}_{mat}^{ep,n+1} + \boldsymbol{K}_{geo}^{ep,n+1} \tag{4.35}$$

It is important to point out that in the case of small deformation theory the geometrical stiffness matrix is zero since the undeformed and deformed configurations are assumed to be equal. Finally, Eq. 4.30 can be expressed in its matrix form as

$$\boldsymbol{K}_{tot}^{ep,n+1} \boldsymbol{\Delta u}^{n+1} = \boldsymbol{F}_{ext}^{n+1} + \boldsymbol{F}_{th}^{n+1} - \boldsymbol{F}_{int}^{n} \tag{4.36}$$

4.2.1 Iterative solution method for mechanical analysis

When an inelastic load increment takes place, the equilibrium relationship, Eq. 4.36, is nonlinear. The process of linearization starts with the Eq. 4.18 and follows the same procedure developed for thermal equation and for the sake of simplicity only a few steps of the solution procedure for the mechanical analysis will be showed.

Equation 4.18 will be rewritten as follows

$${}^{n+1}_{i}\boldsymbol{F}_{ext} - {}^{n+1}_{i}\boldsymbol{F}_{int} = {}^{n+1}_{i}\boldsymbol{R} \tag{4.37}$$

Iterative corrections to the increment in displacement is made through a predictor ${}_{i}\Delta\boldsymbol{u}$ for the first iteration and subsequently by an iterative corrector ${}_{i}\delta\boldsymbol{u}$. This can be mathematically calculated as

$${}_{i+1}\Delta\boldsymbol{u} = {}_{i}\Delta\boldsymbol{u} + {}_{i}\delta\boldsymbol{u} \tag{4.38}$$

Next, one must find the iterative correction which may obtains $\boldsymbol{R}^{n+1}_{i+1} = \boldsymbol{0}$ in the following iteration. This can be achieved by

$$ {}^{n+1}_{i+1}\boldsymbol{R} \approx {}^{n+1}_{i}\boldsymbol{R} + \frac{\partial {}^{n+1}_{i}\boldsymbol{R}}{\partial \boldsymbol{u}} \, {}_{i}\delta\boldsymbol{u} = \boldsymbol{0} \tag{4.39} $$

Eq. 4.39 can be written as

$$ -\frac{\partial {}^{n+1}_{i}\boldsymbol{R}}{\partial \boldsymbol{u}} \, {}_{i}\delta\boldsymbol{u} = {}^{n+1}_{i}\boldsymbol{R} \tag{4.40} $$

In Eq. 4.40 the derivatives can be calculated as follows

$$ -\frac{\partial {}^{n+1}_{i}\boldsymbol{R}}{\partial \boldsymbol{u}} = -\left(\frac{\partial {}^{n+1}_{i}\boldsymbol{F}_{ext}}{\partial \boldsymbol{u}} - \frac{\partial {}^{n+1}_{i}\boldsymbol{F}_{int}}{\partial \boldsymbol{u}} \right) \tag{4.41} $$

Knowing that the external force vector has no dependency on the displacement, one can reduce the Eq. 4.41 as follows:

$$ -\frac{\partial {}^{n+1}_{i}\boldsymbol{R}}{\partial \boldsymbol{u}} = \frac{\partial {}^{n+1}_{i}\boldsymbol{F}_{int}}{\partial \boldsymbol{u}} = {}^{n+1}_{i}\boldsymbol{K} \tag{4.42} $$

Therefore, the increment ${}_{i}\delta\boldsymbol{u}$ can be finally calculated as

$$ {}_{i}\delta\boldsymbol{u} = \left[{}^{n+1}_{i}\boldsymbol{K} \right]^{-1} {}^{n+1}_{i}\boldsymbol{R} \tag{4.43} $$

The incremental and iterative procedures for solving the nonlinear deformation analysis is summarized in Fig. 4.2.

Figure 4.2 – Incremental and iterative procedures for mechanical analysis.

```
I. Analysis initialization
        Incremental counter is set to $n = 0$
        Force vectors are initialized $\boldsymbol{F}_{ext} = \boldsymbol{0}$ ; $\boldsymbol{F}_{int} = \boldsymbol{0}$
      1 DO $n = 0$, number of load/time steps
II. Iterative analysis
        Iteration counter is set to $i = 1$
        Predictor phase ${}^{n+1}_{i}\boldsymbol{F}_{ext} = {}^{n}_{i}\boldsymbol{F}_{ext}$ ; ${}^{n+1}_{i}\boldsymbol{F}_{int} = {}^{n}_{i}\boldsymbol{F}_{int}$
      2 DO $i = 1$, until convergence
            ${}^{n+1}_{i}\boldsymbol{R} = {}^{n+1}_{i}\boldsymbol{F}_{ext} - {}^{n+1}_{i}\boldsymbol{F}_{int}$
            ${}_{i}\delta\boldsymbol{u} = \left[{}^{n+1}_{i}\boldsymbol{K}\right]^{-1} {}^{n+1}_{i}\boldsymbol{R}$
            ${}_{i+1}\Delta\boldsymbol{u} = {}_{i}\Delta\boldsymbol{u} + {}_{i}\delta\boldsymbol{u}$
III. Update variables ( $\boldsymbol{F}, \boldsymbol{D}, \boldsymbol{\sigma}$ )
        IF .NOT. converged THEN
            $i = i + 1$
            GO TO 2
        ELSEIF converged THEN
            $n = n + 1$
            GO TO 1
```

In order to take into account large rotational increments, an algorithm proposed by Hughes and Winget (1980) was used to update the stress at the previous load step to the rotation-free configuration by

$$\bar{\boldsymbol{\sigma}}^{n} = \boldsymbol{Q}\boldsymbol{\sigma}^{n}\boldsymbol{Q}^{T} \tag{4.44}$$

where $\boldsymbol{Q}$ is the incremental rotation tensor, which is defined by

$$\boldsymbol{Q} = \left(\boldsymbol{I} - \frac{1}{2}\boldsymbol{W}\right)^{-1}\left(\boldsymbol{I} + \frac{1}{2}\boldsymbol{W}\right) \tag{4.45}$$

The spin tensor ***W*** is defined at the midpoint configuration as

$$\boldsymbol{W} = \frac{1}{2}\left(\frac{\partial \Delta \boldsymbol{u}}{\partial^{n+\frac{1}{2}}\boldsymbol{x}} - \frac{\partial \Delta \boldsymbol{u}}{\partial^{n+\frac{1}{2}}\boldsymbol{x}}^{\boldsymbol{T}} \right) \tag{4.46}$$

Finally, the displacement gradient at the midpoint configuration is calculated as

$$\frac{\partial \Delta \boldsymbol{u}}{\partial^{n+\frac{1}{2}}\boldsymbol{x}} = \boldsymbol{L}\left(\boldsymbol{I} - \frac{1}{2}\boldsymbol{L} \right)^{-1} \tag{4.47}$$

Thus, by taking the rotated stress from Eq. 4.44 one may update the Cauchy stress as follows

$$\boldsymbol{\sigma}^{n+1} = \bar{\boldsymbol{\sigma}}^{n} + \Delta\boldsymbol{\sigma}^{n+1} \tag{4.48}$$

4.2.2 Implicit numerical integration of the return mapping

For the treatment of the nonlinear equations involved in this theory is assumed an implicit integration scheme in time, which is linearized via the Newton–Raphson method. The reasons behind this choice lie on the stability and quadratic convergence rate near the root. Therefore, in case of plasticity loads, the aforementioned numerical approach is used to correct the stress state, at the integration point, in terms of the internal parameters when required. In the return mapping procedure, the stress field calculated by Eq. (4.48) is adopted as the candidate stress tensor

$$\sigma^{n+1} = \sigma^{c} \tag{4.49}$$

Once the material yields, the condition of a plastic load is verified and the stress state must be corrected with the insertion of the inelastic increment of the rate of deformation tensor

$$\Delta D^{p,n+1} = \Delta\bar{\varepsilon}^{n+1}\sqrt{\frac{3}{2}}\frac{S}{\|S\|} \tag{4.50}$$

where $\bar{\varepsilon}$ is a multiplier parameter, and finally, the stress-strain relation can be written with inclusion of the inelastic strain as

$$\sigma^{n+1} = \sigma^{c} - C^{e}\Delta\bar{\varepsilon}^{n+1}\sqrt{\frac{3}{2}}\frac{S\left(\sigma^{n+1}\right)}{\left\|S\left(\sigma^{n+1}\right)\right\|} \tag{4.51}$$

In order to differentiate the return mapping equations from the equilibrium procedure, the iterative superscript *j* is adopted instead of *n*.

Therefore, rewriting Eqs. (4.51) and (3.74) in the residual form, we obtain

$$R_{\sigma}^{j} = \left[C^{e}\right]^{-1}\left(\sigma^{j} - \sigma^{c}\right) + \Delta\bar{\varepsilon}^{j}\sqrt{\frac{3}{2}}\frac{S\left(\sigma^{j}\right)}{\left\|S\left(\sigma^{j}\right)\right\|} \tag{4.52}$$

$$R_{\bar{\varepsilon}}^{j} = \sigma_{eq} - \sigma_{y}\left(\Delta\bar{\varepsilon}^{j}\right) \tag{4.53}$$

Applying the Newton-Raphson method to Eqs. (4.52) and (4.53), we obtain

$$\begin{bmatrix} \partial\sigma^{j+1} \\ \partial\bar{\varepsilon}^{j+1} \end{bmatrix} = -\left[J\right]^{-1}\begin{bmatrix} R_{\sigma}^{j} \\ R_{\bar{\varepsilon}}^{j} \end{bmatrix} \tag{4.54}$$

where *J* is the Jacobian matrix, which is given by

$$J = \begin{bmatrix} \dfrac{\partial R_{\sigma}}{\partial\sigma} & \dfrac{\partial R_{\sigma}}{\partial\bar{\varepsilon}} \\ \dfrac{\partial R_{\bar{\varepsilon}}}{\partial\sigma} & \dfrac{\partial R_{\bar{\varepsilon}}}{\partial\bar{\varepsilon}} \end{bmatrix} \tag{4.55}$$

The new stress state and inelastic internal variable are updated as follows

$$\sigma^{j+1} = \sigma^{j} + \delta\sigma^{j+1} \tag{4.56}$$

$$\bar{\varepsilon}^{j+1} = \bar{\varepsilon}^{j} + \delta\bar{\varepsilon}^{j+1} \tag{4.57}$$

These values are used to update the incremental terms

$$\Delta\sigma^{j+1} = \sigma^{j+1} - \sigma^{j} \tag{4.58}$$

$$\Delta\bar{\varepsilon}^{j+1} = \bar{\varepsilon}^{j+1} - \bar{\varepsilon}^{j} \tag{4.59}$$

The above parameters are used to update the residue vectors R_{σ}^{j+1} and $R_{\bar{\varepsilon}}^{j+1}$. When the convergence criterion is reached, the tangent modulus $C^{ep,n+1} = \left.\frac{\partial\sigma}{\partial D}\right|^{n+1}$ is evaluated using the following expression:

$$\begin{bmatrix} \partial\sigma^{j+1} \\ \partial\bar{\varepsilon}^{j+1} \end{bmatrix} = \begin{bmatrix} C_{11} & C_{12} \\ C_{21} & C_{22} \end{bmatrix} \begin{bmatrix} \partial D^{j+1} \\ 0 \end{bmatrix} \tag{80}$$

where $\left.\frac{\partial\sigma}{\partial D}\right|^{n+1} = C_{11}$. This result leads to $C^{ep,n+1} = C_{11}$, which is the new tangent matrix at the integration point.

For more details of the whole implicit numerical integration procedure see Pimenta (2019).

4.3 Numerical approach

The general behavior of a given workpiece being welded is strongly affected by the coupling among heat transfer, microstructure evolution, and thermal stresses (Goldak and Akhlaghi, 2005). In addition, we may add the fluid flow into the weld pool as well as the fluid flow into a given pipeline as in the in-service welding case. However, concerning the aforementioned couplings, the present work only focus on the effects of transient temperature fields on the thermal stresses and mechanical deformations. The fluid flow into the pipeline will be presented into the numerical model by empirical correlations relating the heat transfer coefficient at internal wall boundaries and the fluid flow of the molten pool will be inserted by the modification of physical properties at this region. Furthermore, the solution procedure is based upon a decoupled approach, where the solution of the thermal and mechanical analysis is made sequentially. Firstly, we have a transient thermal analysis in order to obtain nodal the temperature distribution and this is followed by a non-linear structural analysis where the stress behavior is evaluated at the integration points.

CHAPTER

5

VERIFICATION AND VALIDATION TEST CASES

The process of transforming a real-world phenomenon into a physical model, which will be capable of reproduces all its important ingredients, is often composed by a great amount of complex aspects. Therefore, in order to represent these phenomena as accurate as possible, is it mandatory, for any physical model, to be exhaustively tested so that it reaches reliable results. When one performs any numerical analysis, different types of errors may appear, erroneous applied boundary conditions as an example, for that reason the process of verification and validation of the numerical model must be doing as the first step of the given analysis. Furthermore, Versteeg and Malalasekera (2007) pointed out that by doing verification and validation one may quantify errors and uncertainty, respectively. In addition, it is important to mention that those aforementioned aspects are inherently related to any numerical modeling.

According to Lindgren (2007) verification is the process that determines if the equations which describe the physical model are solved correctly; this can be verified by comparing the numerical solutions with benchmark solutions, i.e. analytical solutions, and highly resolved numerical solutions, whereas validation is a process that checks if the numerical model reproduces the real world behavior. Therefore, the validation can be performed by comparing the numerical results with high-quality experimental results.

Thus, with the aim to both obtain numerical verification and validation of the MPE_EbFVM (multi-physics environment) developed code, we have performed some verification and validation test cases for thermal, mechanical and thermo-mechanical problems. Furthermore, additional verification and validation test cases for the MPE_EbFVM were performed in the works by Pimenta and Marcondes (2019), and Pimenta (2019).

Before we start, it is important to mention some considerations that were adopted for all simulation test cases. They are stated as follows:

- Independence tests for grid, timestep (transient thermal analysis), and loadstep (non-linear mechanical analysis).
- The meshes adopted were either structured or unstructured depend on the given problem; this is possible due to the flexibility that EbFVM approach has to handle both types of grids.
- Wherever there was a symmetry in the geometry, the simulated domain was reduced to one-half, one-quarter or one-eighth according to the specific problem.
- The majority of test cases were performed with a mesh composed of hexahedral elements, except for few cases, where tetrahedrons and prisms elements were employed.
- Localized grid refinement was made near critical regions with the aim to provide a better resolution for the property being analyzed, and the rest of the given domain was set with a coarse mesh so as the computational resources were saved.
- Based on the comparison between the results obtained by the present study and analytical, numerical or experimental results from literature, the relative error was defined as follows:

$$\varepsilon = \frac{\left| X_{EbFVM} - X_{comp} \right|}{X_{comp}} \tag{5.1}$$

where X_{EbFVM} is a given result from the present study and X_{comp} is the result from the literature study.

5.1 Thermal analysis

Since the present work is an uncoupled sequentially thermo-mechanical analysis, the process of verification and validation of the numerical model can be performed apart for both thermal and mechanical problems. Hence, this section presents verification and validation test cases for thermal analysis only.

5.1.1 2D steady-state heat conduction

This section presents a simple benchmark for the MPE_EbFVM. The problem consists of a 2D steady-state heat conduction modeled by a 3D square thin plate. In addition, since neither phase change nor heat generation are used, Eq. (3.22) has been reduced to the well-known Laplace's equation, which is given by

$$\nabla^2 T = 0 \tag{5.2}$$

The geometry as well as the boundary conditions are represented in Fig. 5.1. The length and width are equal to one, and the 3D plate was made with a small thickness (*0.01W*), where W is the width of the plate. Dirichlet BC was prescribed in the *x*-*y* plane, and symmetry conditions (Neumann BC) was imposed in the *z*-normal direction.

Figure 5.1 – Geometry and boundary conditions adopted in the 2D steady-state heat conduction analysis.

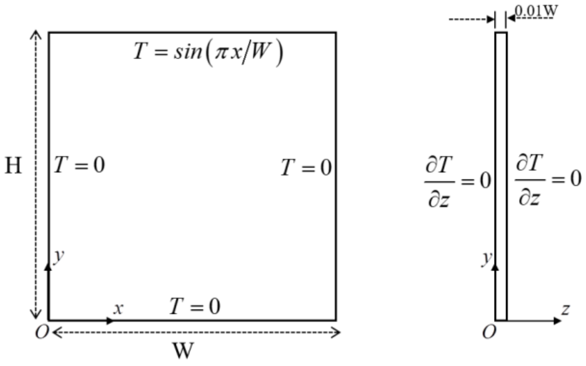

The analytical solution for Eq. (3.37) with the particular set of boundary conditions showed in Fig. 5.1 is given by

$$T = \frac{sinh\left(\pi y/W\right)}{sinh\left(\pi H/W\right)} sin\left(\pi x/W\right) \tag{5.3}$$

For the present simulation, it was adopted a structured hexahedral-based mesh composed by 882 nodes, and 400 elements. The results obtained with the MPE_EbFVM was compared against the analytical ones. They are presented in Fig. 5.2. The green marks in the numerical results represent a temperature profile, *T(x, y=0.5)*, and the red ones represent the numerical results for the temperature profile *T(x=0.5, y)*.

Figure 5.2 – Comparison of analytical and numerical results for a 2D heat conduction problem.

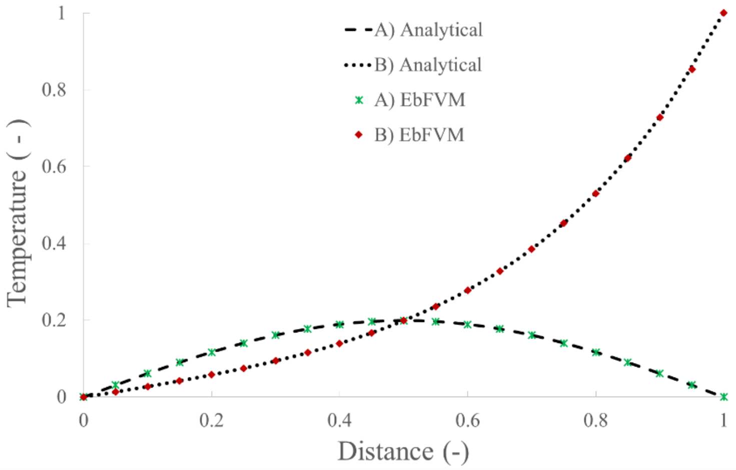

From the results, one can see excellent agreement between numerical and analytical results. In addition, in spite of the simple character of this specific problem, one may conclude that this test case is a fair first step to verify our designed numerical code.

5.1.2 3D moving heat source in a semi-infinite domain

This verification test case was performed by comparing the present work with analytical solutions by Fachinotti et al. (2011). In the latter work they calculated induced thermal field by a moving double-ellipsoidal heat source in a semi-infinite body for welding processes. The present verification was made by comparing temperature variation with time in a specified point (thermal cycles) as well as temperature profiles in a specified path. The present test case has some simplifications (as frequently found in most analytical solutions in the welding area), viz., adiabatic boundary conditions, autogenous process, and no latent heat effects. Fig. 5.3 shows both geometry (*length = 200 mm, width = 200 mm, height = 100 mm*) and the unstructured mesh used in the EbFVM analysis.

Figure 5.3 – Geometry and unstructured mesh adopted in the EbFVM analysis.

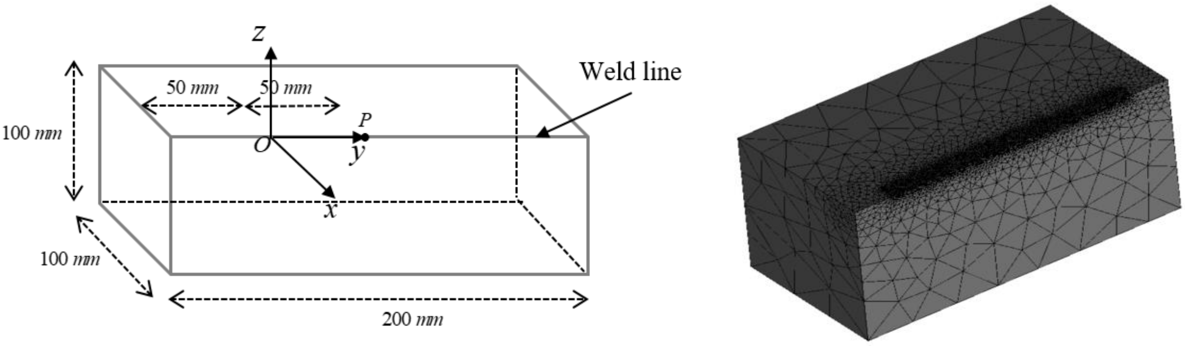

Three different cases were analyzed (A, B, C), where we varied the size and the amount of the heat deposited in the front and the rear of the semi-ellipsoid. Table 5.1 shows the physical and geometrical welding parameters used in this analysis.

Table 5.1. Physical and geometrical welding parameters.

		Case	
Parameter	A	B	C
c_f, c_r	6 *mm*, 24 *mm*	15 *mm*, 15 *mm*	24 *mm*, 6 *mm*
f_f, f_r	0.4, 1.6	1.0, 1.0	1.6, 0.4
b, a		2 mm, 10 *mm*	
k		29.0 *W/m.K*	
c		600 *J/kg.K*	
ρ		7820 kg/m^3	
Q		5083 *W*	
v		5 *mm/s*	
T_0		20°C	

Source: Fachinotti et al. (2011).

Considering geometry and the aforementioned parameters, the welding torch starts moving at point *O* (0,0,0) when time *t=0 s* and moves along *y*-axis with a constant speed. To discretize the domain, an unstructured mesh composed of 10,334 tetrahedral elements and 19,373 nodes was used. In addition, a time-step equal to 0.05 *s* was adopted and kept constant for the whole simulation.

Figs. 5.4 and 5.5 depict the thermal cycles at point *P* (0,50,0) and temperature profile along the weld line at time *t=10 s*, respectively.

Figure 5.4 – Thermal cycles for different geometric parameters of the heat source for both analytical and EbFVM analysis.

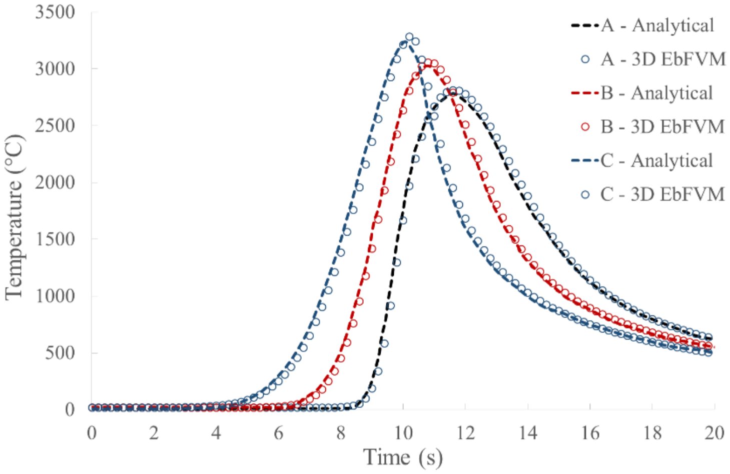

Figure 5.5 – Temperature profiles for different geometric parameters of the heat source for both analytical and EbFVM analysis.

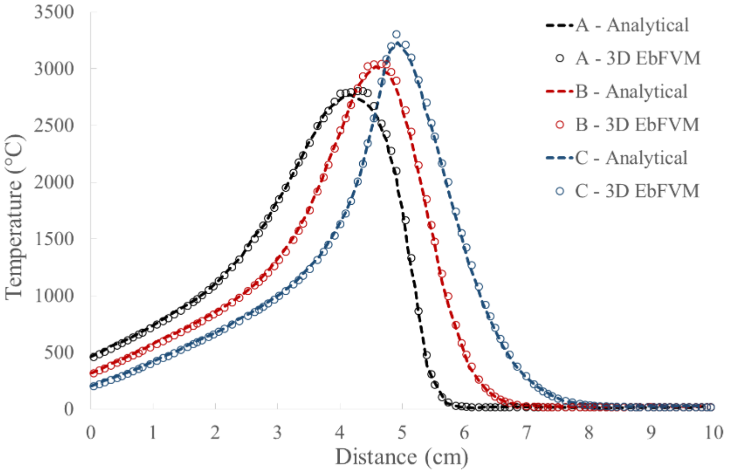

The obtained results from the present work, for all double-ellipsoidal heat source configurations, showed an excellent agreement with the analytical solution by fitting it with high accuracy. The maximum relative error for both the thermal cycle and the thermal profile curves were observed in the case C, at the peak temperature, where it assumes a value of 1.33%, and 2.35%, respectively.

Despite the analysis has been made with temperature-independent properties, which makes the analysis easier, the locations where both thermal cycles and temperature profiles were compared with the analytical solutions are regions of high gradients, and the present numerical approach was able to capture all these details with high accuracy. Therefore, since the results showed high accuracy when compared against analytical solutions, the present model is able to properly represent a welding process subjected to a volumetric Gaussian heat source.

5.1.3 3D and 2D heat source models

We now validate our 3D MPE_EbFVM code with various types of moving heat sources using a thick plate with *length = 300 mm, width = 200 mm, and height = 100 mm*. The tested heat sources are as follows: disc-shaped, double-ellipse, semi-ellipsoidal, and double-ellipsoidal heat sources.

The results are compared against experimental results by Christensen et al. (1965). Fig. 6.6 shows both the geometry along with the double-ellipsoidal heat source model (out of scale) and the mesh adopted in the present validation test case. All the boundaries except the top surface were kept insulated. At the top surface a combination of convection and radiation losses were set by applying Eq. (3.32).

Figure 5.6 – Geometry along with double-ellipsoidal heat source (a) and mesh for the validation test case.

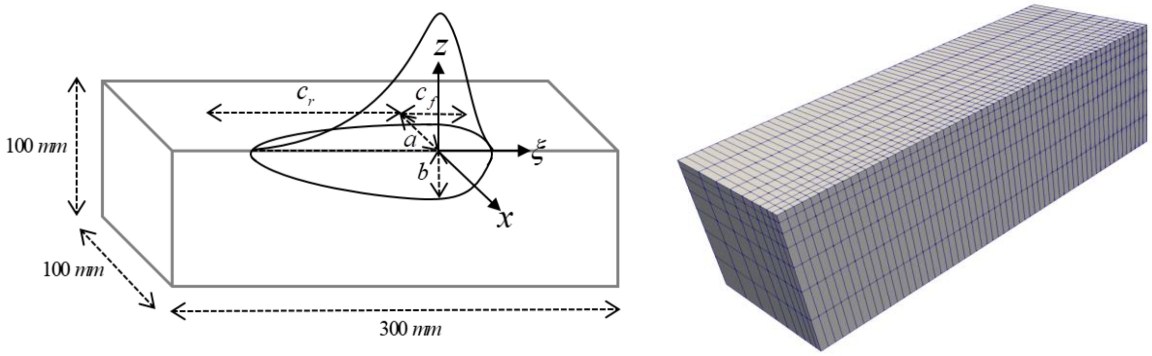

For this test case, a mesh composed of regular hexagonal elements was used. The mesh is composed by 4,880 nodes and 3,780 elements. As can be seen in Fig. 5.6, the adopted mesh is very coarse even in the weld line, this is because the heat source dimensions are large in comparison with the whole domain. However, a refinement was performed through the welding torch path. It is important to point out that these kinds of elements can capture high gradients easily, which is often required in welding numerical analysis. High gradients occur in the molten pool (fusion zone) and HAZ (Heat-affected zone) regions due to the location of the high intensity arc welding, different from the remainder domain, which is often at ambient temperature.

The geometrical and welding parameters are shown in Table 5.2. Thermo-physical properties for a low carbon structural steel (0.23 %C) are given in Table 5.3. The welding process simulated is SAW.

Table 5.2. Welding and geometrical parameters.

Parameter	Value
Current	1170 *A*
Voltage	32.9 *V*
Efficiency	0.95
Speed	5 *mm/s*
b, a	20 mm, 20 *mm*
c_f, c_r	15 mm, 30 *mm*
f_f, f_r	0.6, 1.4

Source: Goldak et al. (1984).

Table 5.3. Thermophysical properties for thermal analysis.

Parameter	Value
Thermal conductivity (solid)	34.0 *W/m.K*
Thermal conductivity (liquid)	68.0 *W/m.K*
Specific heat	680.0 *J/kg.K*
Density	7200.0 kg/m^3
Latent heat	291660.0 *J/kg*
Solidus temperature	1763 *K*
Liquidus temperature	1774 *K*

Source: Anca et al. (2011).

Fig. 5.7 presents the temperature distribution obtained with four heat sources models in a transverse section to the welding direction 11.5 *s* after the arc welding has passed by that section. The heat sources are disc-shaped, double-ellipse, semi-ellipsoidal, and double-ellipsoidal heat sources.

Figure 5.7 – Comparison of EbFVM numerical and Experimental temperature distributions along with different heat source models.

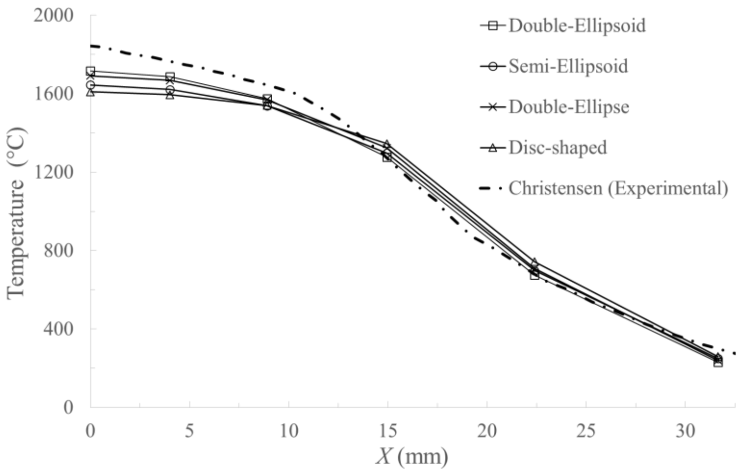

The results for all the heat source models showed an acceptable agreement with the experimental results by Christensen et al. (1965). By comparing the accuracy amongst the heat source models, all of them showed similar results far from the weld pool. Discrepancies were showed near the weld center line, where maximum relative error were found for all heat sources. They were 6.9%, 8.25%, 10.8%, and 12.7% for the double-ellipsoid, double-ellipse, semi-ellipsoid, and disc-shaped heat source, respectively. In addition, as it can be seen in Fig. 5.7, the double-ellipsoidal heat source model presented a better fit with the experimental results, which also agree with previous literature works (Goldak et al., 1984; Hashemzadeh et al., 2013). Therefore, for this specific test case, the Goldak's model seems to be a better choice for characterizing the transient welding process.

From Fig. 5.7, we can observe that, in average, all heat source models predicted similar temperature profile. This observation is in accordance with the results obtained by Lindgren (2007) and Flint et al. (2018). However, as we stated before, if one wants to obtain an accurate temperature profile, the double-ellipsoid is the best heat source model.

Finally, it is worthwhile mentioning that despite of all heat source models were able to predict the temperate profile, none of them were able to capture the temperature profile around the heat source ($\xi = 0$). Therefore, further investigations need to be performed in order to understand such behavior.

5.1.4 Single-pass butt-welded pipe

The present verification test case was performed in a single-pass butt-welded pipe. The present work is compared with the FEM analysis by Karlsson and Josefson (1990). Both EbFVM and FEM models applied full 3D models in a girth welding simulation. The geometry and a portion of the mesh (near the weld line) are shown in Fig. 5.8. The outer pipe diameter, wall thickness, and total length of the pipe are *114.3 mm, 8.0 mm, and 400 mm*, respectively. Filler material is deposited in a *5.5 mm* deep V-groove. The welding process simulated is MIG. At all boundaries, except the symmetry surface (kept insulated), a combination of convection and radiation losses were set by applying Eq. (3.32).

Figure 5.8 – Single-pass butt-welded pipe. Joint configuration and mesh near the weld line.

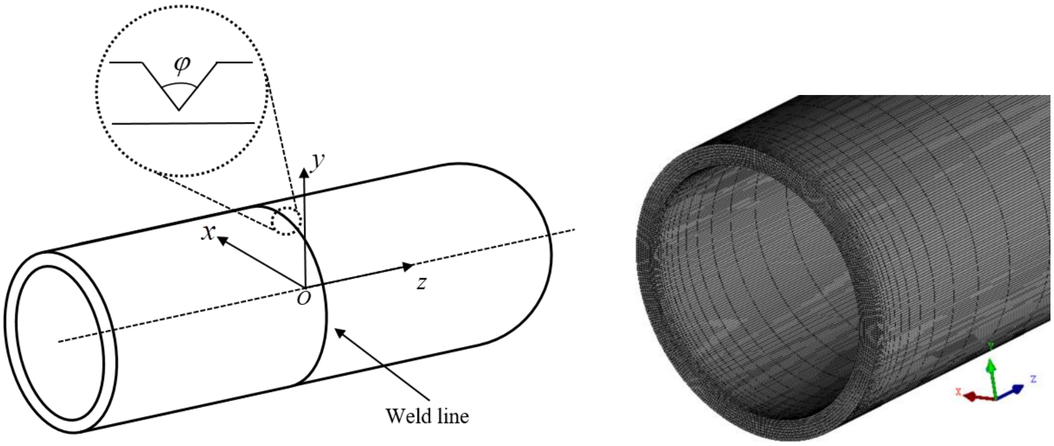

For discretize the domain, an unstructured mesh composed by 1,800 prisms, 25,920 hexahedron, and 36,000 nodes was used. In addition, a time-step equal to 0.05 *s* was adopted and kept constant in the whole simulation. For this simulation, a semi-ellipsoidal heat source model was adopted.

The material employed in the simulation is C-Mn (Carbon-Manganese) steel and its temperature-dependent properties are shown in Fig. 5.9. In Fig. 5.9, TC stands for thermal conductivity, HTC is the heat transfer coefficient, SH-BM is the specific heat at the base metal, and SH-HAZ stands for the specific heat at the heat-affected-zone. HAZ was considered for temperatures ranging from 900 °C to the melting point isotherm.

Figure 5.9 – C-Mn temperature-dependent properties.

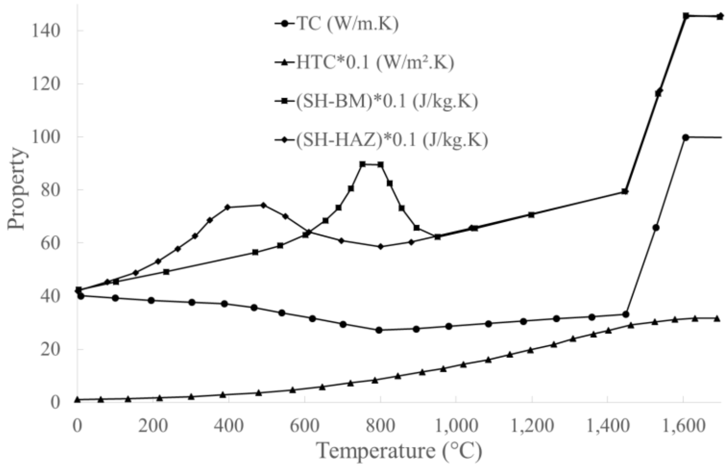

Source: Karlsson and Josefson (1990).

Considering the aforementioned geometry and parameters, the welding torch starts to move at time *t=0 s* at $\theta = 0°$ (refer to Fig. 3.8) and moves around the whole pipe with a constant speed. Welding and geometrical parameters are illustrated in Table 5.4.

Table 5.4. Welding and geometrical parameters.

Parameter	Value
Power	3780 *W*
T_0	20 °C
Efficiency	0.9
Speed	6 *mm/s*
b, a	6 mm, 3.5 *mm*
c	5 mm

Source: Karlsson and Josefson (1990).

Fig. 5.10 shows the temperature profile for a single-pass butt-welded pipe at the outer pipe surface and $\theta = 150°$. We also present the numerical results obtained by Karlsson and Josefson (1990) using the FE method.

Figure 5.10 – Outer surface temperature profile after heat source front has passed at various moments.

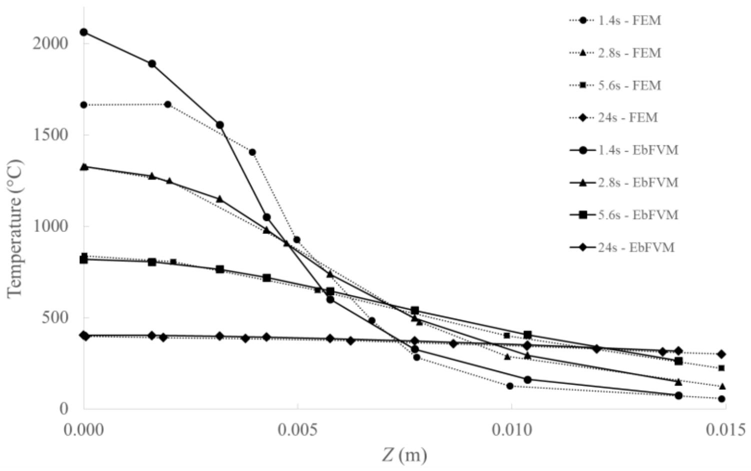

From Fig. 5.10, one can see excellent agreement when comparing both studies at times *t = 2.8 s, t = 5.6 s, and t = 24 s*. However, for the time *t = 1.4 s* EbFVM significantly diverges from the FEM at the weld line. The relative error at the latter time reaches a value of 23.9% at the weld line and decreases near to zero at regions far away from the weld line. Hence, further investigations need to be performed in order to understand such deviation.

Finally, considering that both verification and validation test cases for thermal analysis presented good agreements in most of the cases, and that in cases where some discrepancy between the comparisons emerged can be attributed to some assumptions and the inherently deviation of the numerical studies to analytical, experimental, and other tools, the present MPE_EbFVM code can be employed for analysis of welding process in general, including in-service welding.

5.2 Mechanical analysis

Since the present work is an uncoupled sequentially thermo-mechanical analysis, the process of verification and validation of the numerical model can be performed apart for both thermal and mechanical problem. Hence, this section presents one verification test case for mechanical analysis only.

5.2.1 Internally pressurized cylinder

This section presents a verification test case involving just mechanical effects provided by an internal pressure applied in a 3D long cylinder. The geometry of the problem, the boundary conditions, and the 3D element mesh are represented in Fig. 5.11. Material properties as well as geometrical parameters are illustrated in Table 5.5. For discretize the domain, a structured mesh composed by 100 hexahedron, and 242 nodes was used. Also, due to symmetry only one-quarter of the geometry was used. Perpendicular constraints were set at symmetry planes (Dirichlet boundary conditions). The analysis was carried out under perfectly-plastic conditions and assuming plane strain conditions by making use of only one element in the normal *z*-direction and making normal constraints in this direction as well.

Figure 5.11 – Infinite long internally pressurized cylinder.
Geometry, boundary conditions and 3D element mesh.

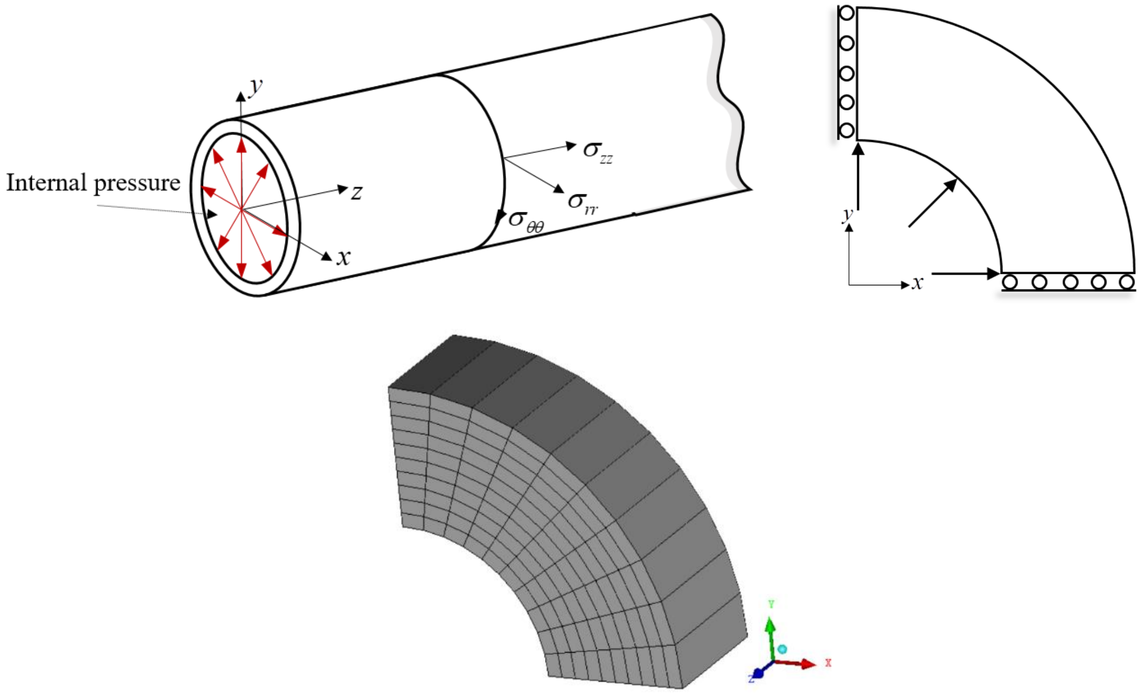

Table 5.5. Material properties and geometrical parameters for mechanical analysis.

Parameter	Value
Young's modulus	210.0 *GPa*
Poisson's ratio	0.3
Uniaxial yield stress	0.24 *GPa*
Internal radius	0.1 *m*
External radius	0.2 *m*

Source: Neto et al. (2008).

The results were compared against the analytical solutions by Hill (1950). Fig. 5.12 shows the applied internal pressure versus the radial displacement at the cylinder's outer surface. From the results, one can see excellent agreement between numerical and analytical solutions.

Figure 5.12 – Internal pressure vs radial displacement.

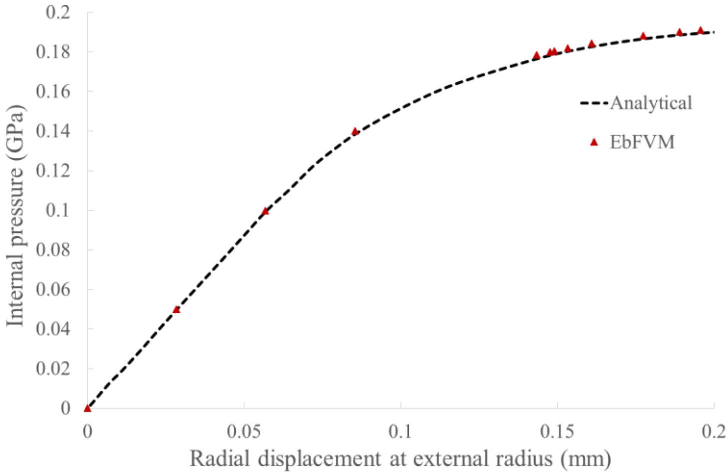

Fig. 5.12 and Fig. 5.13 shows the hoop and radial stress versus radial coordinate, respectively. Both plots are obtained for an applied internal pressure equal to 0.18 GPa.

Figure 5.13 – Hoop stress vs radial coordinate.

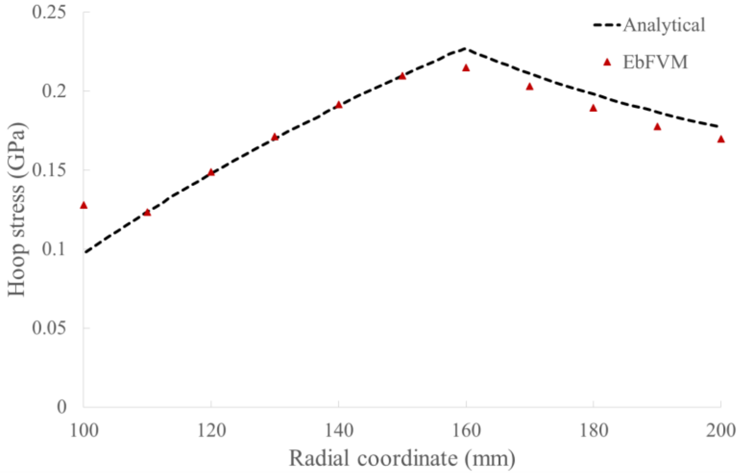

Figure 5.14 – Radial stress vs radial coordinate.

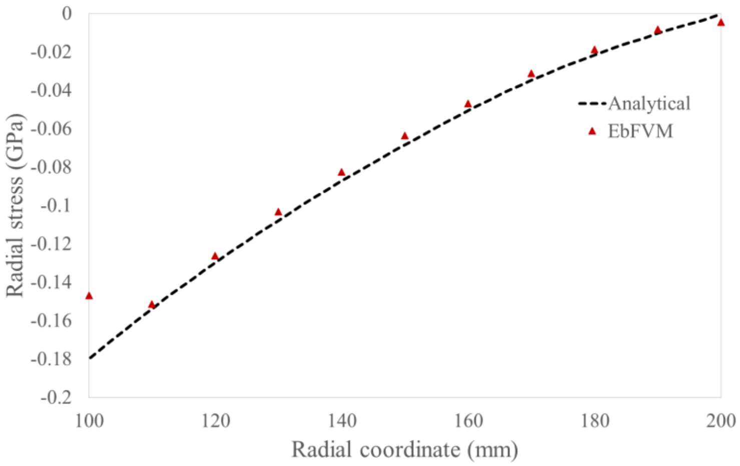

The numerical results were in good agreement with the analytical solution. Attention needs to be paid at the inner cylinder’s surface where the results did not fit well. The relative error for the hoop stress distribution reaches a maximum value of 30% at the inner surface while the relative error for the radial stress reaches a maximum value of 18% also at the inner surface. Hence, further investigations need to be performed in order to understand such deviation. Finally, it is important to mention that the abrupt change in the slope of the hoop stress showed in Fig. 5.13 marks the transition of an elastic to a plastic region.

5.3 Thermomechanical analysis

Since the present work is an uncoupled sequentially thermo-mechanical analysis, the process of verification and validation of the numerical model can be performed apart for both thermal and mechanical problem. Hence, this section presents verification and validation test cases for thermomechanical analysis.

5.3.1 Infinite long plate with temperature-dependent shear modulus

The present verification test case was performed in an infinite long plate subjected to a thermoelastic loading. The present work is compared with the analytical solution by Sladek et al. (1990). The geometry of the problem, the boundary conditions, and the 3D element mesh are shown in Fig. 5.15. To discretize the domain, a structured mesh composed by 800 hexahedrons, and 1722 nodes was used. Assumption of plane strain conditions was made by making use of only one element in the normal *z*-direction and making normal constraints in this direction as well.

Figure 5.15 – Infinite long plate. Geometry, boundary conditions and 3D element mesh.

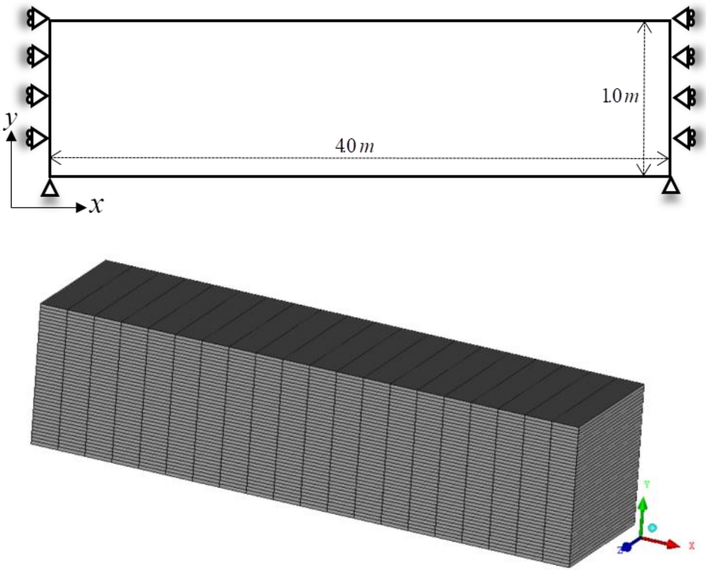

The infinite long plate was subjected to a linear temperature distribution along the *y*-direction (ranging from 5°C to 100°C) and to a linear temperature-dependent shear modulus. The reference temperature was equal to 0°C. The material properties as well as the temperature profile are depicted in Table 5.6.

Table 5.6. Material properties and temperature profile for the thermomechanical analysis.

Parameter	Value
Temperature	T(y) = 95y+5
Shear modulus	S(T) = -15.23T+7.95E+4
Poisson’s ratio	0.3
Thermal expansion coefficient	1.25E-5 °C^{-1}

Source: Sladek et al. (1990).

Fig. 5.16 shows vertical displacement and Fig. 5.17 shows the normal stress along the left wall. As we can see, excellent agreement was achieved by comparing the numerical and analytical results.

Figure 5.16 – Vertical displacement vs Y-coordinate.

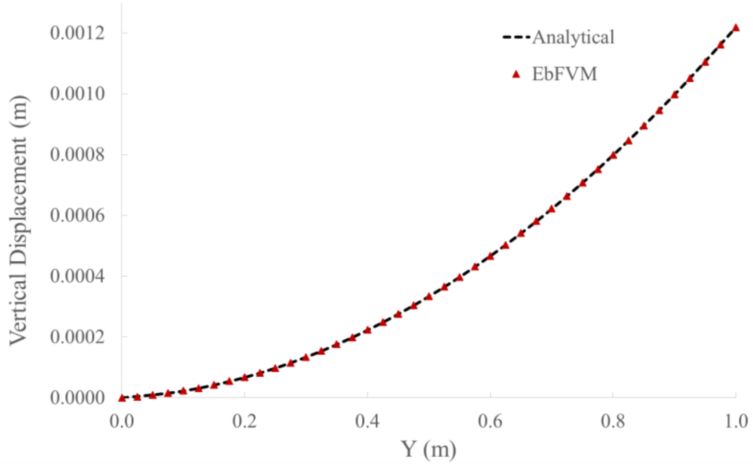

Figure 5.17 – X-normal stress vs Y-coordinate.

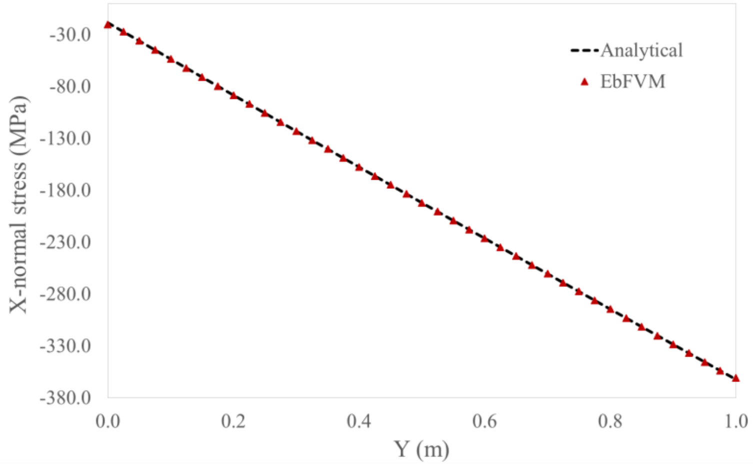

5.3.2 Thermal hollow sphere subjected to mechanical loading

The present verification test case was performed in a hollow sphere subjected to thermal and mechanical loadings. The present work is compared with the analytical solution by Timoshenko and Goodier (1970). The geometry of the problem, the loadings, the boundary conditions, and the 3D element mesh are represented in Fig. 5.18. To discretize the domain, an unstructured mesh composed by 100065 tetrahedrons, and 18413 nodes was used. Also, due to symmetry only one-eighth of the geometry was used, and in addition, perpendicular constraints were set at symmetry planes (Dirichlet boundary conditions). The temperature and pressure at the inner radius, R_1 = 0.01 m, were constant and equal to 6 °C and 5 GPa (red arrows), respectively and the outer radius, R_1 = 0.02 m, was kept with a temperature equal to 2 °C and under a pressure equal to 3 GPa (green arrows). The temperature distribution is expressed by

$$T(r) = 10 - 400r \tag{5.4}$$

The material properties assume the following values: Young's Modulus equals to 1.0 GPa, Poisson's ratio 0.3, and thermal coefficient equals to 0.02 °C^{-1}. The reference temperature was equal to 0°C.

Figure 5.18 – Thermomechanical hollow sphere. Geometry, loadings, boundary conditions and 3D element mesh.

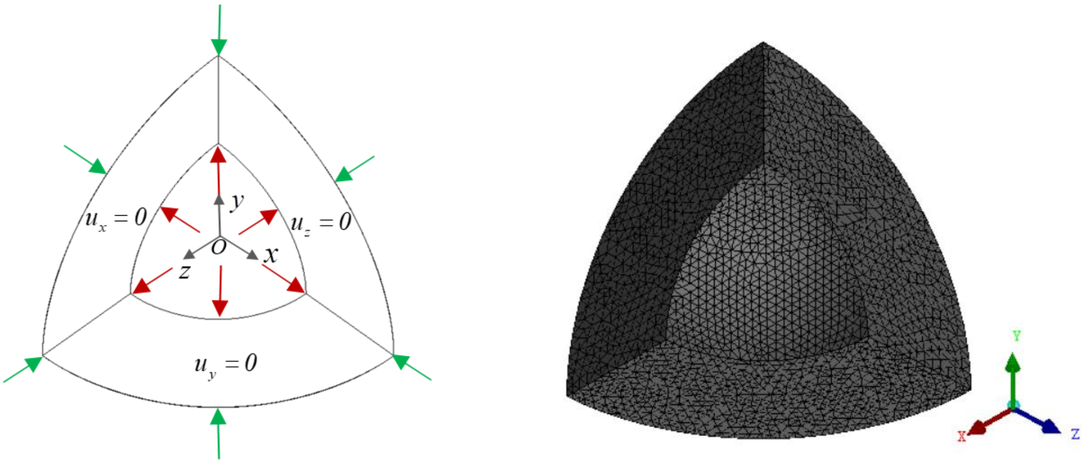

Fig. 5.19 shows the radial displacement as a function of the radius of the hollow sphere and Fig. 5.20 shows the Von Mises equivalent stress as a function of the radius of the hollow sphere. The results for both analyses were collected at the *y-z* symmetry plane and they were averaged over specific radii. Good agreement was achieved between numerical and analytical solutions. Special attention is need to be paid for the Von Mises equivalent stress at the inner radius where a relative error was equal to 7.11%. However, this error can be assumed to be within engineering accuracy. Finally, regardless Fig. 5.19, due to the combination of

loadings acting under the hollow sphere, we can see that now the inner radius became the outer radius and the outer radius became the inner one.

Figure 5.19 – Comparison of radial displacements between EbFVM and analytical solutions.

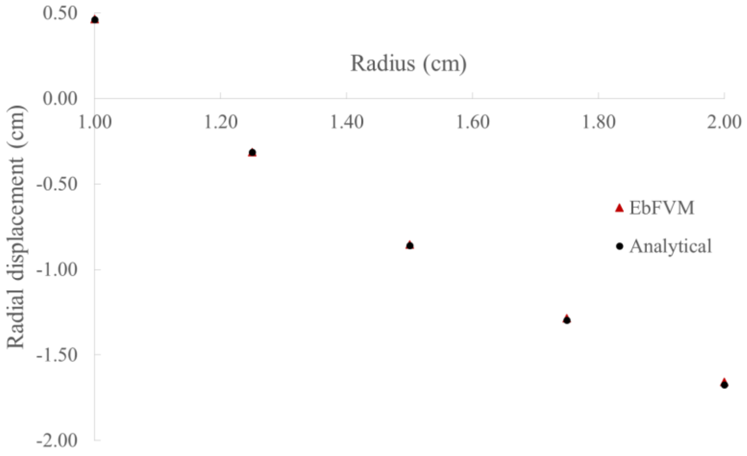

Figure 5.20 – Comparison of Von Mises equivalent stress between EbFVM and analytical solutions.

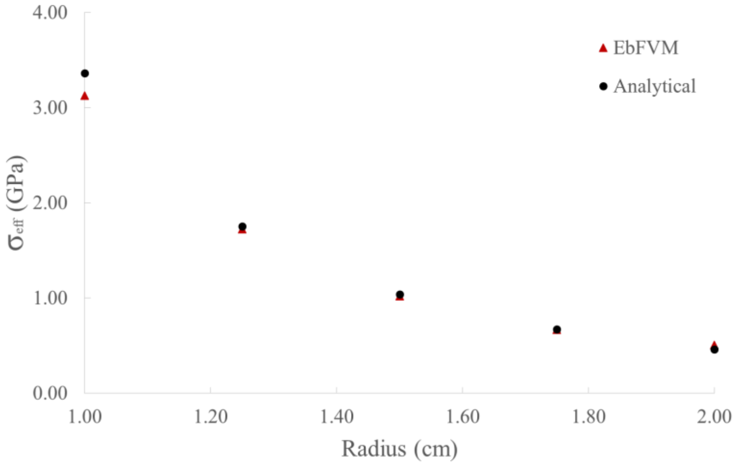

5.3.3 Thermo-elastoplastic thin plate

The present verification test case was performed in a non-uniformly long thin plate subjected to a thermo-elastoplastic loading. The present work is compared with the analytical solution by Boley and Weiner (1962) along with the FVM solution by Demirdžić and martinović (1993). The geometry of the problem, the boundary conditions, and a cross-section of the 3D element mesh are shown in Fig. 5.21. To discretize the domain, a structured mesh composed by 1600 hexahedrons, and 3362 nodes was used. Assumption of plane stress conditions was made by making use of only one element in the normal *z*-direction and assuming that the thickness of the plate is small when compared with the height and width of the plate.

Figure 5.21 – Thermo-elastoplastic long thin plate.

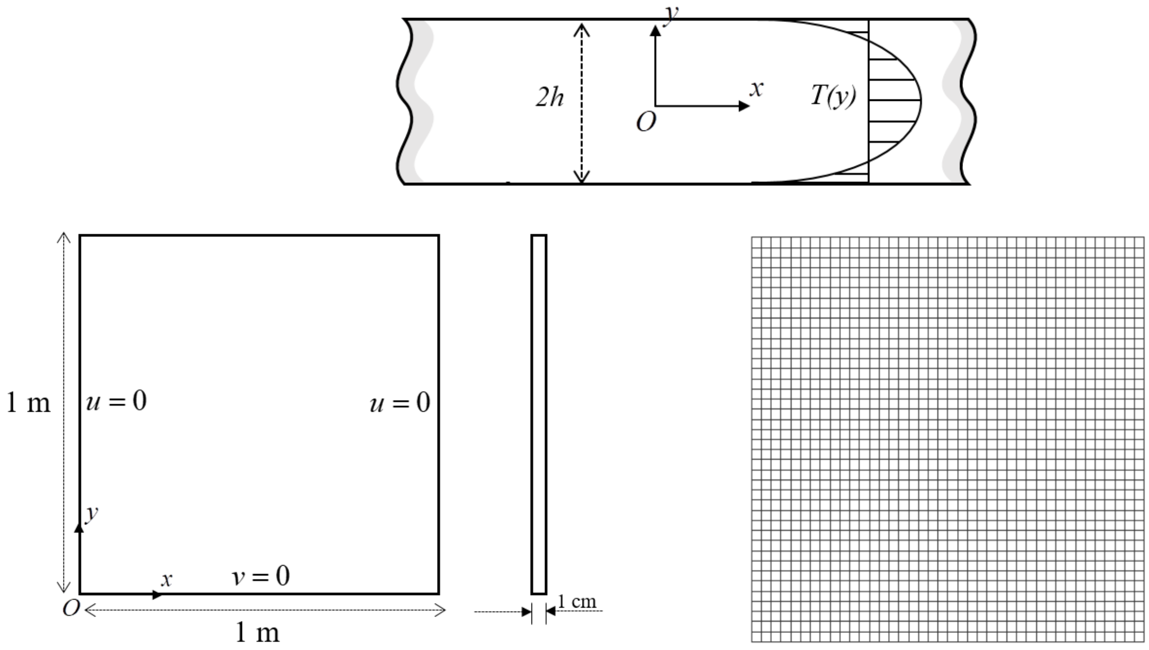

The plate is subjected to a non-uniform temperature distribution expressed by

$$T(y) = T_0\left[\left(\frac{y}{h}\right)^2 - \frac{1}{3}\right] \tag{5.5}$$

where T_o = 600 K, h = 1.0 m, and the reference temperature was equal to 0°C. The thermal load, which is produced by the temperature distribution along the plate, was uniformly distributed throughout the simulation over 10 load steps for the thermo-elastoplastic test case; for the linear thermo-elastic test case only 1 load step was applied for the whole simulation. The material properties used in the simulations are depicted in Table 5.7. The thermo-elastoplastic analysis was carried out under perfectly-plastic conditions.

Table 5.7. Material properties for thermomechanical analysis.

Parameter	Value
Young’s modulus	E = 210 GPa
Yield stress	σ_0 = 210 MPa
Poisson’s ratio	ν = 0.33
Thermal expansion coefficient	α = 9. 5e-6 K^{-1}

Source: Demirdžić and martinović (1993).

Fig. 5.22 compares the vertical displacement of the solution obtained by the present simulation and the analytical solution for the thermo-elastic case and an additional simulation for the thermo-elastoplastic case. As can be seen, excellent agreement was achieved by comparing the numerical and analytical results. Also, we can verify that the vertical displacement reaches an absolute maximum when the T(y) = 0, at Y = 0.58 m, that is, at this point no stress has been produced at all.

Figure 5.22 – Comparison of *y*-displacement between EbFVM and analytical solution.

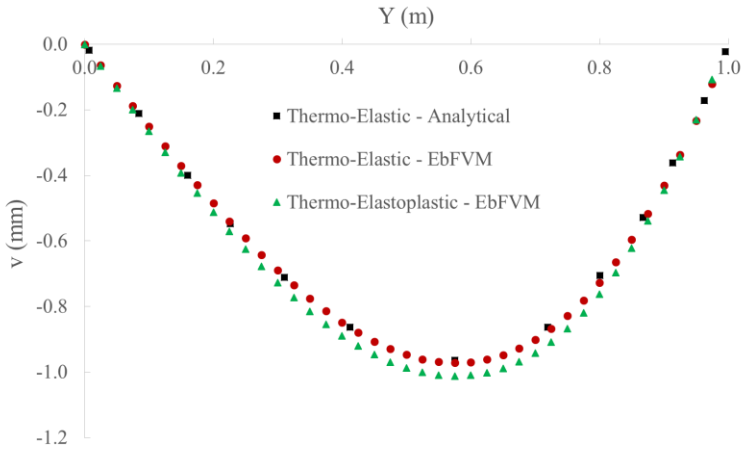

Fig. 5.23 compares the Von Mises equivalent stress of the solution obtained by the present simulation and the FVM solution for both thermo-elastic and thermo-elastoplastic case. As can be seen, fairly good agreement was achieved for both cases. However, for the thermo-

elastoplastic case, the results concerning the plastic region (approximately, 0.4 < Y < 0.7) show considerable divergence. The FVM results appears to be considering material hardening, therefore, further investigations are needed to be performed in order to get final conclusions.

Figure 5.23 – Comparison of the Von Mises equivalent stress between EbFVM and analytical solution.

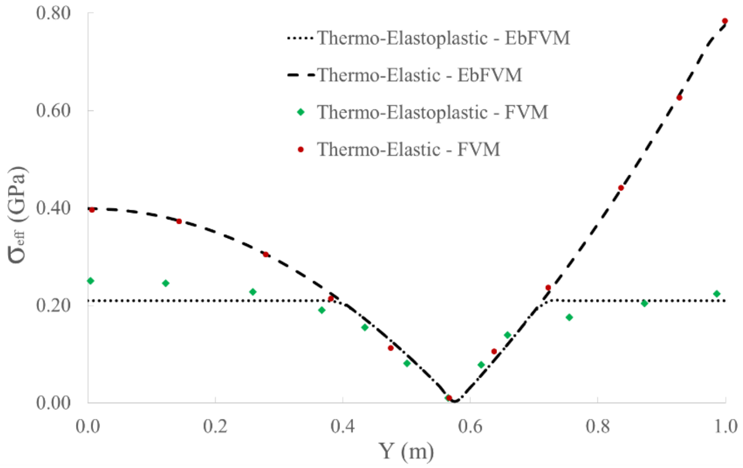

5.3.4 Welding of an aluminum plate

This validation test case was performed by comparing the present work with the GMAW experiment by Masubuchi (1980). For the sake of simplicity, the numerical simulation did not include filler material. Fig. 5.24 shows both geometry (*length = 1220 mm, width = 12.5 mm, height = 152.4 mm*) and the structured mesh used in the EbFVM analysis. The welding torch moves along the longitudinal upper edge. To discretize the domain, a structured mesh composed by 1400 hexahedrons, and 3030 nodes was used. Also, due to symmetry only one-half of the geometry was used, and in addition, zero temperature gradient (Neumann conditions) was set at the symmetry plane for the thermal analysis and perpendicular constraints were set at the symmetry plane (Dirichlet boundary conditions) for the mechanical analysis.

Figure 5.24 – Welding plate. Geometry, boundary conditions and cross-section of the 3D element mesh.

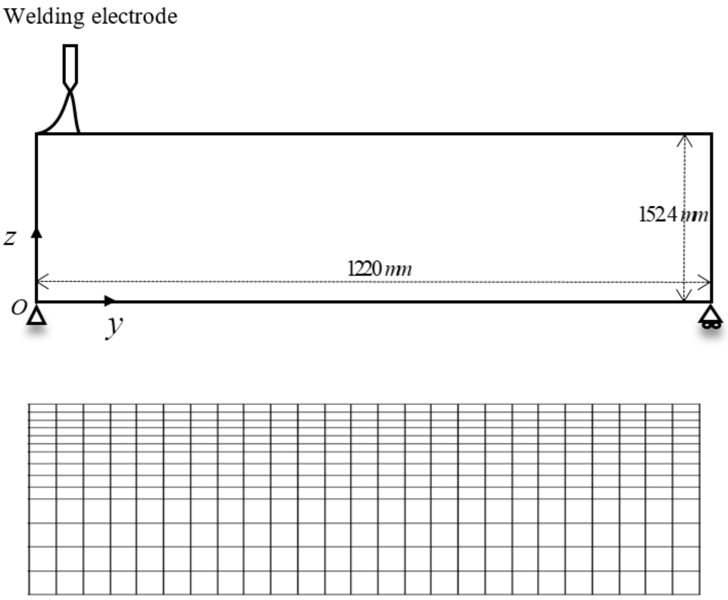

A time-step equal to 1.0 *s* was assumed, loadsteps were kept as 1.0 as well and both were kept constant in the whole simulation. For this simulation, disc-shaped heat source model was adopted (Eq. 3.43) with $a = 6.0$ mm.

The material employed in the simulation is the 5052 H-32 aluminum alloy and its thermal and mechanical temperature-dependent properties are shown in Figs. 5.25 and 5.26, respectively.

Figure 5.25 – Thermal properties of 5052 H-32 aluminum alloy.

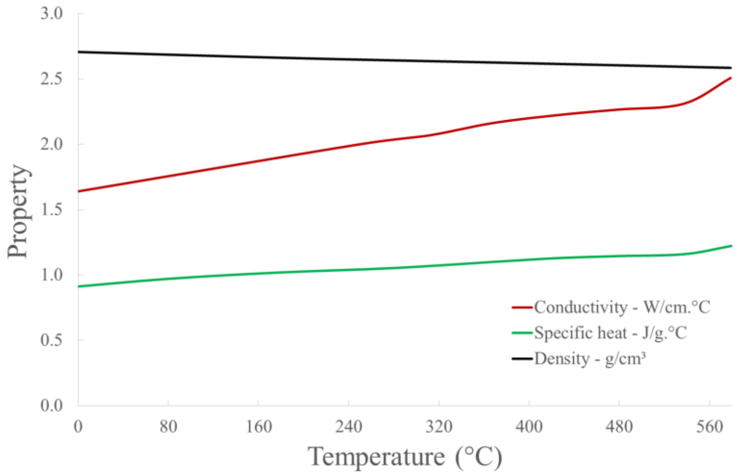

Figure 5.26 – Mechanical properties of 5052 H-32 aluminum alloy.

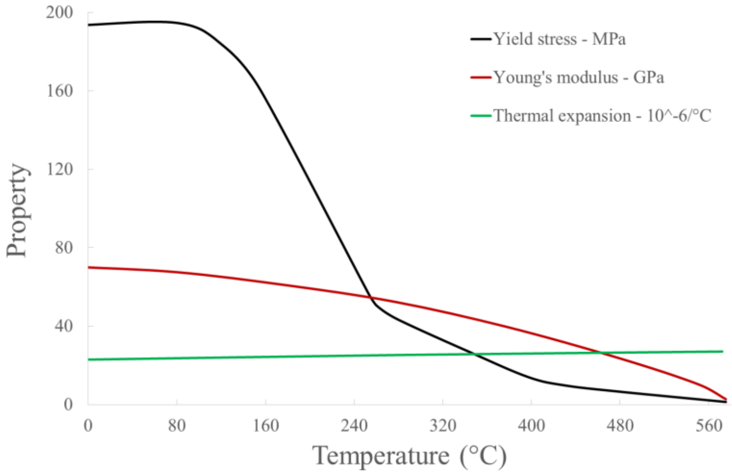

In the present simulation, all thermal properties were taken as function of the temperature, whereas for the mechanical properties the Young's modulus assumed a mean value of 44.5 GPa, the thermal expansion coefficient assumed a mean value of $25.35e^{-6}$ $°C^{-1}$, Poisson's rate was equal to 0.33, and the Yield stress was taken as function of the temperature. Perfectly plastic conditions were assumed. Regarding phase changes, *Solidus* temperature is 880 K, *liquidus* temperature is 922 K and latent heat is $1.076e^9$ J/m^3 whereas for heat losses we considered emissivity equal to 0.03 and heat transfer coefficient equal to 5.0 $W/m^2.K$. Finally, Table 5.8 shows the welding parameters used in the simulation.

Table 5.8. Welding parameters.

Parameter	Value
Current	260.0 *A*
Voltage	23.0 *V*
Efficiency	0.55
Speed	7.34 *mm/s*

Considering the geometry and the aforementioned parameters, the welding torch starts moving at point P_1(0,0,152.4) when time $t=0$ *s* and moves along *y*-axis with a constant speed. Fig. 5.27 depicts the thermal cycles from thermocouples T_1 (0, 635.4, 139.7), T_2 (0, 635.4, 114.3), and T_3 (0, 635.4, 76.2).

Figure 5.27 – Thermal cycles for three different thermocouples for both experimental and EbFVM analysis.

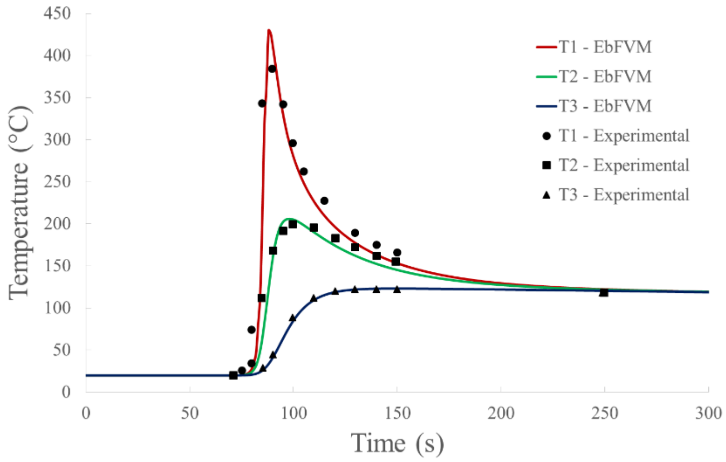

The obtained results, for all three thermocouples, showed fairly agreement with the experiments by fitting it within engineering accuracy. The maximum relative error was observed in thermocouple T_1, at the peak temperature, where it assumes a value of 11.7%.

Fig. 5.28 compares the transient deflection numerically and experimentally. The transient deflection was measured at the lower midpoint of the plate P_2(0, 610, 0). The results match well and the maximum relative error (10.2%) was found at the lower part of the curve when the plate starts to curve downward.

Figure 5.28 – Transient deflection at the plate's lower midpoint for both experimental and EbFVM analysis.

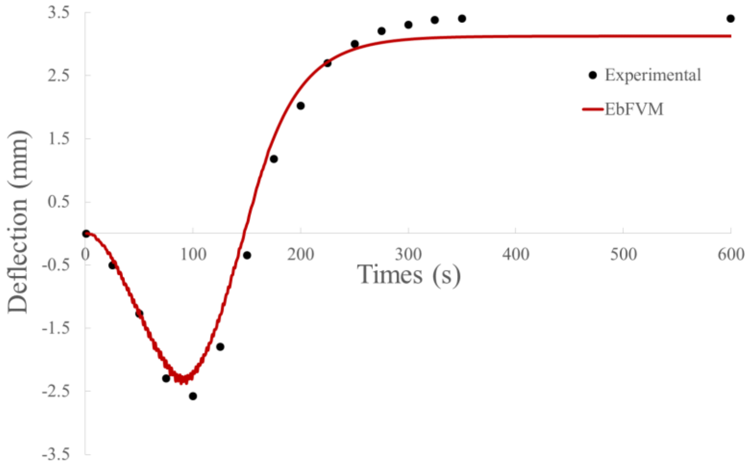

Fig. 5.29 compares the longitudinal residual stress numerically and experimentally. The longitudinal residual stress was measured at the plate's middle section $L_1(0, 610, 0 – 152.4)$ after the plate has been cooled to the room temperature. The results did not fit the experiments well reaching the maximum relative error (59.0%) at the coolest region of the line's middle section. However, as it can be seen, the numerical results are in agreement with literature showing tensile stresses closer to the weld line and compressive stresses far away from these region. In addition, the numerical curve fairly mimics the profile of the curve of the experiments.

Figure 5.29 – Longitudinal residual stress at the plate’s middle section for both experimental and EbFVM analysis.

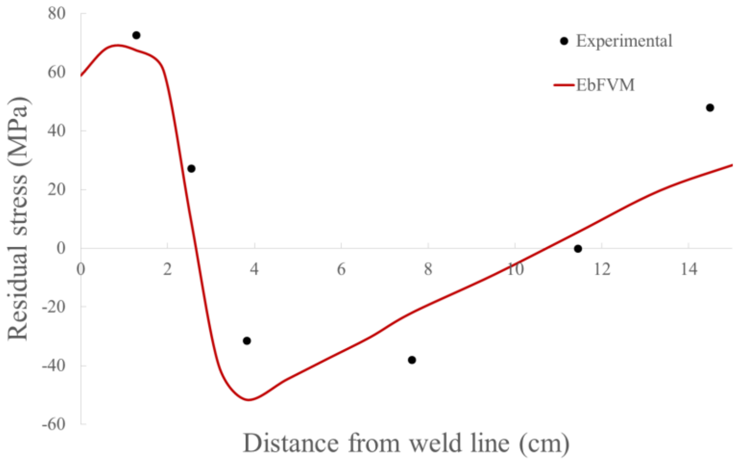

CHAPTER

6

RESULTS AND DISCUSSION

This section presents the results and discussion of the thermomechanical simulations in cylindrical geometries. The first section is concerned with conventional weld analysis, where there is no fluid inside the pipe. Since there is a large amount of works with this kind of simulation, a better understanding of the results can be made through the comparison of present work with the ones found in the literature. The second section adds to the analysis the thermomechanical inputs of the fluid flow inside the pipe. Therefore, by considering the fluid flow in the analysis, we can represent in-service welding processes and obtain a better understanding of the process through parametric studies of the process.

6.1 General aspects of welding in the cylindrical geometries

For both the conventional and in-service welding analyses, girth welding simulations were performed in a full 3D model butt-welded pipe. The geometry, a portion of the mesh (near the weld line), and the welding torch direction are given in Fig. 6.1. The outer pipe diameter, wall thickness, and total length of the pipe are *114.3 mm, 8.0 mm, and 400 mm*, respectively. It is important to stress that the results showing next in sections 6.1 and 6.2 are not specific to any particular welding process. Therefore, the results presented in the former sections can just be compared from qualitative point of view.

Figure 6.1 – Butt-welded pipe, a portion of the mesh near the weld line, and the welding torch direction.

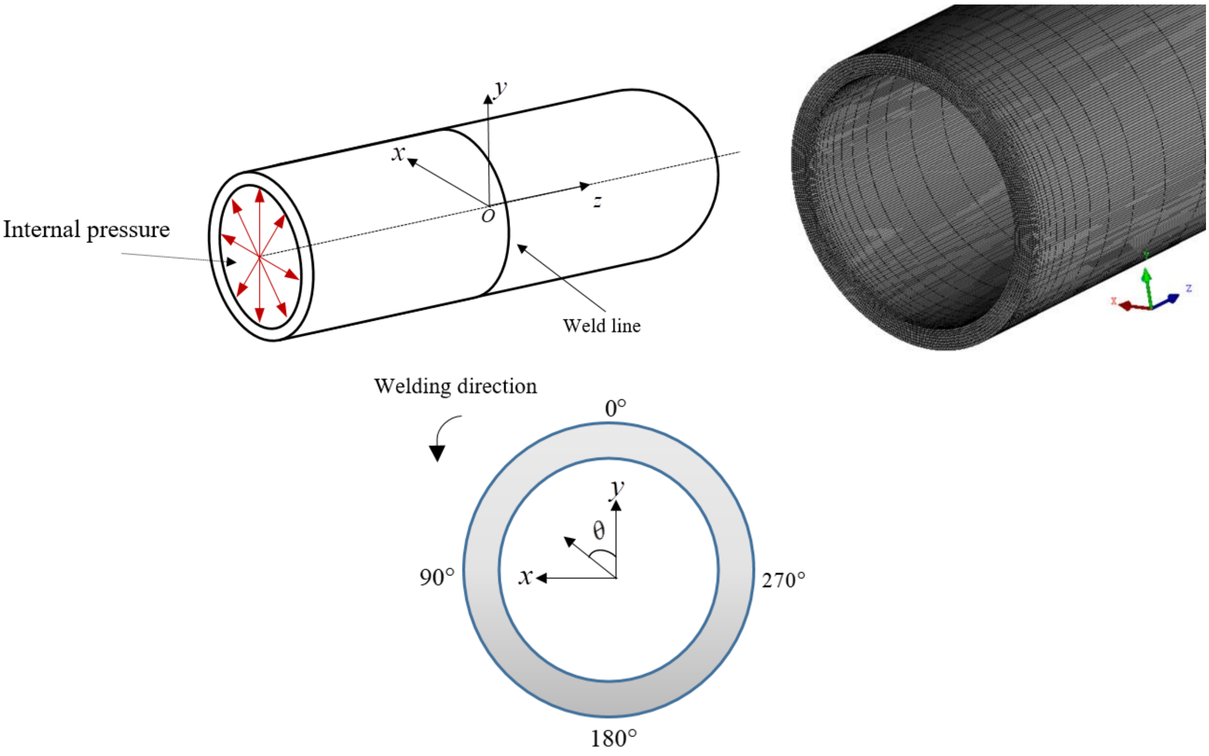

Due to symmetry only one-half of the geometry was simulated. In the thermal analysis, at all boundaries, except the symmetry surface (kept insulated), a combination of natural convection, forced convection (inside the pipe), and radiation losses were applied at the pipe walls. The mechanical boundary conditions (Dirichlet boundary conditions) used in the simulations are shownin Fig. 6.2.

Figure 6.2 – Mechanical boundary conditions at pipe surfaces for the cylindrical geometries.

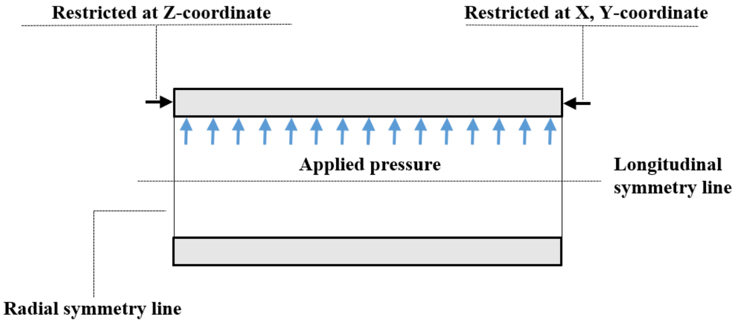

The domain was discretized using an unstructured mesh composed by 7,072 hexahedrons, and 9,520 nodes. In addition, an increment time of 1.0 *s* (thermal simulation) and a loadstep of 1.0 (mechanical simulation) were adopted and kept constants in the whole simulation. For this simulation, a semi-ellipsoidal heat source model was adopted.

The material employed in the simulation is SUS304 stainless steel and the thermal and mechanical properties function of the temperature are shown in Fig. 6.3 and 6.4, respectively.

Figure 6.3 – SUS304 temperature-dependent thermal properties.

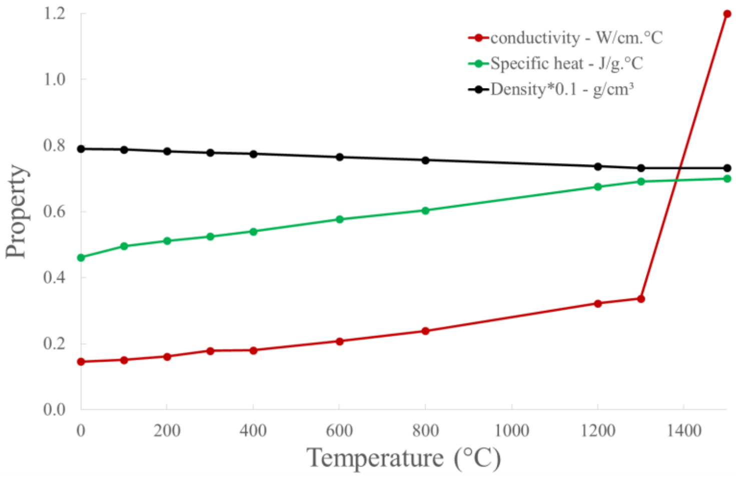

Figure 6.4 – SUS304 temperature-dependent mechanical properties.

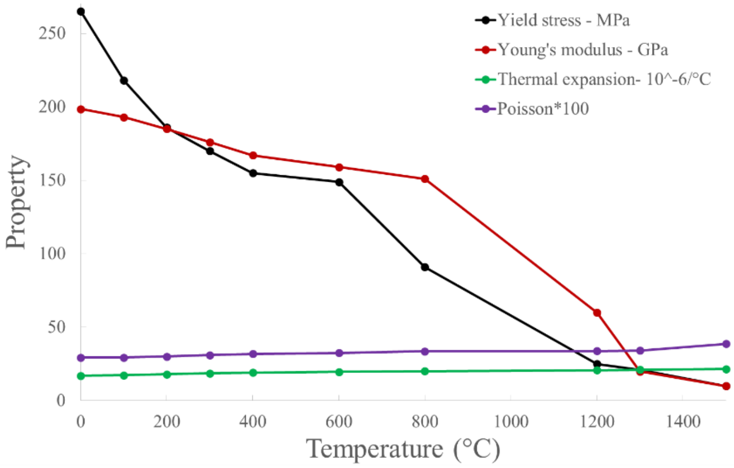

In the present simulations, all thermal properties were taken as function of the temperature, whereas for the mechanical properties due to convergence problems mean mechanical properties were used. Therefore, the following average mechanics properties were used: Young's modulus equal to 132 GPa, thermal expansion coefficient equal to 1.93e^{-5} °C^{-1}, Poisson's rate equal to 0.33, and the Yield stress equal to 129 MPa. Perfectly plastic conditions was assumed. This approach has been shown to give accurate results in welding simulations (Zhu and Chao, 2002).

Considering the aforementioned geometry and parameters, the welding torch starts to move at time *t=0 s* at $\theta = 0°$ (refer to Fig. 6.1) and moves around the whole pipe with a constant speed. The heat source was modelled by a semi-ellipsoid heat source. Welding and geometrical parameters are illustrated in Tables 6.1 and 6.2.

Table 6.1. Welding and geometrical parameters.

Parameter	Value
Current	111 *A*
Voltage	34.05 *V*
Efficiency	0.7
Speed	3 *mm/s*
T_0	20 °C
Room temperature	20 °C
Heat transfer coefficient	15 W/m.K

b, a	6 *mm*, 6 *mm*
c	6 *mm*

Table 6.2. Thermophysical properties for thermal analysis.

Parameter	Value
Latent heat	1.98.10^9 J/m^3
Solidus temperature	1613 *K*
Liquidus temperature	1663 *K*
Emissivity	0.75

In the present work, the main difference between the conventional welding analysis and the in-service welding analysis is related to the boundary conditions at the inner pipe surface. In the conventional welding analysis, heat flux through the inside pipe wall was composed by natural convection and thermal radiation and no pressure was applied at it. In the in-service welding simulations, we will introduce the forced convection instead of natural convection in order to represent the fully-developed turbulent fluid flow into the pipe and apply pressure at the inside pipe wall.

A constant heat transfer coefficient along the inner pipe wall was used and this coefficient was evaluated by the empirical correlation of Dittus-Boelter (Incropera and DeWitt, 1990). As the aforementioned coefficient has larger values for forced convection, the heat transfer coefficient is a key parameter for the in-service welding analysis.

6.2 Conventional welding analysis

Fig. 6.5 depicts the temperature distribution along the pipeline during the welding process. The welding torch starts to move at time *t=0 s* at $\theta = 0^\circ$ and moves around the whole pipe completing a cycle within approximately 120 s. As we can see, the maximum temperature achieved in the weld pool during this process is approximated 2400 °C, whereas the temperature close to the ends of pipe does not exceed the room temperature. Fig. 6.5d represents an instant when the pipeline is already on the cooling stage.

Figure 6.5 – Temperature field at simulation times (a) 10s, (b) 69 s, (c) 105 s, and (d) 182 s.

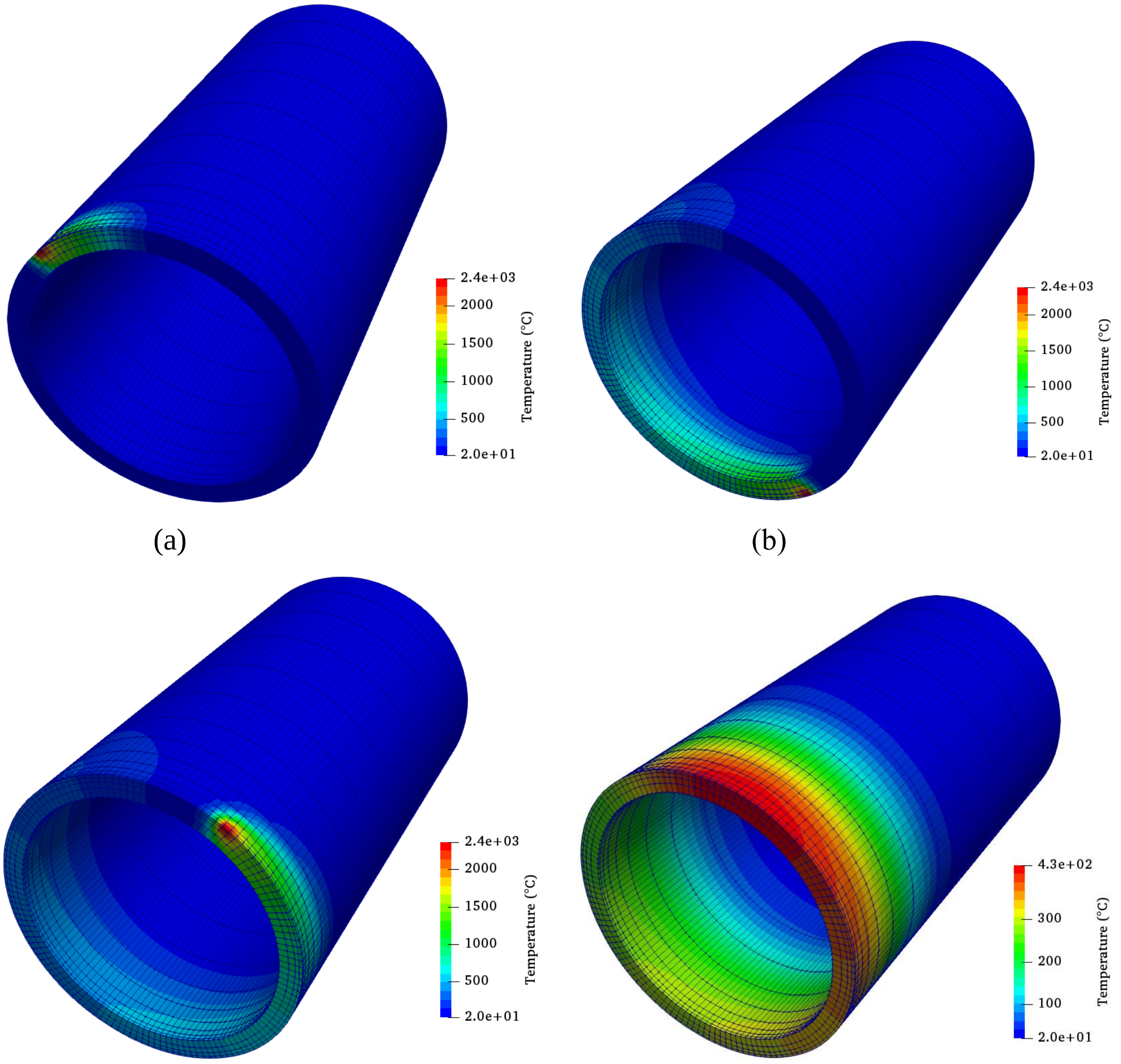

(a) (b)

(c) (d)

Fig. 6.6 shows the temperature profile for a girth butt-welded pipe at the outer pipe surface and $\theta = 90°$ at various moments of the welding simulation after the heat source origin has passed. From this result we can see the abrupt change in the temperature gradient near the weld which is caused by the highly concentrated heat source. This situation affect the stress distribution as we will see afterwards.

Figure 6.6 – Outer surface temperature profile after heat source origin has passed at various moments.

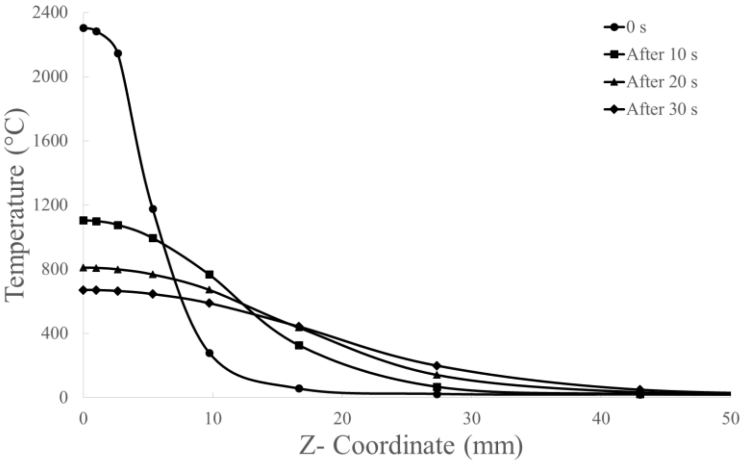

Fig. 6.7 shows thermal cycles at six different locations. From this figure, one can concludes that due to the welding process parameters as well as material properties, the peak temperatures at all the corresponding locations (outside or inside at the symmetry plane) as well as the whole curve profile are identical, which indicates that the heat transfer is in a steady-state regime when the arc welding is moving around the pipe. The latter arguments are strictly related to the Peclet number. Therefore, remainder analyses will be performed at $\theta = 90°$ only.

Figure 6.7 – Thermal cycles at different locations.

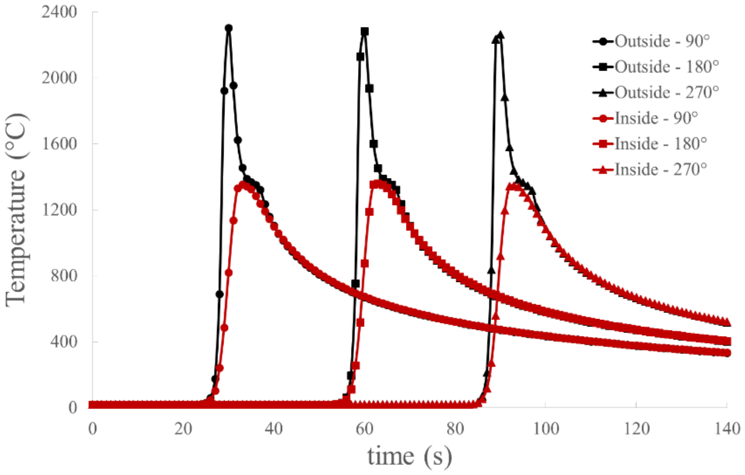

Fig. 6.8(a - b) shows the longitudinal residual stress and the circumferential residual stress along the Z-coordinate. Both of them were measured inside and outside the pipe at various positions along the circumferential direction (hoop coordinate) after the pipe has been cooled to the room temperature. As can be seen, at the weld center line ($Z = 0$) and its surrounding

(HAZ), both axial and hoop residual stresses show tensile stresses at the inner surface and compressive stresses at the outter wall. In the regions far away from the path described by the torch, nearly zero stresses occurred, since in these regions the thermal variation vanishes and the mechanical effects is solely due to the restrictions imposed at the pipe ends. It is also observed that there is a change from tensile to compressive stress and vice versa for all stress distribution. In addition, one may observe that in the welding region permanent plastic strains are developed as the yield strength (129 MPa) is surpassed. Finally, the general profile of both axial and hoop stress shows close analogy with previous works from literature (Brickstad and Josefson, 1998; Deng and Murakawa, 2006; Qureshi, 2008; Obeid et al., 2017).

Figure 6.8 – Axial and hoop stresses at the outer and inner surfaces.

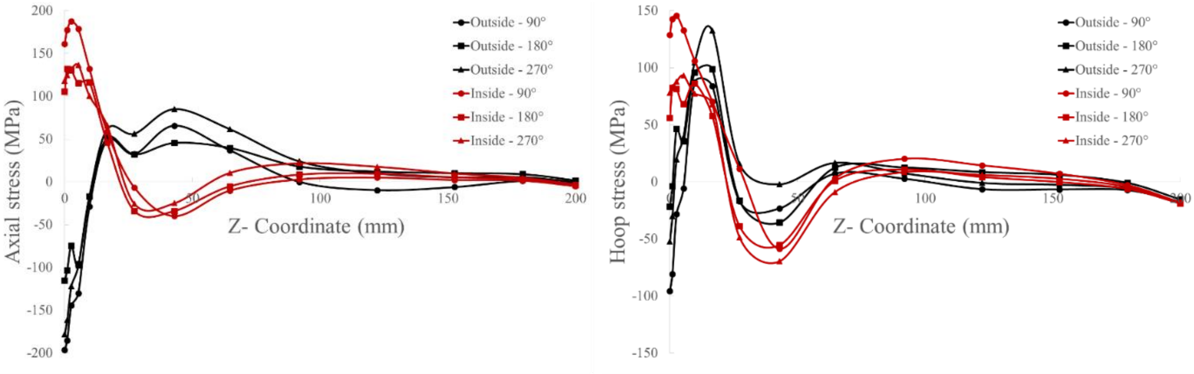

(a) (b)

Fig. 6.9 shows the radial deflection measured at $\theta = 90°$, all over de Z-coordinate for both inside and outside pipe walls. As we can see, after the welding process has been completed, i.e, during the cooling stage, radial contractions take place inside and outside the pipe walls at position $\theta = 90°$.

Figure 6.9 – Residual deflection distribution at $\theta = 90°$.

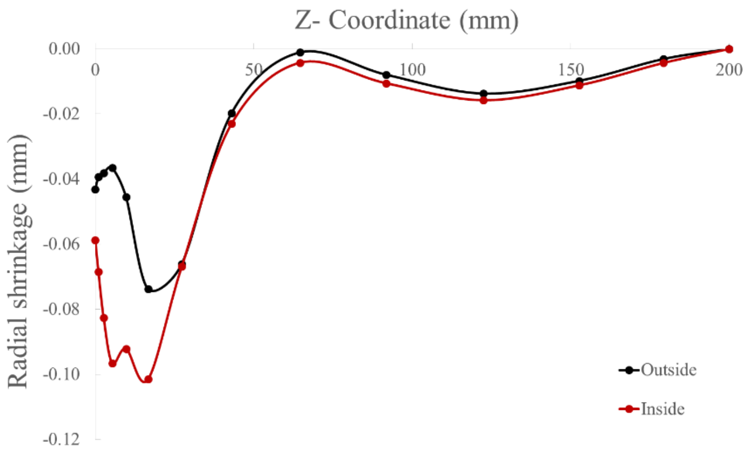

6.3 In-service welding analysis

6.3.1 Varying parameter – fluid velocity

In addition to the previous considerations concerning the conventional welding, the following ones is added to complete the requisites for the in-service welding analysis. Methane was simulated as the working fluid. Thermophysical properties are depicted in Table 6.3.

Table 6.3. Thermophysical data of methane at 4 MPa.

Parameter	Value
ρ [kg/m^3]	28.5
c [kJ/kg.K]	2.623
k.10^2 [W/m.K]	3.211
μ.10^6 [Pa.s]	12.6

Source: Wang et al. (2013).

The influence of fluid velocity in the thermal cycle for CH_4 as working fluid is shown in Fig. 6.10(a-b) and Table 6.4. Fig. 6.10(a) shows that, for the outside surface, the fluid velocity has no significant influence in the peak temperature whereas at the inner surface as long as the fluid velocity increases the peak temperature decreases as shown in Fig. 6.10(b). For both inside and outside surfaces, Table 6.4 show that by increasing the fluid velocity the cooling time decreases leading to the increasing in cooling rates. This tendency indicates that the greater the fluid velocity the more heat is extracted from the inner pipe wall.

Figure 6.10 – Thermal cycles at different locations.

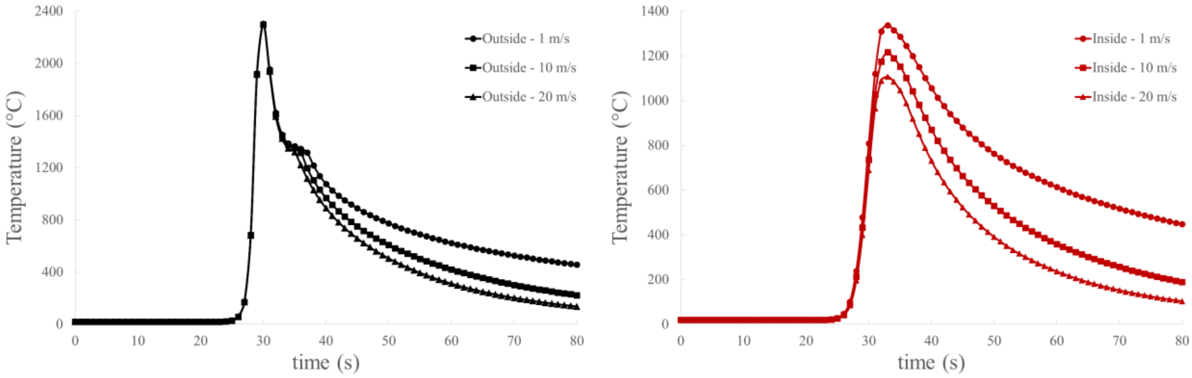

(a) (b)

Table 6.4. Cooling time from 800 to 500°C.

	Δt_{8-5} [s]	
Velocity [m/s]	Outside	Inside
1.0	25	24
10.0	11	10
20.0	8	7

Therefore, in-service welding analyses showed that by increasing the fluid velocity both peak temperatures and the time for cooling the working piece from 800° to 500° decreases. This effect is beneficial because the burn-through effect is avoid. On the other hand, such effect can improve the chance of the appearance of hydrogen-induced cold cracking by originating hard microstructure (martensite) at the pipe wall due to the faster cooling rates. Therefore, proper welding procedures should be applied in order to balance these aspects.

Fig. 6.11(a - d) shows the longitudinal residual stress and the circumferential residual stress along the Z-coordinate. Both of them were measured inside and outside the pipe at $\theta = 90^\circ$ after the pipe has been cooled to the room temperature. As it can be seen, there is no significant difference between the results for velocities of 10 m/s and 20 m/s. Also, at the weld center line and its surrounding (HAZ), the axial residual stresses show tensile stresses at the inside surface and compressive stresses at the outside wall for velocities of 10 m/s and 20 m/s. In the regions far away from the path described by the torch, smaller stresses occurred, since in these regions the thermal variation reduces and the mechanical effects is solely due to the restrictions imposed at the pipe end and the internal pressure of the fluid flow. In addition, one may observe that the smaller the fluid velocity, the greater the stresses. Therefore, in in-service welding processes in order to reduce the chances of appearance of cold cracking (higher stresses), the velocity of the fluid needs to be kept as high as possible and kept in mind the other factors that will be affected by this procedure.

Figure 6.11 – Axial and hoop stress at the outer and inner surfaces at $\theta = 90°$.

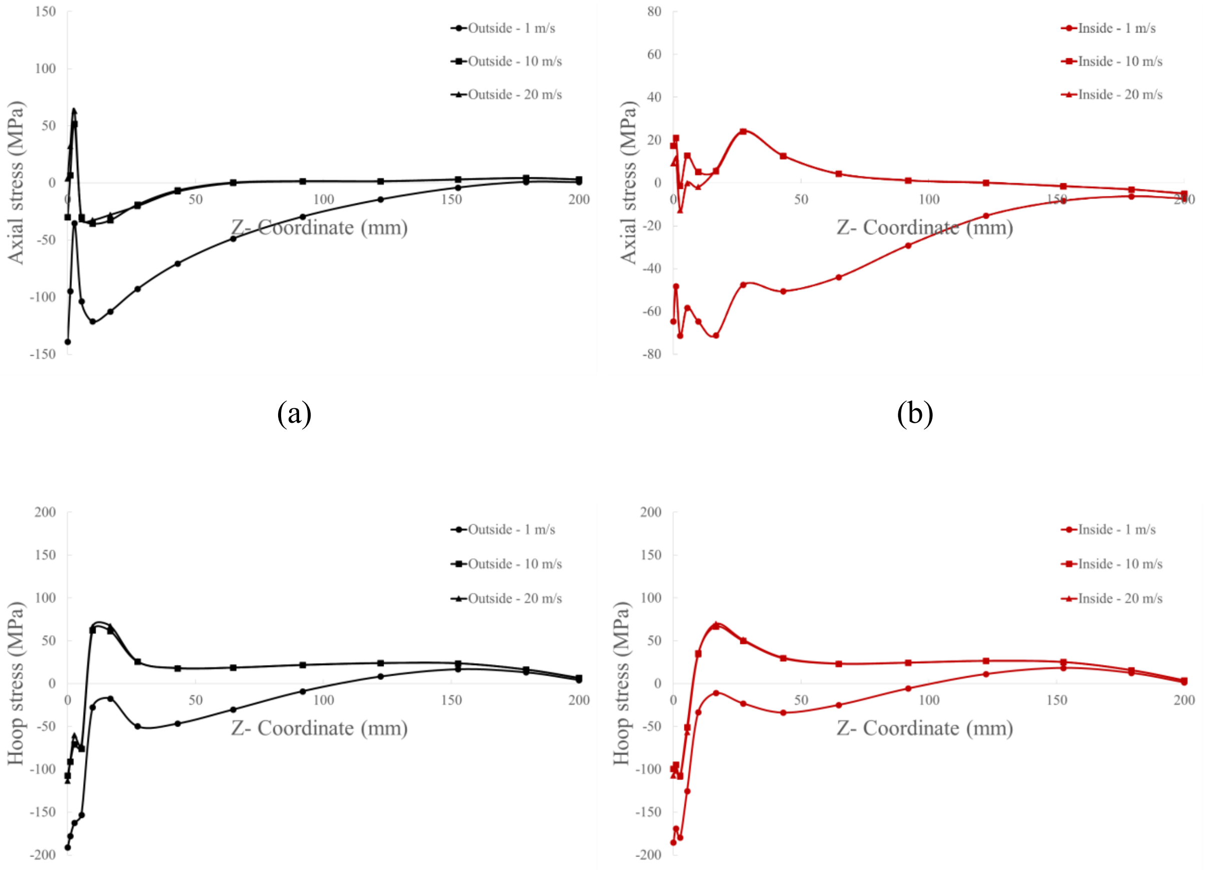

(a) (b)

(c) (d)

Fig. 6.12 shows the radial deflection measured at $\theta = 90°$, all over de Z-coordinate for the inner and outter pipe walls. As we can see, after the welding process has been completed, i.e, during the cooling stage, radial expansions take place inside and outside the pipe walls at position $\theta = 90°$. It is noticeable that no significant difference in the results appeared by changing the fluid velocity.

Figure 6.12 – Residual deflection distribution at $\theta = 90°$.

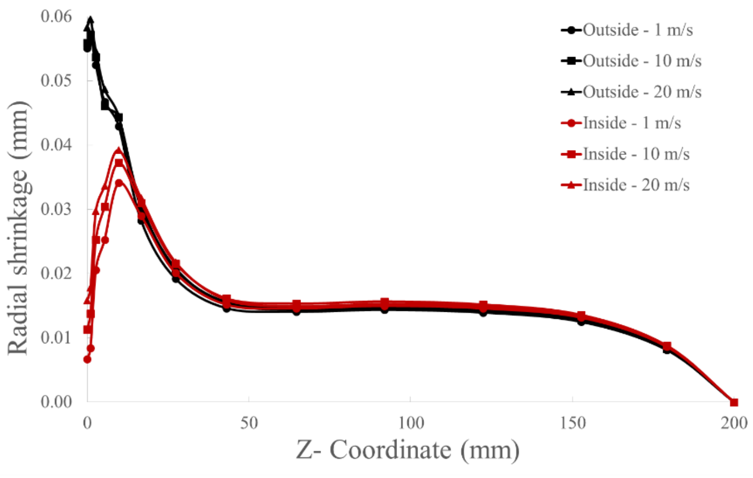

6.3.2 Varying parameter – fluid pressure

In addition to the previous considerations concerning the conventional welding, the following ones is added to complete the requisites for the in-service welding analysis. Methane was simulated as the working fluid at 10 m/s. Thermophysical properties are depicted in Table 6.3.

Table 6.5. Thermophysical data of methane at different pressures.

Parameter	2.0 MPa	CH4 6.0 MPa	8.0 MPa
ρ [kg/m^3]	13.70	44.10	60.8
c [kJ/kg.K]	2.345	2.674	2.867
$k.10^2$ [W/m.K]	3.46	3.84	4.10
$\mu.10^6$ [Pa.s]	11.20	12.16	12.85

Source: Huang et al. (2017).

The influence of fluid pressure in the thermal cycle for CH4 as working fluid is shown in Fig. 6.13(a-b) and Table 6.6. Fig. 6.10(a) shows that, for the outside surface, at $\theta = 90°$, the fluid pressure has no significant influence in the peak temperature whereas at the inner surface as long as the fluid pressure increases the peak temperature decreases as shown in Fig.

6.13(b). For both inside and outside surfaces, at $\theta = 90^{\circ}$, Table 6.6 shows that by increasing the fluid pressure the cooling time decreases leading to the increasing in cooling rates. This tendency indicates that the greater the fluid pressure the more heat is extracted from the inner pipe wall.

Figure 6.13 – Thermal cycles at different locations.

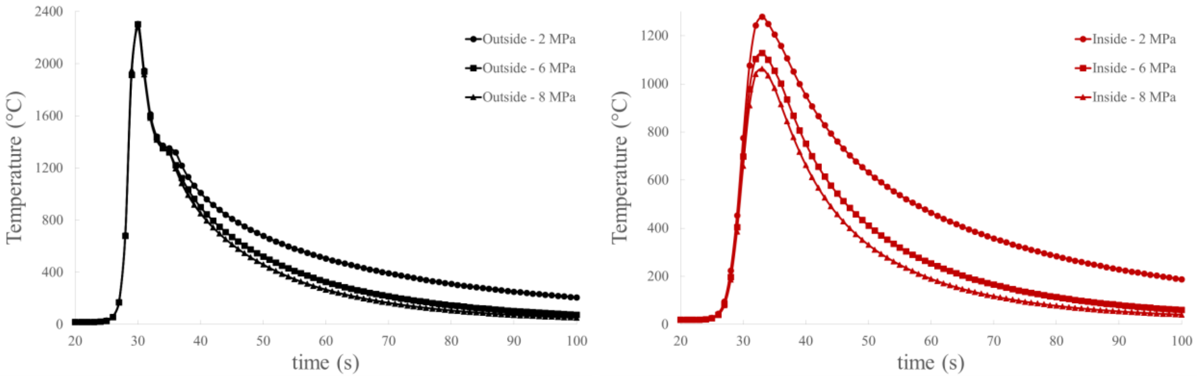

Table 6.6. Cooling time from 800 to 500°C.

	Δt_{8-5} [s]	
Pressure [MPa]	Outside	Inside
2.0	15	13
6.0	9	7
8.0	7	6

Therefore, in-service welding analyses showed that by increasing the fluid pressure both peak temperatures and the time for cooling the working piece from 800° to 500° decreases. On one hand, this is beneficial to avoid burn-through. However, the former effect improves the chance of the appearance of hydrogen-induced cold cracking by originating hard microstructure (martensite) at pipe wall due to the faster cooling rates. Therefore, proper welding procedures should be applied in order to balance these aspects.

Fig. 6.14(a - d) shows the longitudinal residual stress and the circumferential residual stress along the Z-coordinate. Both of them were measured at inner and outter wall at $\theta = 90^{\circ}$ after the pipe has been cooled to the room temperature. As it can be seen, at the weld center line and its surrounding (HAZ), the axial residual stresses shows tensile stresses at the inside surface and compressive stresses at the outside wall for pressure of 2.0 MPa while hoop stress presents only compressive stresses for both inside and outside surfaces at the weld center line and HAZ. In addition, one may observe that the greater the fluid pressure the greater the stresses. Therefore, in in-service welding processes in order to reduce the chances of appearance of cold cracking, the pressure of the fluid needs to be kept as lower as possible and kept in mind the other factors that will be affected by this procedure.

Figure 6.14 – Axial and hoop stress at the outer and inner surfaces at $\theta = 90^\circ$.

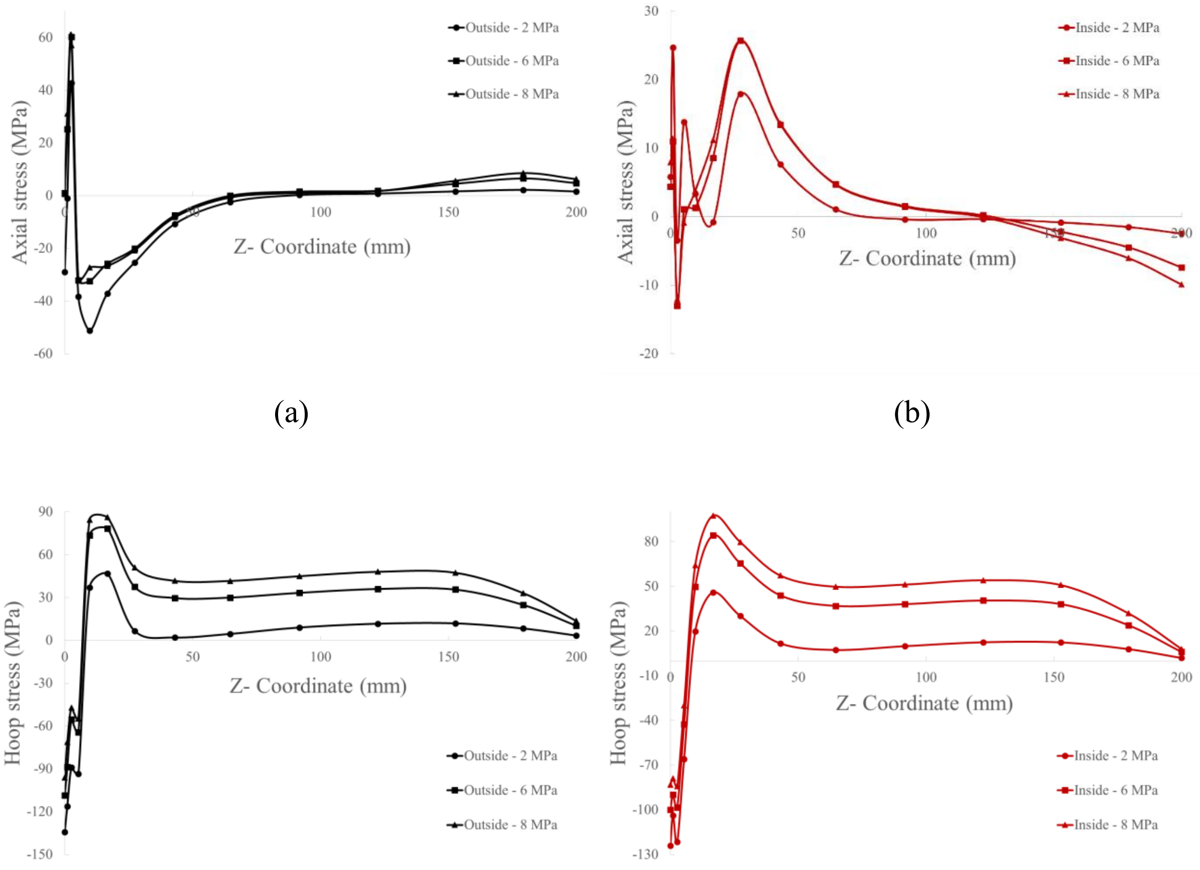

(a)

(b)

(c)

(d)

Fig. 6.15 shows the radial deflection measured at $\theta = 90^\circ$, all over de Z-coordinate for both inside and outside pipe walls. As we can see, after the welding process has been completed, i.e, during the cooling stage, radial expansions take place inside and outside the pipe walls at position $\theta = 90^\circ$. As we expected, as long as the internal pressure is augmented the radial shrinkage also increases and shows greater values at the outside surface.

Figure 6.15 – Residual deflection distribution at $\theta = 90°$.

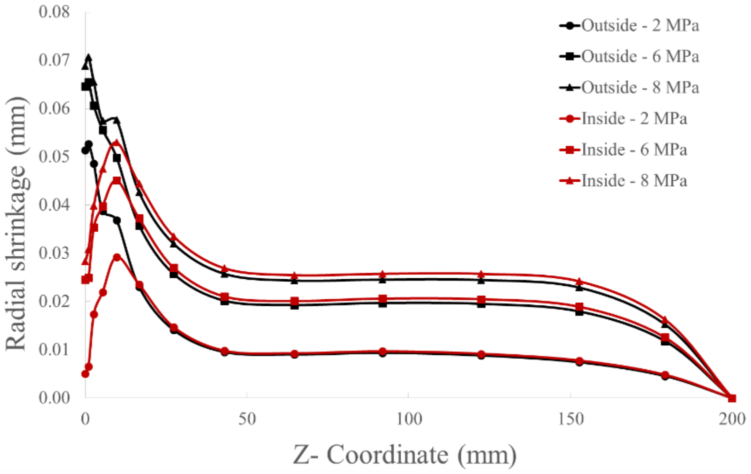

6.3.3 Varying parameter – heat input

In addition to the previous considerations concerning the conventional welding, the following ones is added to complete the requisites for the in-service welding analysis. Methane was simulated as the working fluid at 10 m/s. Thermophysical properties are the same used in section 6.3.1

The influence of the heat input in the thermal cycle for CH_4 as working fluid is shown in Fig. 6.16(a-b) and Table 6.7. Fig. 6.10(a-b) shows that, as long as the heat input increases, the peak temperature also increases in both inner and outer surfaces. For both inside and outside, at $\theta = 90°$, surfaces, Table 6.7 shows that by increasing the heat input the cooling time also increases leading to the decreasing in cooling rates.

Figure 6.16 – Thermal cycles at different locations.

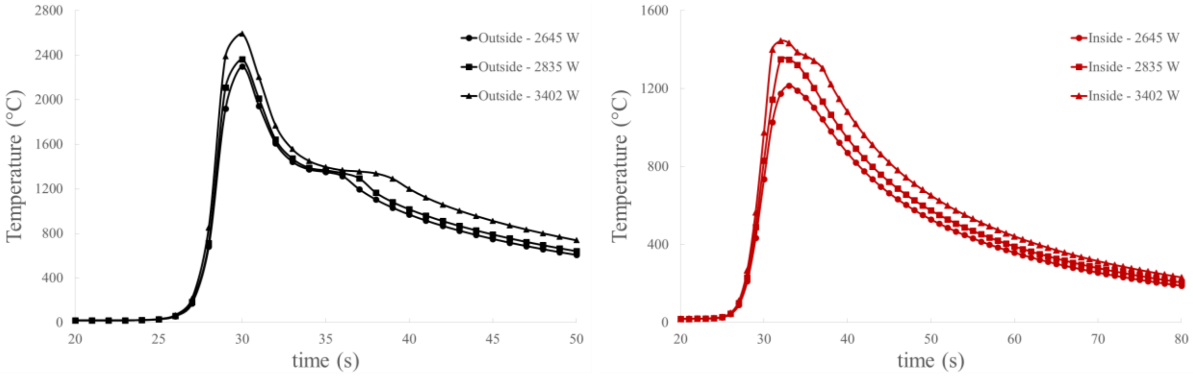

Table 6.7. Cooling time from 800 to 500°C.

	Δt_{8-5} [s]	
Heat input [W]	Outside	Inside
2645	11	10
2835	12	11
3402	13	12

Therefore, in-service welding analyses showed that by increasing the heat input both peak temperatures and the time for cooling the working piece from 800° to 500° increases. On one hand, the slower cooling rates helps to avoid hydrogen-induced cold cracking at pipe wall, on the other hand, this may cause the burn-through effect. Therefore, proper welding procedures should be applied in order to balance these aspects.

Fig. 6.17(a - d) shows the longitudinal residual stress and the circumferential residual stress along the Z-coordinate. Both of them were measured inside and outside the pipe at $\theta = 90°$ after the pipe has been cooled to the room temperature. As it can be seen, at the weld center line and its surrounding (HAZ), the axial residual stresses shows tensile stresses at the inside surface only for the case where the heat input was 2645 W; the other case for both inside and outside surfaces showed compressive stresses. The hoop stresses present only compressive stresses for both inside and outside surfaces at the weld center line and HAZ. In addition, one may observe that the greater the heat input the greater the stresses. Therefore, in in-service welding processes in order to reduce the chances of appearance of cold cracking, the heat input needs to be kept as lower as possible and kept in mind the other factors that will be affected by this procedure.

Figure 6.17 – Axial and hoop stress at the outer and inner surfaces at $\theta = 90°$.

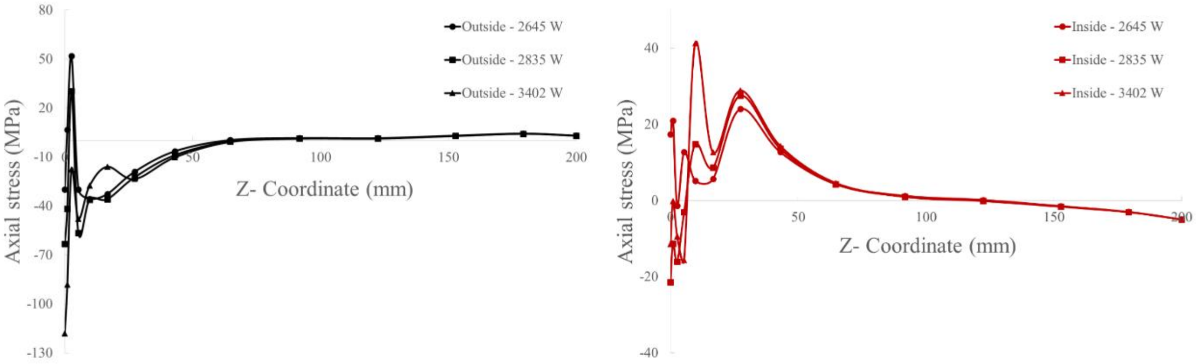

(a) (b)

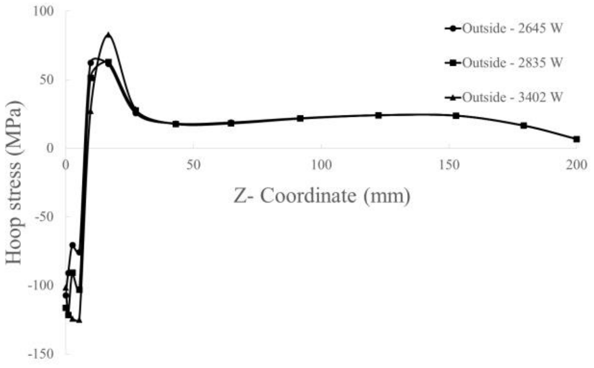

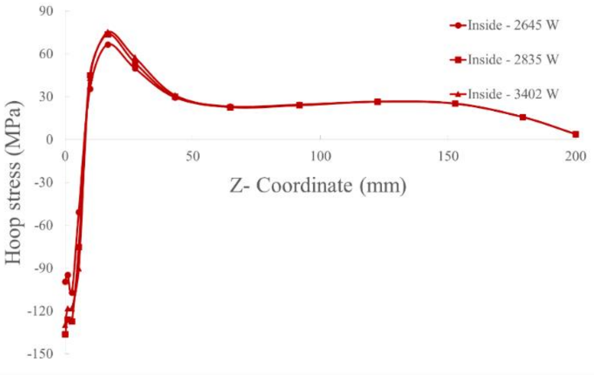

(c) (d)

Fig. 6.18 shows the radial deflection measured at $\theta = 90°$, all over de Z-coordinate for both inside and outside pipe walls. As we can see, after the welding process has been completed, i.e, during the cooling stage, radial expansions take place inside and outside the pipe walls at position $\theta = 90°$ in all cases except when the heat input was 3402 W at the inside wall where radial contractions appeared.

Figure 6.18 – Residual deflection distribution at $\theta = 90°$.

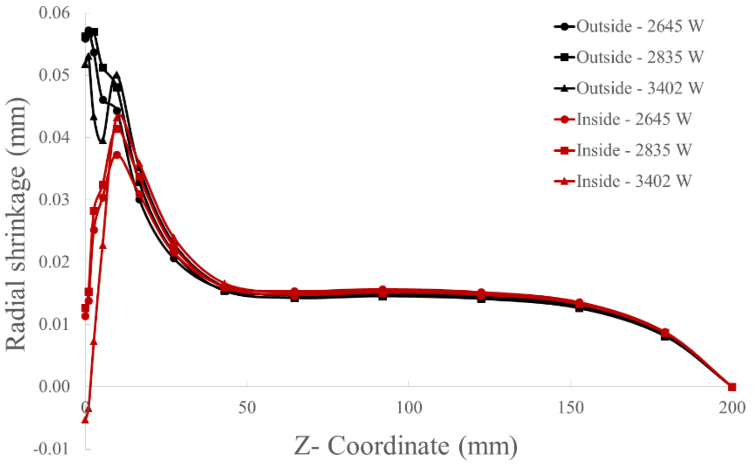

CHAPTER

7

CONCLUSIONS AND FUTURE WORK

In the present work, an Element based Finite-Volume Method (EbFVM) simulator in conjunction with unstructured grids has been developed to give a better understanding of the in-service welding process in order to enhance both the economic benefits, safe welding procedures, and anticipating some risks to the crew and for the process itself. The partial differential equations arising from the physical model (thermal energy and momentum equations) in conjunction with proper boundary conditions and different moving heat source models were discretized by the EbFVM.

The thermo-elastoplastic numerical approach was verified and validated against analytical, numerical, and experimental studies. Also, in general, most of the results were in a good agreements with the works from the literature. From these analyses, it is concluded that the EbFVM simulator can be applied for a whole range of welding simulations and therefore, the addition of internal fluid flow by simulating the in-service welding process it was also possible.

For in-service welding process, it was investigated the influence of the fluid velocity, internal fluid pressure, and heat input to the pipeline. The fluid flow was simulated through the use of empirical correlations. From the analyses of thermal cycles, thermal fields, axial and hoop stress distribution, and radial shrinkage, proper welding procedures were proposed in order to avoid both the burn-through effect and the hydrogen-induced cold cracking at the pipe walls. For instance, through the evaluation of the 3D thermal field and the thermal cycles provided by the electric arc welding to the pipeline, it was possible to analyze the regions with higher risk of burn-through effect and also anticipate the risk of damage of the structure caused by induced thermal stresses and distortions.

Hence, the EbFVM simulator provides an efficient and reliable way to promote the study of a wide range of welding simulations, including in-service welding process. This is possible due to implementation of natural and forced convective and radiative boundary conditions, addition of filler material, different heat sources, stress-strain constitutive relationships as well as different geometry and meshes. Finally, the simulator also has an important implementation of large deformation theory concerning the mechanical analysis. This is a first step in the large deformation theory in our resource group and it will be crucial for analyzing any type of welding condition in the future.

7.1 Future work

In order to perform a more detailed study it is recommended the following analysis for future researches with the developed simulator:

- Perform an experimental work in order to validate the fluid flow and thermomechanical effects for the in-service welding of pipelines;
- Combine CFD techniques with the developed simulator to compare with the results achieved in the present work which applied empirical correlations to describe the internal fluid flow;
- Test different models of plasticity and viscoplasticity as well as the inclusion of the effects of metallurgical transformation on the welded workpiece;
- Perform multipass welding analysis;
- Test other kinds of heat sources such as the conical heat source to simulate Welding Laser Beam;
- Apply mechanical large deformation analysis to welding processes.
- Perform simulations with others working fluids and different states of matter.

REFERENCES

AISSANI, M.; GUESSASMA, S.; ZITOUNI, A.; HAMZAOUI, R.; BASSIR, D.; BENKEDDA, Y., Three-dimensional simulation of 304L steel TIG welding process: Contribution of the thermal flux, Applied Thermal Engineering, v. 89, p. 822-832, 2015.

ALIAN, A. R.; SHAZLY, M.; MEGAHED, M. M., 3D finite element modeling of in-service sleeve repair welding of gas pipelines, International Journal of Pressure Vessels and Piping, v. 146, p. 216-229, 2016.

ANCA, A.; CARDONA, A.; RISSO J.; FACHINOTTI, V.D., Finite element modeling of welding processes, Applied Mathematical Modelling, v. 35, pp. 688-707, 2011

ASL, H. M.; VATANI, A., Numerical analysis of the burn-through at in-service welding of 316 stainless steel pipeline, International Journal of Pressure Vessels and Piping, v. 105-106, p. 49-59, 2013.

BARROSO, A.; CAÑAS, J.; PICÓN, R.; PARÍS, F.; MÉNDEZ, C., UNANUE, I., Prediction of welding residual stresses and displacements by simplified models. Experimental validation, Materials & Design, v. 31, p. 1338-1349, 2010.

BELYTSCHKO, T.; LIU, W. K.; MORAN, B.; ELKHODARY, K. I., Nonlinear Finite Elements for Continua and Structures, John Wiley & Sons, United Kingdom, 2014.

BOLEY, A. B.; WEINER, H. J., Theory of thermal stress, Wiley, New York, 1962.

BOO, K. S.; CHO, H. S., Transient temperature distribution in arc welding of finite thickness plate, Proceeding of Institute of Mechanical Engineering, v. 204, p. 175-183, 1990.

BRICKSTAD, B.; JOSEFSON, B. L., A parametric study of residual stresses in multi-pass butt-welded stainless steel pipes, International Journal of Pressure Vessel and Piping, v. 75, p. 11-25, 1998.

CABEZAS, E. E.; CELENTANO, D. J., Experimental and numerical analysis of the tensile test using sheet specimens, Finite Elements in Analysis and Design, v. 40, p. 555-575, 2004.

CARY, H. B.; HELZER, S. C., Modern welding Technology, 6th edition, Pearson Education, New Jersey, 2004.

CHEN, L.; MI, G.; ZHANG, X.; WANG, C., Numerical and experimental investigation on microstructure and residual stress of multi-pass hybrid laser-arc welded 316L steel, Materials & Design, v. 168, 107653, 2019.

CHRISTENSEN, N.; DAVIES, V.D.L.; GJERMUNDSEN, K., Distribution of temperatures in arc welding, British Weld. J., v. 12, p. 54-75, 1965.

CRISFIELD, M. A., Non-linear finite element analysis of solids and structures, v. 1, Chichester, England, John Wiley and Sons, 1991.

DENG, D.; MURAKAWA, H., Numerical simulation of temperature field and residual stress in multi-pass welds in stainless steel pipe and comparison with experimental measurements, Computational Materials Science, v. 37, pp. 269–277, 2006.

DEMIRDŽIĆ, I.; MARTINOVIĆ, D., Finite volume method for thermo-elasto-plastic stress analysis, Computer Methods in Applied Mechanics and Engineering, v. 109, pp. 331–349, 1993.

DUNNE, F.; PRETRINIC, N., Introduction to computational plasticity, Oxford University Press, New York, 1st edition, 2005.

EAGAR, T. W.; TSAI, N. S., Temperature fields produced by traveling distributed heat sources, 64th AWS convention, Philadelphia, April, 24-29, p. 346-355, 1983.

FACHINOTTI, V. D.; ANCA, A. A.; CARDONA, A., Analytical solutions of the thermal field induced by moving double-ellipsoidal and double-elliptical heat sources in a semi-infinite body, International Journal for Numerical Methods in Biomedical Engineering, v. 27, p. 595-607, 2011.

FACHINOTTI, V. D.; CARDONA, A.; HUESPE, A. E., A fast convergent and accurate temperature model for phase-change heat conduction, International Journal for Numerical Methods in Engineering, v. 44, p. 1863-1884, 1999.

FERRO, P.; PORZNER, H.; TIZIANI, A.; BONOLLO, F., The influence of phase transformation on residual stresses induced by the welding process – 3D and 2D numerical models, Modeling and Simulation in Materials Science and Engineering, v. 14 , p. 117 – 136, 2006.

FLINT, T.F.; FRANCIS, J.A.; SMITH, M.C.; VASILEIOU, A.N., Semi-analytical solutions for the transient temperature fields induced by a moving heat source in an orthogonal domain, International Journal of Thermal Sciences, v. 123, p. 140-150, 2018.

FRIEDMAN, E., Thermo-mechanical analysis of the welding process using the finite element method, Journal Pressure Vessel Technology, Trans. ASME, v. 97, p. 206-213, 1975.

GARCÍA-GARCÍA, V.; CAMACHO-ARRIAGA, J.C.; REYES-CALDERÓN, F., A simplified elliptic paraboloid heat source model for autogenous GTAW process, International Journal of Heat and Mass Transfer, v. 100, p. 536-549, 2016.

GERY, D.; LONG, H.; MAROPOULOS, P., Effects of welding speed, energy input and heat source distribution on temperature variations in butt joint welding, Journal of Materials Processing Technology, v. 167, p. 393-401, 2005.

GOLDAK, J. A.; AKHLAGHI, M., Computational welding mechanics, Springer, 2005.

GOLDAK, J.; CHAKRAVARTI, A.; BIBBY, M., A new finite element model for welding heat sources, Metallurgical Transactions B, v. 15, p. 299-305, 1984.

HASHEMZADEH, M.; CHEN, B.-Q.; SOARES, C. G., Comparison between different heat sources types in thin-plate welding simulation, in: Developments in Maritime Transportation and Exploitation of Sea Resources, 2013.

HILL, R., The Mathematical Theory of Plasticity. London: Oxford University Press, 1950.

HUANG, Z.; TANG, H.; DING, Y.; WEI, Q.; XIA, G., Numerical simulations of temperature for the in-service welding of gas pipeline, v. 248, p. 72 – 78, 2017.

HUGHES, T. J. R.; WINGET, J., Finite rotation effects in numerical integration of rate constitutive equations arising in large-deformation analysis, International Journal for Numerical Methods in Engineering, v. 15, p. 1862-1867, 1980.

INCROPERA, F. P.; DEWITT, D. P., Fundamentals of heat and Mass Transfer, 3rd edition, Wiley, New York, 1990.

JASKE, C. E.; HART, B. O.; BRUCE, W. A., Updated pipeline repair manual, revision 6, Final Report, Project Number R 2269-01R, 2006.

JEFFUS, L., Welding: Principles and applications, Seventh ed., Delmar Cengage Learning, USA, 2012.

KARLSSON, R. I.; JOSEFSON, B. L., Three-Dimensional Finite Element Analysis of Temperatures and Stresses in a Single-Pass Butt-Welded Pipe, Journal of Pressure Vessel Technology, v. 112, p. 76-84, 1990.

KIM, N. H., Introduction to nonlinear finite element analysis, Springer, 2015.

KOMANDURI, R.; HOU, Z. B., Thermal Analysis of the Arc Welding Process: Part I. General Solutions, Metallurgical and Materials Transactions B, v. 31B, p. 1353 -1370, 2000.

KOU, S.; LE, Y. Heat flow during the autogenous GTA welding of pipes, Metallurgical Transactions A, v. 15A, 1165- 1171, 1984.

KOU, S., Welding metallurgy, 2nd edition, John Wiley & Sons, New Jersey, 2003.

KÜCHLER, M. M., Aplicação da técnica da dupla camada na soldagem de dutos em operação, Dissertação. Programa de Pós-Graduação em Engenharia de Minas, Metalúrgica e de Materiais. Universidade Federal do Rio Grande do Sul, Porto Alegre, 2009.

LAW, H.; PRASK, H.; LUZIN, V.; GNAEUPEL-HEROLD, T., Residual stress measuments in coil, linepipe and girth welded pipe, Materials Science and Engineering A, v. 437, p. 60 – 63, 2006.

LIMA, I. A. O. L.; SANTOS, A. A. B., Mathematical approaching and experimental assembly to evaluate the risks of in-service welding in hot tapping, Journal of Pressure Vessel Technology, v. 138, 2016.

LINDGREN, L.-E., Finite element modeling and simulation of welding. Part 2: Improved material modeling, Journal of thermal stresses, v. 24, p. 195-231, 2001.

LINDGREN, L.-E.; RUNNEMALM, H.; NÄSSTRÖM, M.O., Simulation of multipass welding of a thick plate, International Journal for Numerical Methods in Engineering, v. 44, p. 1301-1316, 1999.

LINDGREN, L.-E., Computational Welding Mechanics, Woodhead Publishing Limited, England, 2007.

LI, C.; WANG, Y.; CHEN, Y., Influence of peak temperature during in-service welding of API X70 pipeline steels on microstructure and fracture energy of the reheated coarse grain heat-affected zones, J. Mater. Sci. v. 46, p. 6424–6431, 2011a.

LI, C.; WANG, Y.; HAN, T.; HAN, B.; LI, L., Microstructure and toughness of coarse grain heat-affected zone of domestic X70 pipeline steel during in-service welding, J. Mater. Sci. v. 46, p. 727–733, 2011b.

MAGALHÃES, E.D.S., LIMA E SILVA, A.L.F.D.; LIMA E SILVA, S.M.M.D., A thermal efficiency analysis of a Gas Tungsten Arch Welding process using a temperature moving sensor, International Journal of Thermal Sciences, v. 129, p. 47-55, 2018.

MAJNOUN, P.; GHAVI, M. R.; VAKILI-TAHAMI, F.; ADIBEIG, M. R., A new thermo-mechanical approach to predict 'burn-through' during the in-service welding, International Journal of Pressure Vessels and Piping, v. 194, 104558, 2021.

MALISKA, C. R., Heat transfer and computational fluid mechanics, 2nd edition, LTC Editora, Rio de Janeiro, 2004. (In Portuguese)

MANEERATANA, K., Development of the finite volume method for non-linear structural applications, Thesis. Department of Mechanical Engineering. University of London, London, 2000.

MARCONDES, F.; SANTOS, L.O.S.; VARAVEI, A.; SEPEHRNOORI, K., A 3D hybrid element-based finite-volume method for heterogeneous and anisotropic compositional reservoir simulation, Journal of Petroleum Science and Engineering, v. 108, p. 342-351, 2013.

MASUBUCHI, K., Analysis of welded structures, Oxford, UK, Pergamon Press, 1980.

MENDEZ, P.F. Joining metals using semi-solid slurries. *Master's Thesis*, Department of Materials Science and Engineering, Massachusetts Institute of Technology, 1995.

MOSLEMI, N.; ABDI, B.; GOHARI, S.; SUDIN, I.; REDZUAN, N.; AYOB, A.; AHMED, M.; RHEE, S.; BURVILL, C., Influence of welding sequences on induced residual stress and distortion in pipes, Construction and Building Materials, v. 342, p. 127995, 2022.

NETO, E. A. S.; PERIĆ, D.; OWEN, D. R. J., Computational methods for plasticity: Theory and applications, John Wiley and Sons, Chichester UK, 2008.

NGUYEN, N.T.; OHTA, A.; MATSUOKA, K.; SUZUKI, N.; MAEDA, Y., Analytical solutions for transient temperature of semi-infinite body subjected to 3-D moving heat sources, Weld. J., v. 78, p. 265–274, 1999.

OBEID, O.; ALFANO, G.; BAHAI, H.; JOUHARA, H., A parametric study of thermal and residual stress fields in lined pipe welding, Thermal Science and Engineering Progress, v.4, p. 205–218, 2017.

OKANO, S.; MOCHIZUKI, M., Transient distortion behavior during TIG welding of thin steel plate, Journal of Materials Processing Technology, v. 241, p. 103-111, 2017.

PAVELIC, V.; TANBAKUCHI, R.; UYEHARA, O.A.; MYERS, P.S., Experimental and computed temperature histories in gas tungsten arc welding of thin plates, Weld. J., v. 48, p. 295–305, 1969.

PEREIRA, A. S., Soldagem em operação de tubos API de alta resistência e baixa espessura com ênfase na perfuração e trincas a frio, Tese. Programa de Pós-Graduação em Engenharia Mecânica. Universidade Federal de Santa Catarina, Florianópolis, 2012.

PIMENTA, P. V. C. L., Simulation of the thermal-mechanical continuous casting process using unstructured grids, Dissertation. Graduate Program in Engineering and materials Science. Federal University of Ceará, Fortaleza, 2019.

PIMENTA, P. V. C. L.; MARCONDES, F. Two-dimensional rate-independent plasticity using the element-based finite volume method. Journal of the Brazilian Society of Mechanical Sciences and Engineering, Springer, v. 41, n. 3, p. 142, 2019.

PINSKY, P. M.; ORTIZ, M.; PISTER, K. S., Numerical integration of rate constitutive equations in finite deformation analysis, Computer Methods in Applied Mechanics and Engineering, v. 40, pp. 137-158, 1983.

QURESHI, M. E., Analysis of residual stresses and distortions in circumferentially welded thin-walled cylinders, Dissertation, 2008.

RADAJ, D., Heat effects of welding: Temperature field, residual Stress, distortion, 1st edition, Springer-Verlag, Berlin, 1992.

RIKALIN, N.; BEKETOV, A., Calculating the thermal cycle in the heat affected zone from the two dimensional outline of the molten pool, Welding production, p. 42-47, 1967.

ROSENTHAL, D., Mathematical theory of heat distribution during welding and cutting, Weld. J., v. 20, pp. 220-234, 1941.

SABAPATHY, P. N.; WAHAB, M. A.; PAINTER, M. J., Numerical models of in-service welding of gas pipelines, Journal of Materials Processing Technology, .v. 118, p. 14-21, 2001.

SABAPATHY, P. N., Predicting welding cooling rates and the onset of failure during in-service welding, Dissertation, Department of Mechanical Engineering, University of Adelaide, Adelaide, 2002.

SATTARI-FAR, I.; FARAHANI, M. R., Effect of weld groove shape and pass number on residual stresses in butt-welded pipes, International Journal of Pressure Vessels and Piping, v. 86, p. 723 – 731, 2009.

SHARMA, S. K.; MAHESHWARI, S., A review on welding of high strength oil and gas pipeline steels, Journal of Natural Gas Science and Engineering, v. 38, p. 203-217, 2017.

SILVA, C. C.; FARIAS, J. P., Non-uniformity of residual stress profiles in butt-welded pipes in manual arc welding, Journal of Materials Processing Technology, v. 99, p. 452–455, 2008.

SLADEK, J. V.; SLADEK, V.; MARKECHOVA, I., Boundary Element Methods Analysis of Stationary Thermoelasticity Problems in Non-homogenous Media, International Journal for Numerical Methods in Engineering v. 30, p. 505-516, 1990.

TAHAMI, F. V.; MAJNOUN, P.; ASL, A. Z., Controlling the in-service welding parameters for T-shape steel pipes using neural network, International Journal of Pressure Vessels and Piping, v. 175, 2019.

TAYLOR, G. A.; HUGHES, M.; STRUSEVICH, N.; PERICLEOUS, K., Finite volume methods applied to the computational modelling of welding phenomena, Applied Mathematical Modelling, v. 26, p. 311-322, 2002.

THOMAS, B. G.; SAMARAZEKERA, I. V.; BRIMACOMBE, J. K., Comparison of numerical modeling techniques for complex, two-dimensional, transient heat-conduction problems, Metallurgical Transactions B, v. 15B, p. 307 – 318, 1984.

TIMOSHENKO, S. P.; GOODIER, J. N., Theory of elasticity. McGraw-Hill, New York, 1970.

TRAIDIA, A.; ROGER, F.; GUYOT, E.; SCHROEDER, J.; LUBINEAU, G., Hybrid 2D–3D modelling of GTA welding with filler wire addition, International Journal of Heat and Mass Transfer, v. 55, p. 3946-3963, 2012.

User’s guide for Ansys CFX Release 14.0, Ansys Inc., 2011.

VELAGA, S. K.; KUMAR, S. A.; RAVISANKAR, A.; VENUGOPAL, S., Weld characteristics of non-axisymmetrical butt-welded branch pipe T-joints using finite element simulation and experimental validation, International Journal of Pressure Vessels and Piping, v. 150, p. 72 – 88, 2017.

VERSTEEG, H. K.; MALALASEKERA, W., An introduction to computational fluid dynamics, 2nd edition, Harlow, 2007.

WADE, J. B., Effect of diameter and thickness on hot-tapping practice, Aust. Wed. Res. v.11, pp. 55-56, 1982.

WAHAB, M. A.; SABAPATHY, P. N.; PAINTER, M. J., The onset of pipewall failure during “in-service” welding of gas pipelines, Journal of Materials Processing Technology, v. 168, p. 414-422, 2005.

WANG, Y.; WANG, L.; DI, X.; SHI, Y.; BAO, X.; GAO, X., Simulation and analysis of temperature field for in-service multi-pass welding of a sleeve fillet weld, Computational Materials Science, v. 68, p. 198-205, 2013.

WILCOX, D. C., Turbulence modeling for CFD, 3rd edition, Canada: DCW Industries, 2006.

XU, J.J.; GILLES, P.; DUAN, Y.G.; YU, C., Temperature and residual stress simulations of the NeT single-bead-on-plate specimen using SYSWELD, International Journal of Pressure Vessels and Piping, v. 99-100, p. 51-60, 2012.

ZHU, X.K.; CHAO, Y.J., Effects of temperature-dependent material properties on welding simulation, Computers & Structures, v. 80, p. 967-976, 2002.

APPENDIX
A

LARGE DEFORMATION ANALYSIS

This appendix presents numerical verification of the MPE_EbFVM (multi-physics environment) developed code concerning large deformation cases. We have performed some verification test cases for both elastic and elastoplastic mechanical problems.

A.1 Unit cube subjected to simple tension

This section presents a verification test case involving just elastic mechanical effects provided by a simple tension uniformly distributed in the top side of the unit cube. The geometry of the problem, and the applied load are represented in Fig. A.1. The analysis was carried out for both Jaumann rate of the Cauchy stress and Jaumann rate of the Kirchhoff stress and compared to analytical solutions, see Crisfield (1991) and Pinsky et al. (1983), respectively. For discretize the domain, a structured mesh composed by 1 hexahedron, and 8 nodes was used. For the Jaumann rate of the Cauchy stress analysis, perpendicular constraints were set at symmetry planes (Dirichlet boundary conditions at faces 1, 2, and 3).

Figure A.1 – Unit cube subjected to applied load.

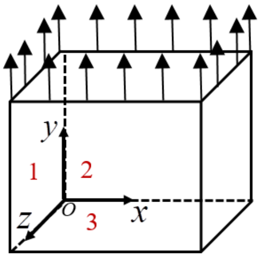

Table A.1 presents the material properties and applied load used in the simulation.

Table A.1. Material properties, and applied load.

Parameter	Value
Applied pressure	68 GPa
Young’s modulus	200.0 GPa
Poisson’s ratio	0.30

Source: Maneeratana (2000).

Fig. A.2 shows the comparison between large deformation theory and small deformation theory with analytical solution by using Jaumann rate of the Cauchy stress. The load step used was 0.01. As we can see, excellent agreement was achieved by comparing the numerical and analytical results concerning the large deformation analysis. It is important to see that for small deformations the approaches coincide.

Figure A.2 – Comparison between large deformation theory and small deformation theory with analytical solution by using Jaumann rate of the Cauchy stress.

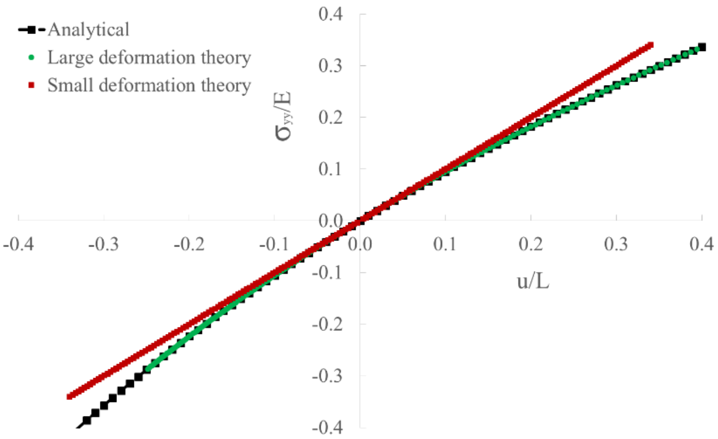

For the Jaumann rate of the Kirchhof stress analysis, Young's modulus is 200 GPa and Poisson's rate is 0.3. Plane strain approach is considered by applying the following boundary conditions presented at Table A.2 in the unit cube presented in Fig. A.1.

Table A.2. Boundary conditions.

Wall	Restricted at direction
Left	Free surface
Right	x
Top	Free surface
Bottom	y
Back	z
Front	z

Fig. A.3 shows the comparison between large deformation theory and small deformation theory with analytical solution by using Jaumann rate of the Cauchy stress. The load step used was 0.001. As we can see, excellent agreement was achieved by comparing the numerical and analytical results concerning the large deformation analysis. It is important to see that for small deformations the approaches coincide where the stretch ratio tends to 1.

Figure A.3 – Comparison between large deformation theory and small deformation theory with analytical solution by using the Jaumann rate of the Kirchhoff stress rate

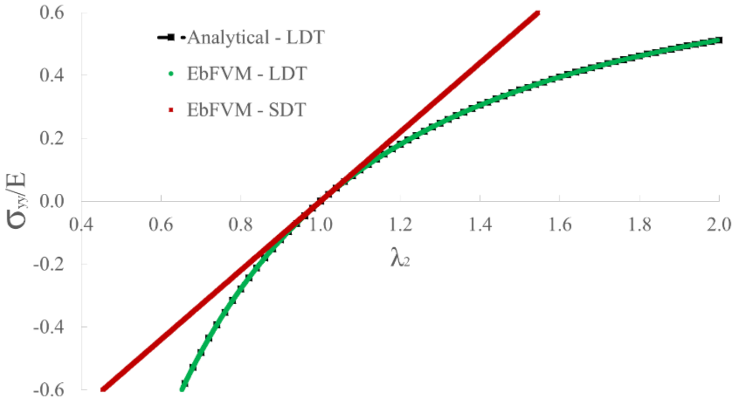

A.2 Unit cube subjected to simple shear

This section presents a verification test case involving just elastic mechanical effects provided by a simple shear tension uniformly distributed in the top side of the unit cube. The geometry of the problem at initial and final configuration, and the applied shear load are represented in Fig. A.4. The analysis was carried out for both Jaumann rate of the Cauchy stress and Jaumann rate of the Kirchhoff stress and compared to analytical solution, see Pinsky et al. (1983), respectively. For discretize the domain, a structured mesh composed by 1 hexahedron, and 8 nodes was used.

Figure A.4 – Unit cube subjected to simple shear loads

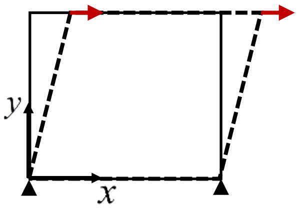

The material properties and the boundary conditions for the simple shear test case are shown in Table A.3.

Table A.3. Material properties and boundary conditions for the simple shear test case.

Parameter	Value
B.C at top surface	$v = w = 0$
B.C at bottom surface	$u = v = w = 0$
Young’s modulus	200.0 GPa
Poisson’s ratio	0.30

Since for the simple shear problem one has isochoric deformation, that is $J = 1$, Fig. A.5 shows the comparison between EbFVM and analytical solution by using the Jaumann rate of both Cauchy and Kirchhoff stress rate. The load step used was 0.001. As we can see, excellent agreement was achieved by comparing the numerical and analytical results.

Figure A.5 – Comparison between EbFVM and analytical solution by using the Jaumann rate of the Cauchy/Kirchhoff stress rate

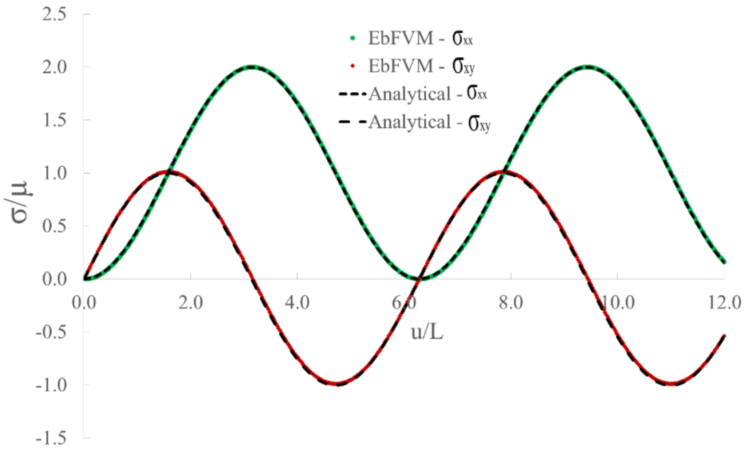

A.3 Tensile test of SAE 1045

The present validation test case was performed in a sheet specimen of SAE 1045 steel subjected to tensile test. The present work is compared with the experiments by Cabezas and Celentano (2004). The geometry of the problem, and the 3D element mesh are shown in Fig. A.6. For discretize the domain, a structured mesh composed by 3150 hexahedron, and 3968 nodes was used. A localized refinement was made where the structure is expected to failure. Due to symmetry, only one-eighth of the geometry was used, and in addition, perpendicular constraints were set at symmetry planes (Dirichlet boundary conditions).

Figure A.6 – Geometry and 3D mesh of the sheet specimen. Load step (0.01)

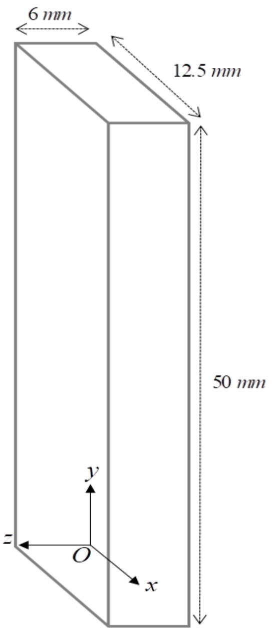

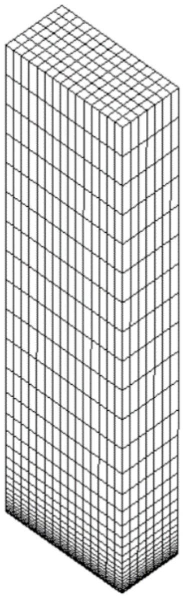

The material properties for the tensile test are shown in Table A.4.

Table A.4. Material properties the tensile test.

Parameter	Value
Poisson’s ratio	0.30
Young’s modulus	222000 MPa
Yield strength	450 MPa
Hardening modulus	8000 MPa

Fig. A.7 plotted the engineering stress-strain curve. From the results, one can see good agreement between numerical predictions and experiments by Cabezas and Celentano (2004). The maximum relative error is 4.9% which is observed at the transition from elastic to plastic behavior. The error is within engineering accuracy.

Figure A.7 – Engineering stress-strain curve.

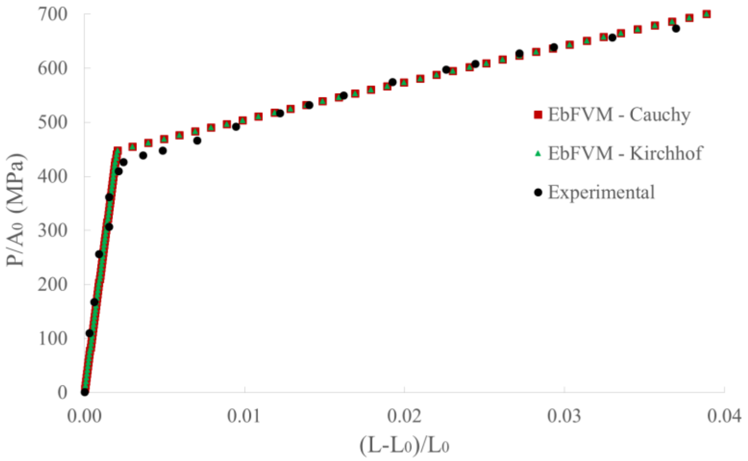
700
600
500
400
300
200
100
0
P/A0 (MPa)
0.00
0.01
0.02
0.03
0.04
(L-L0)/L0
EbFVM - Cauchy
EbFVM - Kirchhof
Experimental

APPENDIX

B

ELEMENTS AND SHAPE FUNCTIONS FOR PRISMS AND TETHAHEDRONS

This appendix shows the elements and their respective shape functions of both tetrahedral and prismatic (with triangular base) elements. Fig. B.1 shows tetrahedral and prismatic elements as well as all their sub-control volumes.

Fig. B.1. 3D elements and their respective sub-control volumes.

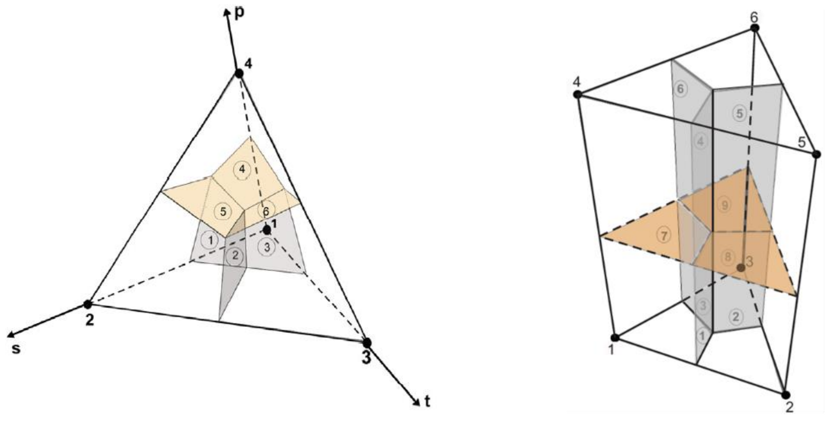

Source: Marcondes et al. (2013).

Explicitly, the shape functions as function of the computational plane for tetrahedral and prismatic elements are given by Eqs. B.1-B.2, respectively.

$$\begin{aligned} N_1(s,t,p) &= 1-s-t-p \\ N_2(s,t,p) &= s \\ N_3(s,t,p) &= t \\ N_4(s,t,p) &= p \end{aligned} \tag{B.1}$$

$$\begin{aligned} N_1(s,t,p) &= (1-s-t)(1-p) \\ N_2(s,t,p) &= s(1-p) \\ N_3(s,t,p) &= t(1-p) \\ N_4(s,t,p) &= p(1-s-t) \\ N_5(s,t,p) &= sp \\ N_6(s,t,p) &= tp \end{aligned} \tag{B.2}$$

where *s*, *t* and *p* denote the local axes in the computational plane.